A COMPUTATIONAL STUDY OF WATER MOBILITY ON SMOOTH SURFACE, CAVITIES AND POROUS STRUCTURE WITH HYDROPHILIC AND HYDROPHOBIC COATINGS

YONG KOK WEE

FACULTY OF ENGINEERING
UNIVERSITY OF MALAYA
KUALA LUMPUR

2020

A COMPUTATIONAL STUDY OF WATER MOBILITY ON SMOOTH SURFACE, CAVITIES AND POROUS STRUCTURE WITH HYDROPHILIC AND HYDROPHOBIC COATINGS

YONG KOK WEE

THESIS SUBMITTED IN FULFILMENT OF THE REQUIREMENTS FOR THE DEGREE OF DOCTOR OF PHILOSOPHY

FACULTY OF ENGINEERING
UNIVERSITY OF MALAYA
KUALA LUMPUR

2020

UNIVERSITI MALAYA

ORIGINAL LITERARY WORK DECLARATION FORM

Name of Candidate:	Yong Kok Wee
Registration No:	KHA160004
Name of Degree:	Doctor of Philosophy (Ph.D)
Title of Thesis:	A Computational Study of Water Mobility on Smooth Surface, Cavities and Porous Structure with Hydrophilic and Hydrophobic Coatings
Field of study:	Computational Fluid Dynamics, Droplet Dynamics and Metallic Foam

I do solemnly and sincerely declare that:

(1) I am the sole author/writer of this work;

(2) This work is original;

(3) Any use of any work in which copyright exists was done by way of fair dealing and for permitted purposes and any excerpt and extract from, or reference to or reproduction of any copyright work has been disclosed expressly and sufficiently and the title of the work and its authorship have been acknowledged in this work;

(4) I do not have any actual knowledge nor ought I reasonably to know that making of this work constitutes an infringement of any copyright work;

(5) I hereby assign and every right in the copyright to this work to the University of Malaya ("UM"), who henceforth shall be the owner of the copyright in this work and that any reproduction or use in any form or by any means whatsoever is prohibited without the consent of UM having been first had and obtained;

(6) I am fully aware that if in course of making this work I have infringed any copyright whether intentionally or otherwise, I may be subject to legal action or any other action as may be determined by UM.

Candidate's Signature Date: 25 July 2020

Subscribed and solemnly declares before.

Witness's Signature Date: 25 July 2020

Name:

Designation:

A COMPUTATIONAL STUDY OF WATER MOBILITY ON SMOOTH SURFACE, CAVITIES AND POROUS STRUCTURE WITH HYDROPHILIC AND HYDROPHOBIC COATINGS

ABSTRACT

This research focus on water mobility and discovers a new phenomenon where droplet accelerates on a hydrophilic cavity surface when sliding down from a hydrophobic surface. The kinetic energy of droplet increases six (6) times higher than before sliding into the first cavity. This finding is useful for creating an effective way of filling liquids into cavities for passive microfluidics related devices. The work consists of validating cases using Computational Fluid Dynamics (CFD) software. The first part of the research reviews the literature regarding CFD modelling of a water droplet (i) sliding down on a surface, (ii) detachment in a gas-flowed microchannel and (iii) jumping upon coalescence on a superhydrophobic surface. Then, this research continues with the investigations regarding the water retention behaviour in porous structures, *i.e.*, an ideal structure and an actual porous metal structure, and further investigates the effect of different static contact angles and liquid drainage rates in a reservoir for each type of porous structures. Also, this research develops a method to quantify additional parameters for porous metal *i.e.,* the structural homogeneity and the number of junctions besides the other parameters like pores per inch and porosity. With that, the present research able to relate the structural variations and its effect on the distribution of water saturation in the porous structures. In details, it detects the presence of large pores in the porous metal geometry, *i.e.*, two times larger than the small pores that reduces the capacity in retaining water.

KAJIAN MELALUI PENGIRAAN KOMPUTER BERKENAAN PERGERAKAN AIR DI ATAS PERMUKAAN LICIN, BERONGGA DAN BENTUK BERLIANG DENGAN SALUTAN HIDROFILIK DAN HIDROFOBIK

ABSTRAK

Kajian ini focus pada mobiliti air dan menemui fenomena baru dimana titisan air memecut di permukaan hidrofilik semasa menggelongsor dari permukaan hidrofobik. Tenaga kinetik pada titisan air meningkat enam kali lebih tinggi dari masa sebelum menggelongsor ke dalam permukaan hidrofobik. Hasil kajian ini berguna dalam mencipta cara yang efektif untuk mengisi titisan bendalir dalam permukaan rongga untuk applikasi mikro-bendaliran. Kajian ini merangkumi kes-kes pengesahan jitu yang menyokong penemuan baru ini menerusi pengunaan perisian Computational Fluid Dynamics (CFD). Tambahan, sebahagian kajian ini meninjau kembali kajian-kajian yang lepas iaitu (i) titisan air menggelongsor di atas permukaan, (ii) titisan air berpisah dalam gas terowong mikro dan (iii) titisan air melompat apabila bergabung antara satu sama lain di atas permukaan hidrofobik yang luar biasa. Kajian ini menyelidik pengekalan air dalam bentuk - bentuk berliang iaitu bentuk ideal dan satu lagi bentuk berliang buih besi. Lanjutan itu, kajian ini menyelidik beberapa jenis hidrofobikasi dan kelajuan pengaliran pada bentuk-bentuk tersebut. Untuk tujuan penilaian, kajian ini mencadangkan cara baru dalam menguantitikan ciri-ciri baru strukturnya iaitu homogenitas and bilangan simpang selain daripada bilangan liang seinchi dan keliangan. Denagan itu, kajian ini mengaitkan keaturan bentuk berliang dengan hasil kajian dalam pengekalan air dan dapat mengesan liang – liang iaitu yang bersaiz dua kali ganda besar dari liang-liang yang terkecil di dalam bentuk berliang besi yang menurunkan kapasiti dalam pengekalan air.

ACKNOWLEDGEMENTS

I want to express my deepest gratitude to my wife, Gan SY and my parents, Yong PK and Foo CY, for their supports; my supervisor, Prof. Ir. Dr Poo Balan Ganesan and co-supervisors, Prof. Dr Kazi Salim Newaz and Prof. Ir. Dr Ramesh Singh for their supports and advice. My gratitude to my heartfelt former teachers, lecturers, and employers including but not limited to my Physics teacher, En. Azman; Mathematics teachers - Ms Ong and Madam Tan LS, Counselling Teacher, Ms Lee HB; all of SMK (L) Bukit Bintang. Tuition tutors, Mr Yee CL, Sunny and Ennie of Yee's family Tuition Sdn. Bhd. My supervisor of Master's Degree and lecturer of the Heat Transfer coursework, Prof. Dr Vijay R. Raghavan of Indian Institute of Technology, Madras; lecturer of the Fluid Mechanics coursework, Dr Ahmad Fuad of University Tun Hussein Onn Malaysia; former employers, Dr Chin Wai Meng of Daikin OYL R&D Center Sdn. Bhd. and Melvin Chan of Dazztech Solution Sdn. Bhd.; the former trainer of Flow-3D, Anurag Chandorkar of Flow Science Inc.; former supervisors, Mohan Dass and Dr Nalasimalu Srikanth of Energy Research Institute of Nanyang Technological University, Singapore; former colleague of Comsol Multiphysics software distributor, Dr Zhao Xin of Singapore; and last but not least, my schoolmate, Mr. Lim Wing Hooi for helping me to proofread this thesis.

TABLE OF CONTENTS

LIST OF FIGURES

LIST OF TABLES

LIST OF SYMBOLS AND ABBREVIATIONS

Symbols

$\boldsymbol{A}$	Area fraction, *(Ax, Ay, Az)*
A_r	Wetted surface area.
$A_{i,cs}$	Area on the cut-section face
$A_{i,out}$	Area of the outer units
$A_{i,in}$	Area of the inside units
A_r^*	Dimensionless form of A_r
A_s	Surface area of metallic foam
a	Major radius of an elliptical shape
α	Plane tilted angle
b	Minor radius of an elliptical shape
β	Mesh density
Ca	Capillary number
γ	Specimen orientation (degree)
d	Pore diameter
$\bar{d}$	Average pore diameter
D_P	Independent RSD factor
$\overline{D}_s$	Overall RSD factor
D	Cavity diameter
d_c	The distance between cell centres
d_s	The distance between the free surface and the centre of the neighbour cell
δx	Length of discrete elements.
E_m	Junction point
$\boldsymbol{F_s}$	Surface tension force
F, F(x)	Volume fraction function

$\boldsymbol{G}\ g$	Gravity field
h_d	Droplet height
h	Spherical cap height
k_n	Constant with *n* of 1, 2, 3…
κ	Surface curvature
L	The total length of metallic foam
$\bar{\iota}$	Average unit length
m_s	Solid mass
N	Number of filled cavities in Chapter 4. Number of pores in Chapter 5.
$N(q)$	Number of specific junctions
N	Number of generated droplets
$\boldsymbol{n}$	Unit normal to the surface interface, Γ
η	The remaining fraction in *N*
$\mathbf{P}$,p	pressure
$P(q)$	Probability of a specific q
ρ_s	Solid density
ϕ	Porosity
ρ	Fluid density
q,q_m	The number of connecting struts at a junction.
ϕ_o	Starting angle from +*x*-axis direction.
r	Radius of a circle
σ	Surface tension coefficient
σ_{SD}	Standard deviation
σ_p	Standard deviation of a variable
S	Spacing between the cavities

t	Time
δt	Time step
t_c	Cavity depth
t_g	Total time in droplets generation
t_g/N	The average droplet generation rate
t_∞	Infinite time
$\boldsymbol{\tau}$	rate of the strain tensor
θ_s	Static contact angle
θ_A	Ascending contact angle
θ_R	Receding contact angle
$\theta_{s,c}$	Static contact angle at the cavity surface
$\theta_{s,nc}$	Static contact angle at the non-cavity surface
$\boldsymbol{U}$	Velocity field
U	Drainage velocity
μ	Dynamics viscosity
μ_s	Mean of a population
μ_p	Mean of a variable
$\overline{v}_c$	Average generated droplet volume per cavity
ν	Kinematic viscosity, μ/ρ
$\bar{v}$	Average solid volume
V_i	Initial droplet size or volume
V_f	Volume fraction
V_s	Solid volume of metallic foam
V_T	Total volume ($l \times w \times h$)
V_F	Fluid volume in metallic foam

x_m, y_m, z_m Coordinates of point E_m

Subscript and Superscript

i	incident
p	Count of independent variable or parameter
x, y, z	Axis directions or groups
*	Dimensionless form

Abbreviations

CFD	Computational Fluid Dynamics
GDL	gas-diffusion-layer
LBM	Lattice Boltzmann method
MRT	Multi-Relaxation Time
PPI	Pores per inch
PEMFC	Polymer Electrolyte Membrane Fuel Cells
SRT	Single-Relaxation-Time
VOF	Volume of Fluid

LIST OF APPENDICES

CHAPTER 1: GENERAL INTRODUCTION

The modelling of water mobility is essential for many applications as it concerns the motion of liquid on different solid surfaces. The energy for its motion originates from (i) the gravity, (ii) the difference in air pressure an enclosed channel, (iii) the surface tension force of liquid or other external forces. In the microliter scale, the water droplet mobility is subjected to forces like the self-weight, the interfacial dispersion forces and the resistance forces from surface roughness which consist of different shapes, cavity spaces and heights. As a result, water mobility varies on different surfaces. The liquid-vapour interface is modelled to be continuously bounded by two regions of fluids (liquid-vapour), which are parallel but located just within the corresponding bulk phases. The process of vaporisation and condensation at the liquid-vapour interfaces are neglected in the modelling at macroscale treatment (Carey, 2008). In literatures, there is a lacking of simulation study regarding validation cases related to droplet dynamics motion on surfaces with different hydrophobicity. Simulation validation cases are crucial as it can provide insights for designers in developing a better device.

1.1 Problem Statements

Micro/nano fluid droplet generation in microfluidics devices can be found in many biomedical and chemical studies (Popova et al., 2015; Carreras & Wang, 2017). Some of the examples are the devices fabricated in polydimethylsiloxane (PDMS) for polar solvents (Baah et al., 2012; Zeng et al., 2018), glass capillary microfluidic applications (Herranz-Blanco et al., 2017; Nabavi et al., 2015) and terrace-based microfluidics (Vladisavljević et al., 2018). However, there are some limitations in those devices, such as their fabrication being difficult, high cost and limited usage, and some devices are thermodynamically unstable as reviewed by Liu et al. (2017). The application of an alternative technology, which was much simpler to manufacture and use, was found

in recent studies by Lin et al. (2018) and Chang et al. (2016). The substrates used in both the studies were patterned with coatings where the small droplets 'stick' on the hydrophilic surface but slide on the main hydrophobic surface. In that regard, the present research investigates droplet sliding behaviour in a cavity substrate under specific conditions through Computational Fluid Dynamics (CFD). On the other hand, the study of water mobility behaviour on porous surface like metallic foam could provide better understandings regarding the influence of its interior shapes on the water retention behaviour. Such insights are crucial in developing the metallic foam as fins for the use in heat exchanger in the application of condensation. Another challenge faced by this initiative is due to the lacking of method or technology for checking the quality of the fins in details at the early stage of manufacturing.

1.2 Importance of the Research

The research work addresses a few of the important issues. It compiles an extensive literature regarding dynamics motion of microliter droplet on surfaces and microchannel with different hydrophobicity. It provides many insights in performing the simulation validation cases for droplet sliding down a surface and cavities. With that, it creates an opportunity for a development of a new microfluidics device in generating micro-droplets more efficiently. The research work provides a proper quantification on metallic foam structure like porous metal. It enables the parameters to be related with the physical results for a better understanding and possible making it predictable. In term of water retention behaviour, it gives a meaningful insight in designing fins which will work effectively in the application of cooling and dehumidification. It gives the possibility for developing technology through the use of automation and robotics, the same know-how can be developed into computer algorithm for checking the metallic foam shapes in large quantity at the early stage of manufacturing and reduced the number of tests indirectly.

1.3 Objectives of the Research

The objectives are to perform computational modelling of:

(a) Droplet slide down on smooth surface with hydrophilic and hydrophobic coatings.

(b) Droplet slide down on cavities with hydrophilic and hydrophobic coatings.

(c) Water retention on porous geometries with hydrophilic and hydrophobic coatings.

1.4 Scopes of the Research

The research reviews literature regarding water droplet behaviour in three different categories, *i.e.*, (i) droplet sliding down on surfaces, (ii) droplet jumping upon coalescence on a superhydrophobic surface and (iii) droplet detachment in microchannel. It followed by investigating the water droplet sliding down behaviour on a plain surface with different hydrophobicity *i.e.*, hydrophilic, hydrophobic and superhydrophobic. Next, the research investigates the water droplet sliding down behaviour on a surface with cavities. The varied parameters are hydrophobicity, cavity depth, cavity spacing, substrate tilted angle (α) and initial droplet volumes. Lastly, the research investigates the water mobility behaviour in porous structures specifically a porous metal and an ideal geometry. The studies varied the water drainage velocity (U) and the hydrophobicity.

1.5 Novelty and Contribution of the Research

The present research has summarized extensively on the possible physical behaviours of a droplet motion in micro-scale applications. It provides many updated information regarding the relevant publications in the recent years. The present research also achieved a good validation cases for simulation of droplet sliding down motion on a surface with different hydrophobicity. Furthermore, the present research created and studied a new microfluidics device in generating micro-droplets. A new phenomenon was

discovered where the droplet on hydrophobic surface accelerates when it slide down into hydrophilic surface. It allows designer to create a more efficient device in that technology.

The present research developed a method for quantifying the interior shapes of porous metal. The method uses a combination of several concepts found in different mathematical studies *i.e.,* treating or simplifying the solid junction as a coordinate point, is similar to the data treatment used in the subject of "Stochastic Geometry"; the 'tracking' technique used to connect the coordinate points are used in the subject of "Topology"; the Relative Standard Deviation is profoundly used in the subject of "Statistics". The method was able to detect the location of large pores and calculated the degree of variation in the porous metal. The quantification method was proven to be workable as it was able to relate the structural variations and the water retention behaviour in porous structures. The same quantification method can be applied for other physical analysis study. With the proven method, the present research has identified the additional parameters of the porous metal *i.e.,* structural homogeneity and number of junctions besides pores per inch (PPI) and porosity which are commonly used. Furthermore, the present research compared the water retention behaviours in the porous structures with different types of heat exchangers. It provides a meaningful insight in designing fins which will work effectively in the application of cooling and dehumidification.

1.6 The Limitations of the Research

In Chapter 3, the validation cases used solely experimental results of Sakai et al. (2006) because many literatures published after that do not have sufficient information. In the same work, the validation cases uses no surface roughness for the simulation model. It is because the surface roughness function in the CFD software is meant for predicting the turbulent sub-layers for large scale application *e.g.*, open-channel flow or pipe flow. In Chapter 5, the required computing time was very high. The size of the porous metal

was small, *i.e.,* 3mm × 3mm × 3mm, due to limited computing power available. Yet, it is acceptable because it is close to the scale of louver fins. The simulation took averagely 2 weeks to complete one simulation case. On the other hand, the selection of parameter range for the studies in Chapter 5 are crucial. It was found that the water surface was sloshing due to liquid separation for the range θ_s of 30° and U is 8mm/s. The water level bounced and reattached to the porous metal geometry after the free surface separation. Due to this reason, that set of data was excluded from the analysis.

CHAPTER 2: LITERATURE REVIEW

2.1 Introduction

This chapter reviews literature regarding computational modelling of droplet dynamics behaviour for three categories, *i.e.* (i) droplet sliding down on surfaces, (ii) droplet detachment in microchannel and (iii) droplet jumping upon coalescence on a superhydrophobic surface.

2.1.1 Static Contact Angle

At microscale application, water is often found in the form of droplets on solid surfaces. Droplet static contact angle (θ_s) is the angle made at the three-phase contact line, *i.e.*, solid, liquid and gas. A droplet on a hydrophilic surface has $\theta_s < 90^{\circ}$. Hydrophilic surface is commonly found on an uncoated glass surface. A droplet on a hydrophobic surf9ace has θ_s ranging from 90° to 150° while a droplet on a superhydrophobic surface has θ_s at least 150°. The liquid-vapour interface of a droplet is associated with interfacial tension due to the result of Van Der Waals forces which exist in all matters. In the thermodynamic analysis, the liquid-vapour interface is modelled to be continuously bounded by two regions of fluids (*i.e.*, liquid and vapour), which are parallel but located just within the corresponding bulk phases. In both of the regions, the internal energies and densities vary continuously across the liquid-vapour interface (Carey, 2008). In the macroscopic treatment or modelling, it neglects the process of vaporisation and condensation at the liquid-vapour interfaces for simplicity.

The equation of Young is stated as, $\cos(\theta_e) = (\gamma_{SV} - \gamma_{SL})/\gamma_{LV}$, where γ refers to the interfacial surface tensions with *S*, *L* and *V* as solid, liquid, and gas, respectively. Thereafter, two models were considered for a droplet in force equilibrium on a surface, *i.e.*, Wenzel's model and Cassie-Baxter model. In Wenzel's model, the liquid droplet conforms to the base surface with the inclusion of the surface roughness (see Figure 2.1a).

Wenzel proposed a modified equation of Young which is given by, $\cos(\theta_w) = r\cos(\theta_e)$, where θ_w represents the apparent θ_s on the wetted surface and r is a ratio of the actual area to the projected area.

In Cassie–Baxter's model, the liquid droplet retains an almost spherical or round shape on the rough structure surfaces without conforming the base surface (see Figure 2.1b). The Cassie model is expressed by, $\cos(\theta_C) = f\cos(\theta_e) - (1 - f)$, wherein θ_C represents the apparent θ_s on the composite surface and f is the area fraction of the solid surface in contact with the liquid. Cassie-Baxter's model is associated with high apparent θ_s. It showed a lesser hysteresis θ_s than Wenzel's model (Bormashenko & Faculty, 2015; Cui et al., 2011; He et al., 2004; He et al., 2003; Khojasteh et al., 2016; Mchale et al., 2004; Zhu et al., 2012). Wenzel's state predicts a "sticky" surface. Cassie-Baxter type of surfaces predict a "slip" surface. Generally, a droplet has more resistance to move on a "sticky" than a "slip" surface.

A droplet can have two distinct θ_s on the same rough surface (Patankar, 2003). The droplet can rest in a stable position of Wenzel's state or Cassie-Baxter's state that one's θ_s is higher than another. There is no guarantee that the droplet will always go to its lowest energy state (Wenzel's state) from the higher energy state (Cassie-Baxter's state). Later, He et al. (2003) confirmed the prediction through experiments. However, the exact details of the transition are not well understood. Patankar (2003) believed that the intermediate energy barrier exists. For droplet to be in the lowest energy state, the liquid must start filling the valleys or grooves of the substrate as the transition occurs.

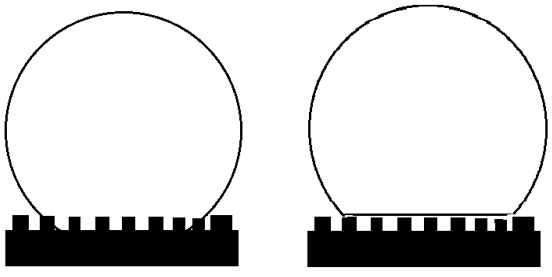

(a) (b)

Figure 2.1: Wenzel's state (left) and Cassie–Baxter's state (right)

Another method is to press the droplet down to enable the transition (Bico et al., 1999). In applying the theories, He et al. (2003) created a composite surface consisting of different materials. Then, He et al. (2003) varied the spacing of the pillars to achieve a robust superhydrophobic surface which consists of a common state surface energy for the droplet. He et al. (2003) applied the equations of both Wenzel's and Cassie-Baxter's models and related the constants with the pillar spacing. The side of a unit pillar is denoted as 'a' while the spacing between pillar is denoted as 'b'. The Wenzel's state equation is given by, $\cos(\theta_w) = [1 + 4A/(a/H)]\cos(\theta_e)$, and $\cos(\theta_C) = A(1 + \cos\theta_e) - 1$, wherein $A = 1/(b/a + 1)^2$, and 'H' as the pillar height. They worked the theoretical relation of the equations of states versus the parameter of 'b/a'. The curves intersect at a point which can be used to design a robust substrate where the energies of both surfaces are the same.

2.1.2 Different Hydrophobicity in Applications

Hydrophilic surface can be found in automobile where the rear-view mirrors for preventing fogging (Wang et al., 1997). In air conditioning systems, the hydrophilic coating is applied on aluminium fins of an evaporator for lowering the θ_s. It prevents the droplet from bridging between the fins and forming a higher pressure drop on the evaporator (Wang & Chang, 1998; Jhee et al., 2002; Kim et al., 2002; Liu & Jacobi, 2006; Min & Webb, 2000; Wu & Webb, 2001; Moallem et al., 2012). In the condensates formation study, a hydrophilic surface was used to observe the dynamics coalescences with the neighbouring condensates (Hu et al., 2016; Chu et al., 2017; Kim et al., 2017). Such study helps to develop a more efficient way of removing condensates from fin surfaces (Shi et al., 2015; Farokhirad et al., 2015; Khatir et al., 2016; Zhang & Yuan, 2018).

In the past, many research topics related to droplet behaviour on hydrophobic surface had emerged, *e.g.*, anti-icing surface (Cao et al., 2009; Boreyko & Collier, 2013; Zhang et al., 2013; Tavakoli & Kavehpour, 2015; Kim et al., 2017), droplet impact on hydrophobic surface (Kamali et al., 2016; Li et al., 2016; Patil et al., 2016), microliter droplet evaporation (McHale et al., 1998; Moffat et al., 2009; Patil & Bhardwaj, 2014), nanoliter droplet dispensers (Önnerfjord et al., 1998; Ren et al., 2004; Choi et al., 2007), droplet sliding behaviour on different surface roughness (Suzuki et al., 2004; Yoshida et al., 2006) and different surface structures (Yoshimitsu et al., 2002; Yeong et al., 2011; Thanh-vinh et al., 2015).

In nature, raindrops slide down on lotus leaves in a superhydrophobic condition (Barthlott & Neinhuis, 1997; Feng et al., 2002; Ueda & Levkin, 2013). It gathers dust particles which results in self-cleaning while rolling down. A superhydrophobic surface method can be fabricated through several methods like solidification of melted Alkylketene-dimer (Onda et al., 1996; Yan et al., 2006; Fang et al., 2008), anodic oxidization of Aluminium (Shibuichi et al., 1998; He et al., 2009; Saffari et al., 2018) and microwave plasma-enhanced CVD method using Trimethylmethoxysilane (TMMOS) (Wu et al., 2002; Wu, 2006). Superhydrophobic surface can be found to be similar to hydrophobic surface ones, *e.g.*, anti-freezing (Wang et al., 2007; Jin et al., 2016; Wang et al., 2018), condenser/evaporator (Garrod et al., 2007; Marcinichen et al., 2012; Wang et al., 2018) and microfluidic valves (Washe et al., 2013; Kosmas et al., 2014; Ellinas et al., 2017).

Mixed surfaces can be a patterned surface of hydrophilic/hydrophobic stripes. It is studied for a passive control system on droplets sliding downward (Drelich et al., 1996; Matsui et al., 2012; Suzuki et al., 2008). Lee et al. (2016) studied the sliding direction of droplet changes with different orientation of stripe-patterned surfaces using computational modelling. In microfluidics application, a sliding mechanism or gravity-

induced method generates high quantity droplets in nanoliter size on patterned hydrophilic dots on the hydrophobic surface (Chang et al., 2016; Huang et al., 2007; Lin et al., 2018).

2.1.3 Droplet Sliding Down on Surface

A droplet retained on a tilted surface exhibits variations in θ_s azimuthally. Parameters such as θ_s hysteresis, which is the difference between its advancing angle (largest θ_s) and receding angle (smallest θ_s), were introduced to characterise the relation at the inclined plane (ElSherbini & Jacobi, 2004a; ElSherbini & Jacobi, 2004b; ElSherbini & Jacobi, 2006). The θ_s hysteresis for a droplet on polymer surface does not mean it is simultaneously equal to the surface inclination at which it started to slide downward (Krasovitski & Marmur, 2005; Yoshida et al., 2006). It implies that the relation of θ_s hysteresis and gravitational pull is a non-linear one. Another method of studying the advancing and receding angle was done by spreading and slurping the water droplet from its source (Sakai, 2006). On tilted surfaces, it was shown that the droplet slides down with (i) rotating motion on a hydrophilic surface, (ii) partially rotating and slip-off motion on the hydrophobic surface and (iii) a full slip-off motion on a superhydrophobic surface (Sakai et al., 2006). While, a droplet on a rough hydrophobic surface experiences elongation and contraction while sliding down (Suzuki et al., 2004).

2.1.4 Droplet Jumping upon Coalescence on a Superhydrophobic Surface

Interestingly, droplet is found to jump spontaneously upon coalescence on the superhydrophobic surface (Boreyko & Chen, 2009; Miljkovic et al., 2013; Nam et al., 2013; Peng et al., 2013). It was estimated the conversion for the jumping motion; it was about 20% of the total energy released upon the coalescence (Boreyko & Chen, 2009). For the same conditions, Peng et al. (2013) estimated a release of 25.2% of that total

energy. A small droplet would jump with a higher velocity than a large droplet. However, the velocity of very tiny droplet is limited by air resistance (Boreyko & Chen, 2009). Therefore, an optimum condition exists for the droplet to jump at the highest velocity. Khatir et al. (2016) investigated different droplet radius; ranging from 100 to 515 microns. They compared the numerical results of VOF and Lattice Boltzmann Method (LBM) and the experiments. It was estimated that the droplet with a radius of 35–40 μm would jump on a surface with θ_s of 160° as it yielded the highest velocity. Zhang and Yuan (2018) demonstrated the effect of different surface roughness. The surface condition that favour droplet jumping is the surface with roughness properties with smaller skewness, larger root mean square and Kurtosis of three units approximately. Generally, the condition of which the droplets jump with the highest velocity is thought to yield the highest rate of condensation. However, that assumption had excluded the effect of airflow on the trajectories of droplets and the heat transfer on the surface. Miljkovic et al. (2013) investigated the effect of electric-field on the phenomenon under the influence of airflow and found that the droplets were jumping with longer distances due to the enhancement of the electric field while the small droplets were jumping to early coalescences. As compared to state-of-art dropwise condensation, Miljkovic et al. (2013) reported that the electric-field enhanced the condensation and the overall heat transfer increased between 30% and 50% respectively.

2.1.5 Droplet Detachment in a Microchannel

Droplet detachment in the microchannel can be found in Polymer Electrolyte Membrane Fuel Cells (PEMFC). The device is one of the leading advanced energy conversion technology used for transportation. It generates water droplets through the catalytic processes and dispenses the water through the gas-flowed microchannels. In PEMFC assembly, it consists of the dielectric membrane-Nafion, gas diffusion layers,

electrolyte, electrodes, catalyst and gas sources, *i.e.*, hydrogen and oxygen gases. The membrane requires sufficient liquid water in operation. Thus, the usual operation temperature is below 90 °C, which prevents high evaporation rate in the system. In a complete electrical circuit, the electrons move from anode to cathode through the wires and electrical resistances. Simultaneously, the electrons move within the PEMFC assembly from cathode to anode. Commonly, the working principle of PEMFC is explained from the perspective of ions transport. Herein, this paragraph explains the working principle from the perspective of charge carriers as the nature requires far less energy for the electrons to move from an ion to another ion than the ion itself. It is a similar concept to explain the movement of charge carriers in a transistor. The motion of electrons that is relative to the electrolytes (from the cathode to the anode) makes as if the protons (hydrogen ions) travel in the opposite direction. During the operation, the anode side, which is separated by different the layers receives the supply of hydrogen gas (Loyselle & Prokopius, 2011). The hydrogen gas together with an electron (from the cathode) split catalytically into two unit pairs of hydrogen ion and an electron; and the electron moves into the electrical circuit around the copper wires. At the cathode, the oxygen gas combines with the hydrogen ions and electrons catalytically to form the water molecules.

As the water pressure builds up internally, it forces the water to move within the pores and accumulates at the surface of the gas-diffusion-layer (GDL) in a droplet form. In PEMFC, the water dispensing method requires gas pressure to force the water droplets to move along the microchannel. Other innovative methods of water removal are, *e.g.,* flexural wave (Byun & Kwak, 2019), acoustic pressure wave (Mortazavi et al., 2019), and vibrational-acoustical methods (Palan et al., 2006). The average size of the droplet is less than 4 μL (Cho et al., 2012; Hao & Cheng, 2010; Qin et al., 2012; Theodorakakos et al., 2006; Zhu et al., 2010). The presence of droplet in the microchannel causes an

increase of 2 to 4 times pressure drop (Qin et al., 2012; Zhu et al., 2010). Water film could block the microchannel if it is over-accumulated or not appropriately dispensed. If liquid water blocks the microchannels, the diffusion layers will become saturated; it will degrade the fuel cell performance as it could not transport the waste heat in the system (Bazylak, Sinton, & Djilali, 2008; Hartnig et al., 2009; Kumar & Reddy, 2003). At the anode, the microchannel blockage can cause voltage reduction and fuel starvation to the catalyst layer which can lead to fast oxidation and accelerates the ionomer degradation.

Yang et al. (2004) observed the dynamic behaviour of water droplets in a gas microchannel. The setup characterised the test under automotive condition, *i.e.*, 0.82 A/cm^2 and 70°C. The growth of the water droplet was found to be non-linear or discontinued at times. It happened because of the water in GDL layers still filling or spreading beneath it. At the time of coalescence, the two droplets that were growing closer together, collide and would sticks to the hydrophilic wall on the side. In the author's opinion, the droplet could have experienced agitation on the liquid-vapour interface or a slight jump from the floor upon the coalescence.

The behaviour of droplet detachment in microchannel is subject to parameters such as the channel size, hydrophobicity of the walls and GDL uneven fibre features (Qin et al., 2012), droplet generation rate, pressure difference, temperature changes, permeability of the GDL and electric current flow (Cho et al., 2012; Hao & Cheng, 2010; Qin et al., 2012; Theodorakakos et al., 2006; Zhu et al., 2010). Cho et al. (2012) conducted experiments to model the droplet behaviour in a microchannel and obtained both the top and side views of a droplet in the experiment and developed a coefficient of drag for a droplet in the microchannel. They estimated the velocity and the droplet size that was about to detach from its source. Those correlations were used to develop an estimation of the droplet shape and then, validated it using numerical solution.

Theodorakakos et al. (2006) investigated the behaviour of droplet on three different surfaces. The droplet remained the same shape in the steady flow condition, but the θ_s would change with different temperature. The shape of the droplet was similar to the work of Hao and Cheng (2010), who used LBM for their predictions. Also, they observed that the droplet detached from the wall only at a very high gas velocity (~16m/s). However, the gas flow rate in the application is around 5 m/s or equal to Re 164 due to practicality issues (Qin et al., 2012).

Zhu et al. (2010) studied the motion of the droplets with a continuous generation condition. Such modelling setup is closer to the actual conditions as the continuous generation of droplet affects the motion of the previously detached droplet in the microchannel. As the droplet occupies the microchannel, the free-flow area becomes lesser. Thus, the flow pressure focus on the newly generated droplet was more than the previously detached one. The same approach was used in Qin et al. (Qin et al., 2012). Zhu et al. (2010) investigated the droplet behaviour in a rectangular microchannel with the same cross-section area but used different aspect ratio of height to width. The findings showed that the droplet tends to stick at sidewalls for cases of high aspect ratio cases. On the other hand, the droplet tends to stick on the top wall for all cases of low aspect ratio. The longest detachment time and the largest detachment diameter occur in cases of aspect ratio of half. The longest removal time for a droplet to exit the microchannel occurs at aspect ratio of 0.25. The highest pressure drop in the microchannel consisting a droplet occurs at aspect ratio of 0.1. Also, a semi-circular microchannel was investigated as well. The detachment time for semi-circle channel is longer than the rectangle, but the removal time is shorter than the rectangular cross-section type.

Furthermore, Zhu et al. (2010) investigated other types of cross-section, *i.e.,* the rectangular with the curved bottom wall, trapezoidal, upside-down Trapezoidal and triangular microchannels. Those microchannels have equal width and height. The

constraints were practical as it would not change the number of channels per row in the arrays. They measured the detachment time, the droplet diameter during detachment and the total droplet removal time. The performance favoured the triangular cross-section; in descending order, it followed by a trapezoid, the rectangle with a curved bottom wall, rectangular and upside-down trapezoid. They presented the results in ratios, *i.e.,* (i) the wetted area to the area of microchannel wall, (ii) the water volume to the microchannel volume and (iii) the friction factor during operation to friction factor of an empty microchannel.

Qin et al. (2012) investigated the phenomenon by performing a series of CFD simulations and focused on the role of walls hydrophobicity and the GDL for the water dispensing purpose. Qin et al. (2012) found that the droplet took a lesser time to detach from the source on the surface of a higher hydrophobicity than a lower one. During the detachment, the droplet leaned forward, and the ascending θ_s increases with higher gas flow rate. Furthermore, Qin et al. (2012) confirmed that the microchannel walls in the hydrophilic conditions could prevent the microchannel from clogging. At first glance, those physical behaviours may seem to contradict the understanding that the droplet would travel faster on the hydrophobic surface. Qin et al. (2012) showed that the temporal result of transporting the volume of liquid on the sidewalls of a microchannel similar to the observations made by Yang et al.,(2004)s' experiment, where the gas flow induces drag on the water film. Over the time, the film on the hydrophilic wall grew toward the end of the microchannel as the airflow was shearing the film. Qin et al. (2012) observed the liquid film that was thinning at the leading edge but thickening at the end of the microchannel. The airflow caused the extra volume of water to propagate as a surface wave toward the exit. As the water volume increases at the end of the channel (film), the liquid would be sheared-off by the gas flow eventually.

2.2 Comparisons of the selected categories

The earlier development in computational modelling of droplet dynamics is mostly regarded as the prediction of droplet motion on the hydrophilic surface only. In the recent years, there is growing interest in computational modelling regarding droplet sliding down a surface (Ahmed et al., 2013, 2014; Dupont & Legendre, 2010; Koh et al., 2009; Lee et al., 2016; Oliveira et al., 2011; Annapragada et al., 2012; Schwartz et al., 2005; Spelt, 2005). For the ease of writing, the subject is denoted as a type-A simulation hereafter (see Figure 2.2). In another category, the computational modelling of droplet detachment in a gas-flowed microchannel, applied for PEMFC usually, denoted as type-B simulation, concerns the water dispensing design that uses the gas pressure flow from one end of a microchannel to force out the water droplets inside to the other end (Cho et al., 2012; Hao & Cheng, 2010; Qin et al., 2012; Theodorakakos et al., 2006; Zhu et al., 2010). As compared to other categories, the number of publication related to type-B simulation was low since 2012. New types of modelling studies related to the technology have been reported recently, *i.e.,* the phenomenon of water droplet jump upon coalescence in microchannel (Hou et al., 2018), the water droplet breaking through a gas diffusion layer (Yu et al., 2018) and droplet sliding angle on hydrophobic wire screens (Venkateshan & Tafreshi, 2018).

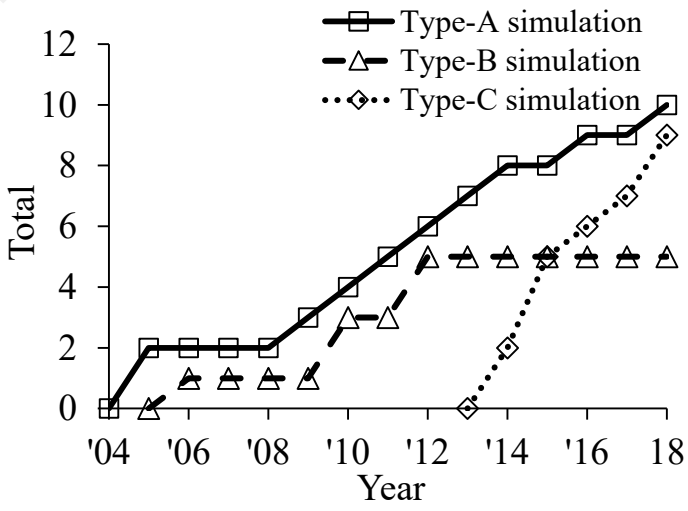

Figure 2.2: Cumulative number of publications in each type of simulation from 2005 to 2018.

In another category, the publication related to the phenomenon of droplet jumping upon coalescence on a superhydrophobic surface, denoted as type-C simulation, increased rapidly in recent years. It is believed that such a phenomenon could enhance the performance of cooling and dehumidifying process for the ease of removing condensates from the fin surfaces. Amongst the publications, three-dimensional (3D) modelling was reported in higher numbers than two-dimensional (2D) ones.

As shown in Figure 2.3, the number of publications concerning 2D modelling was comparatively low in 2014. Most of the 2D computational modelling was published with unique numerical approaches or techniques (Dupont & Legendre, 2010; Oliveira et al., 2011; Spelt, 2005; Zhang & Yuan, 2018) and to validate the solutions (Cho et al., 2012). Liu and Peng explained the limitation of using 2D computational modelling for droplet dynamics (Liu & Cheng, 2015; Liu et al., 2014). Recently, a new had been developed to replace the previous 2D modelling method (Shang et al., 2018). It uses a 3D front-tracking method that integrates the generalised Navier boundary condition to model the moving contact line.

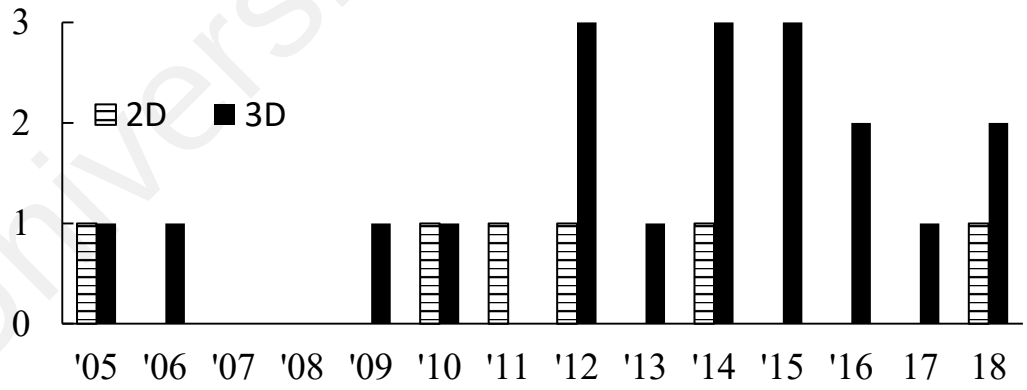

Figure 2.3: Number of publications using 2D and 3D simulations reported from the year 2005 to 2018.

2.2.1 Reference for Validations

In research related to droplet sliding down a plane, Spelt (2005) validated their numerical scheme of Level Set method with the boundary element method of Schleizer and Bonnecaze (1999). The validations showed accurate results. Besides other references

(Lavi & Marmur, 2004; Ramos et al., 2010; Sakai et al., 2006; Schleizer & Bonnecaze, 1999), Podgorski et al. (2001)s' experimental results were the most preferred for validating computational modelling results in that category (Ahmed et al., 2014; Koh et al., 2009; Schwartz et al., 2005).

In the past, computational modelling of droplet movement in the water dispensing microchannel were conducted to investigate the droplet behaviour in particular for different channel size, hydrophobicity, droplet generation rate and air velocities (Cho et al., 2012; Hao & Cheng, 2010; Qin et al., 2012; Theodorakakos et al., 2006; Zhu et al., 2010). It was essential for avoiding unstable behaviour during the droplet growth and detachments in the microchannel (Okada et al., 1998; Wang et al., 2001; You & Liu, 2002).

In topics related to droplet detachment in microchannel (Okada et al., 1998; Wang et al., 2001; You & Liu, 2002), most of the researchers conducted their own experimental works and performed numerical simulations (Cho et al., 2012; Hao & Cheng, 2010; Theodorakakos et al., 2006; Zhu et al., 2010). It was with exception that Qin et al. (2012) compared their computational modelling results with the experimental results of Bazylak et al. (2008) and Hartnig et al. (2009).

In reality, the droplet rests or move with a short contact length on the superhydrophobic surface, which creates very little resistance for the droplet to slide down (Gogte et al., 2005; Sakai et al., 2006). In the literature, most of the modelling assumed that the droplet has a full-surface contact with its base. As such, the modelling would have significant discrepancies with the experimental results. The discrepancy was observed in the validation work of Kulju et al. (2018). As compared to the CFD result of the superhydrophobic surface, the CFD result of the droplet impacting on a hydrophobic surface was inaccurate due to longer contact time. Since the θ_s is lower for a hydrophobic surface, the surface tension force is lower as compared to a superhydrophobic surface.

Simultaneously, it occupied a larger area, of which, it was a full-contact length. Thus, it reduced the kinetic energy of the droplet. In the case of droplet jumping upon coalescence on superhydrophobic surface, the experimental results of Boreyko and Chen (2009) and the numerical work of Liu et al. (2014) who used the pseudopotential model of LBM of Yue et al. (2006) were the most popular reference for validation besides other references (Lv et al., 2013; Miljkovic et al., 2013; Yuan, 2005; Zhang et al., 2014).

2.2.2 Hydrophobicity

There is a norm in hydrophobicity used in each category of the studies. As shown in Figure 2.4, the most investigated surface in the category of droplet sliding down a surface (type-A) was the hydrophilic type. In the category of droplet detachment in a gas-flowed microchannel (type-B category), the hydrophobic surface was mainly used except by Qin et al. (2012) who extended the θ_s in the study to 170°. As for the category of droplet jumping upon coalescence (type-C), the superhydrophobic surface was mainly used. In some studies, the phenomenon was studied with θ_s as low as 130° (Khatir et al., 2016; Shi et al., 2015; Zhang & Yuan, 2018) and as high as 180° (Farokhirad et al., 2015; Khatir et al., 2016; Liu et al., 2014).

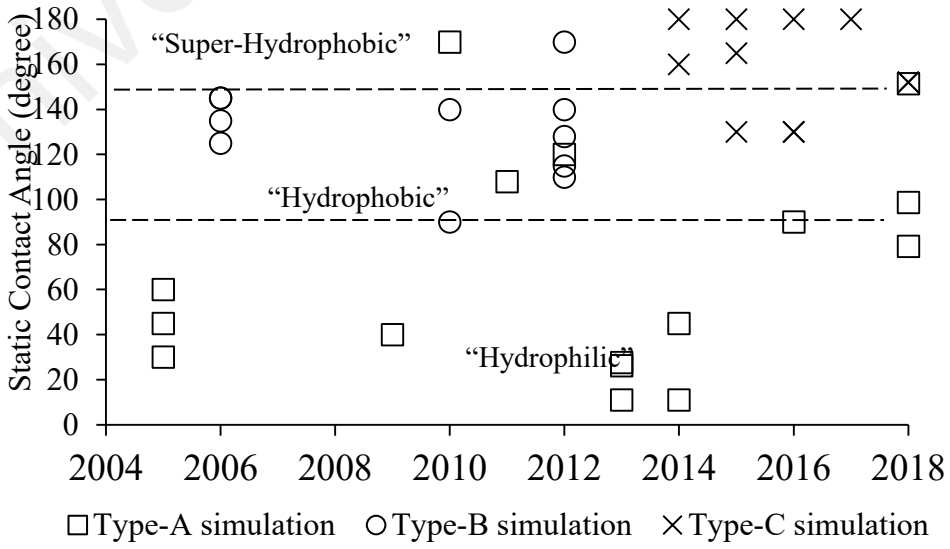

Figure 2.4: Distribution of hydrophobicity used in different types of simulation.

2.2.3 Liquid Droplet Size

In Figure 2.5, the droplet volume in the categories of type-A, type-B and type-C are grouped and presented with each volume (data point) with reference. Generally, the droplet size used in Type-A simulation was the largest as compared to other categories. For type-B, the range of droplet size was between the Type-A and Type-C. The estimation of the droplet size in the microchannel was equal to the duration of detachment time multiplied by the rate of injection. Among the categories, 'Type-C' simulation had the most extensive range of droplet size. It indicated that the factor of hydrophobicity influenced the phenomenon more than the size of the droplet itself.

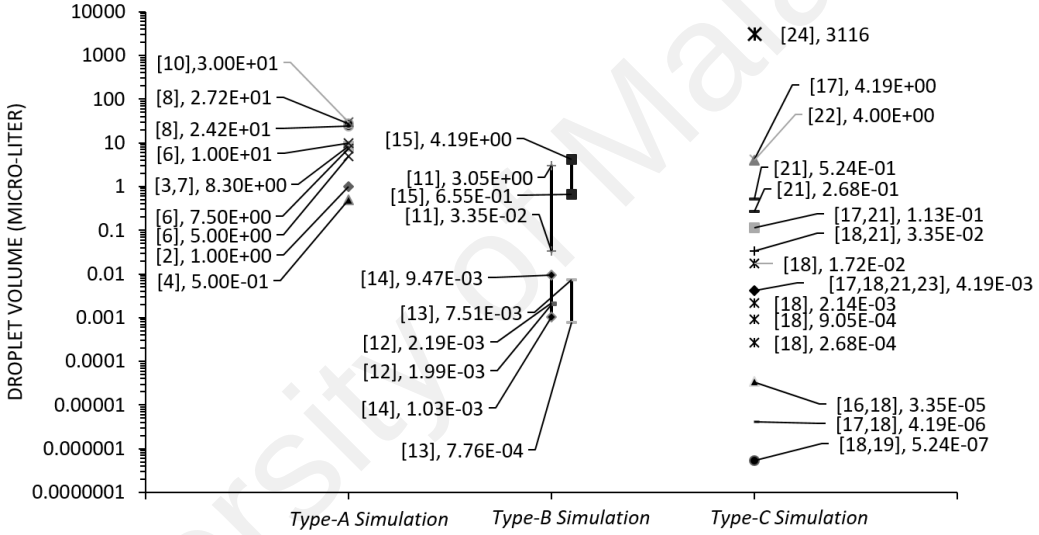

Legend:

[1] Spelt (2005)	[9] Lee et al. (2016)	[17] Liu et al. (2014)
[2] Schwartz et al. (2005)	[10] Yong et al. (2018)	[18] Liu and Cheng (2015)
[3] Koh et al. (2009)	[11] Theodorakakos, et al. (2006)	[19]Farokhirad and Lee (2015)
[4] Dupont and Legendre (2010)	[12] Zhu et al. (2010)	[20] Shi et al. (2015)
[5] Oliveira et al. (2011)	[13] Hao and Cheng (2010)	[21] Khatir et al. (2016)
[6] R. Annapragada et al. (2012)	[14] Qin et al. (2012)	[22] Zhang and Yuan (2018)
[7] Ahmed et al. (2013)	[15] Cho et al. (2012)	[23] Chu et al. (2018)
[8] Ahmed et al. (2014)	[16] Liu et al. (2014)	[24] Shi and Tang (2018)

Figure 2.5: Each data point consists of at least a reference and is followed by the droplet volume used in that paper.

2.2.4 Numerical Methods

The first challenge in modelling droplet liquid-vapour interface is to implement of mass and momentum conservation equations. The second is to model the discontinuities in fluids density across the interface. Third, it is to handle of complex

numerical treatment for droplet advection. For modelling the physics, there are several numerical models, *e.g.*, "long-wave or lubrication approximation" coupled with the "disjoining pressure" model (Schwartz et al., 2005) with the accuracy of this method being dependent on the sublayer height in addition to the mesh size (Koh et al., 2009); Volume-of-Fluid (VOF) with unique numerical treatments that track the droplet advection and free-surface interfaces (Hirt & Nichols, 1981); and the LBM (Hao & Cheng, 2010; Shan & Chen, 1994).

"Long-wave or lubrication approximation" coupled with the "disjoining pressure" model assumes a layer of liquid with an isolated droplet on a plane substrate. The liquid surface corresponds to $z= h(x,y,t)$ where t is time. The mass conservation, $h_t = -\nabla \cdot Q + w_i(x,y,t)$, where w_i is a local injection rate and the term, $= \int_0^{h(x,y)}(U,V)dz$, wherein U and V are the component velocities in x and y directions. In lubrication theory, it assumes the droplet moves slowly where its body forces are negligible. The free surface at the contact line inclines with a small angle relative to the substrate (Schwartz, 1998). Under such an assumption, the model is capable of analysing hydrophilic conditions only. The substrate has a no-slip condition, and the free surface is a slip condition. The pressure in the liquid is, $P = -\sigma\kappa - \Pi \approx -\sigma\nabla^2 h - \Pi$, where κ is free-surface curvature, σ is surface tension coefficient and the so-called "disjoining pressure" is given by, $\Pi = \mathrm{B}[(h^*/h)^n - (h^*/h)^m]$, wherein B, n and m are positive constants and $h^*$is the thin wetting layer thickness above the substrate.

In the VOF method, a sharp interface is commonly used to represent the liquid-vapour interface for the one-fluid and two-fluid models (Hirt & Nichols, 1981; Ravi et al., 2012). The approach volume fractions of liquid-solid regions embedded the geometry into the mesh. In the VOF method, the mass continuity equation is given by

$$\frac{1}{V_F}\frac{\partial}{\partial x}(\rho u A_x) + \frac{1}{V_F}\frac{\partial}{\partial y}\left(\rho v A_y\right) + \frac{1}{V_F}\frac{\partial}{\partial z}(\rho w A_z) = 0 \qquad (2.1)$$

Where V_F is fractional volume open to flow, (A_x, A_y, A_z) are the fractional areas that open to flow. The parameter ρ is the fluid density, and the variables (u, v, w) are the fluid velocity components. It uses the fractional face areas and the fractional volumes of the cells that are open to the flow for defining the wall boundary features in the mesh. In each cell, the solver computes the surface fluxes, surface stress, and body forces. It treats the cell as a control volume. These quantities are then used to form approximations for the conservations laws as expressed by the equation of motion. The equations of motion for the fluid velocity components are the Navier-stokes equations as given below:

$$\frac{\partial u}{\partial t} + \frac{1}{V_F}\left\{uA_x\frac{\partial u}{\partial x} + vA_y\frac{\partial u}{\partial y} + wA_z\frac{\partial u}{\partial z}\right\} = -\frac{1}{\rho}\frac{\partial p}{\partial x} + G_x + f_x$$

$$\frac{\partial v}{\partial t} + \frac{1}{V_F}\left\{uA_x\frac{\partial v}{\partial x} + vA_y\frac{\partial v}{\partial y} + wA_z\frac{\partial v}{\partial z}\right\} = -\frac{1}{\rho}\frac{\partial p}{\partial y} + G_y + f_y \tag{2.2}$$

$$\frac{\partial w}{\partial t} + \frac{1}{V_F}\left\{uA_x\frac{\partial w}{\partial x} + vA_y\frac{\partial w}{\partial y} + wA_z\frac{\partial w}{\partial z}\right\} = -\frac{1}{\rho}\frac{\partial p}{\partial z} + G_z + f_z$$

Where (G_x, G_y, G_z) are the body accelerations and (f_x, f_y, f_z) are the fluid accelerations. The explicit solver solves the viscous stress, σ, pressure, and advection motion. It evaluates the equations using the current time-level values of the local variables.

On the other hand, it solves the local pressures and velocities, which are coupled implicitly, by using the time-advanced pressures in the momentum equations and time-advanced velocities in the mass (continuity) equation. This semi-implicit formulation, however, results in coupled sets of equations that must be solved by iterative techniques which include the Generalised Minimal Residual Method (GMRES). The approximation for the volume of fluid (VOF) function (free surface) in Eulerian grids is given by

$$\frac{\partial F}{\partial t} + u\frac{\partial F}{\partial x} + v\frac{\partial F}{\partial y} + w\frac{\partial F}{\partial z} = 0 \tag{2.3}$$

Wherein *F* is scalar,

$$F = \begin{cases} 1 & \text{if the cell filled fully.} \\ 0 < F < 1 & \text{if the cell filled partially.} \\ 0 & \text{if the cell is empty.} \end{cases} \tag{2.4}$$

And *'h'* is the height of fluid in the cell. For a single fluid with sharp interface solution, the numerical model treats the atmospheric gas region as a void region while the uniform atmospheric pressure boundary condition (BC) is defined as normal at the fluid interface. The numerical model uses one fluid only, *i.e.*, a water droplet. The pressure is assumed to have been specified at the interface surface of a non-fully filled cell. The surface cell pressure ($p_{i,j}$) is set equal to the value obtained from linear interpolation between the desired pressure at the surface (p_s) and a pressure normal (p_N) to inside the fluid can be represented and given by

$$p_{i,j} = \left(1 - \frac{d_c}{d_s}\right) p_N + \left(\frac{d_c}{d_s}\right) p_s \tag{2.5}$$

The improvised Lagrangian method (Barkhudarov, 2003) of the Volume-of-Fluid (VOF) method predicts with higher accuracy for the droplet with advection using three steps. The first step is to approximate the fluid interface in a cell with a planar surface. The second step is to approximate the fluid volume movement according to the local velocity field. For example, the distance dx in the *x*-direction is computed using a second order integration of the equation which is given by

$$\frac{dx}{dt} = \frac{A_x}{V_f} U \tag{2.6}$$

The third step is to compute new fluid fraction values in the computational cells using an overlay procedure where an adjustment of the computed fluid volume could be made. The procedure makes sure that the combined volume of fluid in the acceptor cells is equal to the volume in the donor cell (Barkhudarov, 2003; Hirt & Nichols, 1981).

The net surface tension stresses acting at the sides of the cell is calculated by computing the net surface tension force acting on a surface cell. The surface tension forces are assumed that it can be replaced by an equivalent surface pressure. To compute, *e.g.*, the net *z*-direction force acting on the projected area ($\delta x . \delta y$), the net *z*-direction force is given by

$$S_z = \sigma \int \cos(\theta) \left[\frac{dy}{\cos(\Phi)}\right] \tag{2.7}$$

The θ herein is the angle of the second principal tangent to the *z*-axis and Φ is the angle of the first principal tangent to the *y*-axis. The factor $[dy/\cos(\Phi)]$ is the length of the surface intersecting the face cell.

LBM solves the discrete Boltzmann equation to simulate the flow with collision models. The Boltzmann equation is also known as the Boltzmann transport equation. It describes the statistical distribution of particles in a fluid. It is an equation for the time evolution where the particle distribution function in the phase space. The Boltzmann equation treats every stationary point in a computational domain that stores information. It stores information like its position, (x, y, z) in coordinates and momentums, (p_x, p_y, p_z). As such, the computational domain is known as a phase space, which has six dimensions since every variable is independent of one to another. Each point has the vector notation of $(\boldsymbol{r}, \boldsymbol{p})$ which is equal to (x, y, z, p_x, p_y, p_z).The vector parameter $\boldsymbol{p}$ is also known as 'momenta'. In the computational domain, the discretised space element is written as $(dxdydz \cdot dp_x dp_y dp_z)$ or $(d^3\boldsymbol{r} \cdot d^3\boldsymbol{p})$. Particles or molecules passing through a region in the computational domain over the time (*t*). The probability density function of the particles passing through the region is $f(\boldsymbol{r}, \boldsymbol{p}, t)$ which is per unit phase-space. The function of the distribution gives the probability of finding a particular molecule for a given position and momentum (Perumal & Dass, 2015). The discretised count of the number of particles are $dN = f(\boldsymbol{r}, \boldsymbol{p}, t) d^3\boldsymbol{r} \cdot d^3\boldsymbol{p}$. The total number of particles in that region is stated as $N = \iint\iint\iint f(x, y, z, p_x, p_y, p_z, t) \cdot dxdydz \cdot dp_x dp_y dp_z$. The collision between particles is defined as the rate of change of forces, and is denoted as $\partial f/\partial t$. The classic continuum Boltzmann equation for a single particle distribution function and written as $\partial f/\partial t + \boldsymbol{c}(\partial f/\partial \boldsymbol{r}) + \boldsymbol{F}\,\partial f/\partial \boldsymbol{c} = Q(f)$ wherein $\boldsymbol{c}$ is velocity as derived from $\boldsymbol{p}$, $\boldsymbol{F}$ is the body force and $Q(f)$ is the collision integral. One

of the major problem with LBM is to resolve the collision integral. As proposed by He and Luo (1997), a straightforward expression is the lattice Boltzmann with Bhatnagar–Gross–Krook (BGK) approximation or single-relaxation-time (SRT) model and is given by $Q_{BGK}(f) = -(f - f^{eq})/\tau$ replaces the collision integral. The parameter τ is a typical SRT associated with collision relaxation to the local equilibrium. In the present review, the LBM of isothermal and hydro-dynamics often use three dimensional and 19 velocity lattices, it is written as D3Q19 stencils, with the multi-relaxation-time (MRT) approach as it has higher numerical stability than that of the SRT approach. The evolution equation with MRT collision operator is given by $f_\alpha(\boldsymbol{X} + \boldsymbol{e}_\alpha\delta_t, t + \delta_t) = f_\alpha(\boldsymbol{X}, t) - \sum_{\boldsymbol{\beta}} \boldsymbol{\Omega_{\alpha\beta}} \left(f_\beta(\boldsymbol{X}, t) - f_\beta^{eq}(\boldsymbol{X}, t)\right) + S_\alpha(\boldsymbol{X}, t) - 0.5 \sum \Omega_{\alpha\beta} S_\beta(\boldsymbol{X}, t)$ where f_α is the density distribution function, $\boldsymbol{e}_\alpha$ is the particle velocity in α^{th} direction, f_β^{eq} is the equilibrium distribution function, x is the spatial position, $\boldsymbol{\Omega_{\alpha\beta}}$ is the collision matrix in the velocity space, and δ_t, the time step (Shi & Tang, 2018).

As shown in Figure 2.6, most of the publications regarding droplet sliding down on a surface (type-A) were performed by the researchers through numerical coding while the remaining percentage was conducted by CFD software. In that regard, the "long wave or lubrication approximation" coupled with "disintegrated pressure" (Schwartz et al., 2005) was the most-used and effective method for modelling the 3D droplet movement on a hydrophilic surface. The same method was applied by Ahmed et al. (2014) for non-Newtonian droplets such as blood and PPG silica solutions in the modelling of the droplet spread on an inclined surface. Other numerical coding methods are LBM (Shan & Chen, 1994), the Level Set (Spelt, 2005) and the Cellular Potts Hamiltonian (Oliveira et al., 2011). In modelling droplet sliding behaviour at higher hydrophobicity, the VOF method (Hirt & Nichols, 1981) or software was preferred. For example, Dupont and Legendre (2010) worked on modelling for droplet sliding on superhydrophobic with θ_s of 170° using VOF method namely, JADIM, while Annapragada et al. (2012) modelled droplet sliding

in a moving reference frame (a steady-state condition) on an inclined plane with θ_s of 120° using the VOF method of FLUENT software. Generally, the computational modelling of droplet detachment in a gas-flowed microchannel (type-B) is more complicated. It is a multiphase flow computational modelling where the droplet moves in the microchannel due to the shear and form drag brought on by the difference in gas pressure.

In most cases, the small physical assembly itself limits the observation made on the droplet, especially from the side view and walls. For solution, CFD simulation was used to overcome the difficulty in measuring the θ_s on the walls and GDL layer (Theodorakakos et al., 2006). In Figure 2.6, most of the studies in that category were done using CFD software instead of coding. For example, Zhu et al. (2010), Qin et al. (2012) and Cho et al. (2012) used second-order schemes of FLUENT, while Theodorakakos et al. (2006) used in-house VOF software in Eulerian grids and RANS models [27].

On the other hand, limitations were found in the LBM in modelling the droplet in such conditions. The assumption is that the dynamic viscosity ratio of liquid and vapour are made the same. As such, it constrained the modelling to exhibit high fluidity with high-density ratio (Hao & Cheng, 2010). Later, Li et al. (2013) proposed a forcing scheme of MRT pseudo-potential of LBM, which enables the method to solve with accuracy for density ratio around 500 times. However, it has yet to reach 1000 times to represent the density ratio of water to air. For the category of droplet jumping upon coalescence on a superhydrophobic surface (type-C), most of the previous studies performed numerical coding. Liu and Cheng (2015) and Shi et al. (2015a), who adopted the pseudopotential LBM coupled with MRT collision operator, were able to model the phenomenon, while Farokhirad et al. (2015) used LBM with Cahn-Hilliard diffuse interface theory for simulation of large density ratio. Despite these developments, numerical instability in LBM simulation was still highlighted (Liu & Cheng, 2015; Shi et al., 2015).

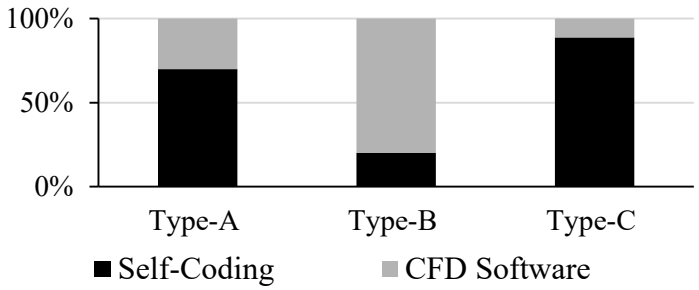

Figure 2.6: Percentage of researchers do coding vs. researchers using CFD software in all types of simulation.

2.2.5 Boundary Conditions and Surface Geometry

In the category of droplet sliding down on a surface, the α commonly used in computational modelling were 30°, 45 ° and 60 ° (Ahmed et al., 2013, 2014; Koh et al., 2009; Annapragada et al., 2012). Other specific inclinations of 6°, 13°, 19°, 26°, 29°, 40 ° and 79° were found in the work of Dupont and Legendre (2010). The smallest α was 4.7° (Oliveira et al., 2011). In the past, computational modelling investigated the droplet sliding down behaviour on a vertical plane (90°) for the hydrophilic surface only (Schwartz et al., 2005; Spelt, 2005). Smooth surface with non-slip boundary condition was mainly defined in most of the computational modelling. For non-smooth surfaces, it was found mainly in the category of droplet jumping upon coalescence on superhydrophobic surface (type-C) *e.g.,* such as cavities, square pillars (Liu & Cheng, 2015; Liu et al., 2014), conical pillars (Shi et al., 2015) and random structures (Zhang & Yuan, 2018). In LBM, the common size of a square pillar shape was 2×2 lattices, 16 lattices in height and with spacing varying from 4 to 28 lattices. For other categories, Oliveira et al. (Oliveira et al., 2011) used ramped pillars for a droplet to slide down.

In computational modelling of droplet detachment in a gas-flowed microchannel for the type-B category, a rectangular cross-section shape of microchannel was used in all of the cases. The common aspect ratio was approximately two units in height to 1 unit in width (Cho et al., 2012; Hao & Cheng, 2010; Qin et al., 2012; Zhu et al., 2010). On the other hand, Zhu et al. (2010) simulated various sizes of micro-channels with aspect ratios

ranging from 1:10 to 2:1. The channel length was found in the range of 0.5mm (Qin et al., 2012) to 5mm (Theodorakakos et al., 2006). The airflow rate in the channel could range up to Re 300. The microchannel with the lowest cross-section height was 0.079mm with airflow rates of 10m/s or Re 90.4. The highest velocity was 15m/s and applied in a 2.7mm x 7mm micro-channel (Theodorakakos et al., 2006).

2.2.6 Mesh Cells and Computational Domain

The common number of mesh cells used in the studies is approximately 500,000 units (Ahmed et al., 2013, 2014; Cho et al., 2012; Shi et al., 2015). In Figure 2.7, it is notable that the total mesh cells or lattices used in simulations increase each year. As a note, the publication related to the mesh dependency study (Koh et al., 2009) is excluded from Figure 2.7. Another interpretation of mesh size is the number of cells per droplet radius. Typically, it was approximately 22 to 40 cells (Dupont & Legendre, 2010; Spelt, 2005). The highest number of cells per radius was 100 units as applied by Schwartz et al. (Schwartz et al., 2005) who use "Longwave or lubrication approximation" coupled with "disintegrated pressure".

For the Lattice Boltzmann method, the computational domain size is measured in the lattice unit. Hao and Cheng (2010) had used 60 lattices per radius. However, Farokhirad et al. (2015) did a grid dependency study and concluded that the use of 25 lattices per radius was sufficiently accurate. The computational domain shape in each type of the simulation was unique to its application. For illustration, the present review cases which uses LBM. The computational domain of *e.g.,* (i) droplet sliding down on a surface (type-A) category shaped like a flat plane with 40×80×80 lattices (Lee et al., 2016), (ii) the droplet detachment in a gas-flowed microchannel (type-B) category shaped like an elongated cube with 60 ×30 ×120 lattices (Hao & Cheng, 2010); the usual cross-section of microchannel is a quadrilateral shape, some are triangular shape with hydrophilic walls

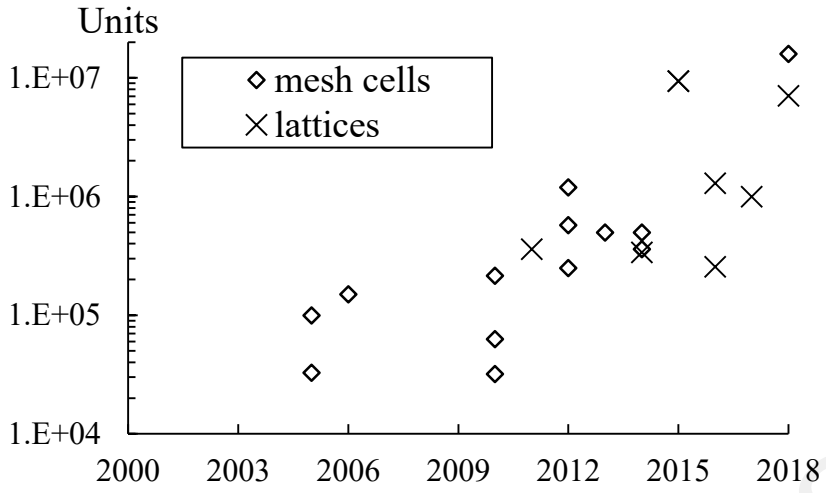

Figure 2.7: The number of mesh cells and lattices used in simulations

(Gopalan & Kandlikar, 2013; Preethi et al., 2014; Zhu et al., 2008) and (iii) droplet jumping upon coalescence on superhydrophobic surface (Type-C) category shaped like tall cube with 192× 192 × 256 lattices (Shi et al., 2015).

2.3 Summary

The topics related to computational modelling of droplet sliding down a surface and the phenomenon of droplet jumping upon coalescence on the superhydrophobic surface are anticipated to increase in the coming years. The future research in those categories are anticipated to focus on mixed types of surfaces with different body forces. It is found that the topics related to the performance or evaluation criteria for the microchannel shapes are still lacking. As for the category of droplet jumping upon coalescence, it is anticipated that the future research will include the influence of air and the actual heat transfer performance on the surfaces.

CHAPTER 3: COMPUTATIONAL MODELLING OF DROPLET SLIDING DOWN ON SMOOTH SURFACE WITH HYDROPHILIC AND HYDROPHOBIC COATINGS

3.1 Introduction

This chapter presents the computational modelling with validations using FLOW-3D®, the commercial software. The subject of validation is to model a water droplet sliding down on an inclined plane. The cases of the modelling use surface conditions of hydrophilic, hydrophobic and super-hydrophobic. For modelling droplet dynamic behaviour on hydrophobic surface, the several computational methods related to the interfacial phenomena were introduced in the past (Ganesan et al., 2017; Islam et al., 2015; Annapragada et al., 2012). The methods were pseudo-Lagrangian method based on the Volume of Fluid - Continuous Surface Force (VOF-CSF) of FLUENT (Annapragada et al., 2012), Lattice Boltzmann method (Hao & Cheng, 2010; Liu et al., 2014; Lee et al., 2016), a fixed grid technique such as the level set (Spelt, 2005) and the VOF with free tracking algorithms method (Hirt & Nichols, 1981).

3.2 Methodology

3.2.1 Governing Equations

The present research uses commercial software, FLOW-3D® (Version of 9.1). The governing equations solve the mass continuity equation, see Equation (2.1); and Navier-stokes equations, see Equation (2.2); where the conditions were isothermal, incompressible, single fluid with gravitation force.

3.2.2 Numerical Method

The free surface in Eulerian grids is solved by Equation (2.3) using the mathematical conditions of Equation (2.4). At the free surface interface, the atmospheric pressure treatment is given by Equation (2.5). Also, the advection of the free surface in

the grids was explained in Section 2.2.4. The residual value of 10^{-4} for the momentum and continuity equations is set as the convergence criteria. A self-correcting numerical treatment of Harlow (1966) was adopted in the software to minimise the accumulation of iteration convergence errors over many time steps. The flow Courant number was ≤1, which is given as the ratio of $\delta t.U/\delta x$, where δt and δx are the time step and the length of the discrete elements respectively. The time step used is 10^{-5}–10^{-6} s throughout the transient simulation.

3.2.3 Droplet Creation

As shown in Figure 3.1, an approximation of the initial droplet shape and its θ_s using an elliptical cap geometry (Wang & Yu, 2012). The droplet volume is given by

$$V = \frac{1}{3}\pi a^2 b(sin^3\phi_o - 3sin\phi_o + 2) \quad (3.1)$$

The radiuses of the droplet were selected to achieve a volume of 30μL at a given θ_s, wherein, $\theta_s = 180° - \phi_o$. The initial droplet height (h_d) and base diameter (d) are given as, h_d=$b(1-sin\phi_o)$ and d=$2acos(\phi_o)$ respectively. The aspect ratio of h/d ranged from 0.416 to 1.866 which increases with θ_s; the droplet height to cavity diameter (h_d/D) was set ranging from 0.9 to 1.6 times approximately.

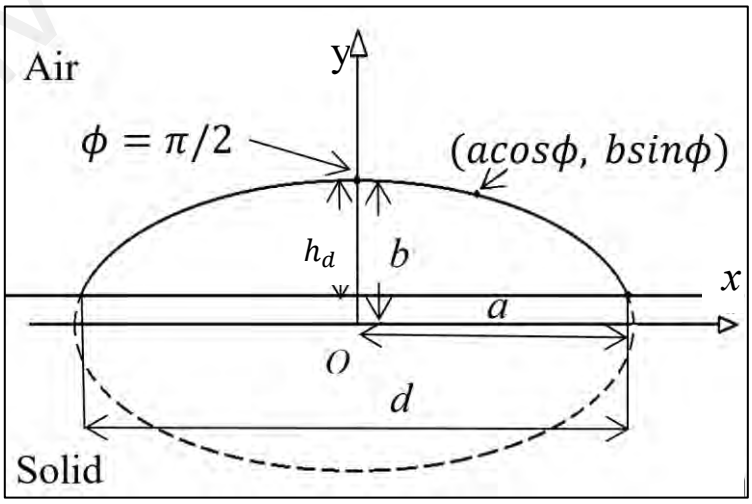

Figure 3.1: Parameters of a droplet geometry.

3.2.4 Initial and Boundary Conditions

At the initial stage of each case study, the droplet was set on a horizontal surface and simulated under the influence of gravity to allow the droplet to reach a settled state (rest condition); then it was set to run based on the governing equations. The differences in θ_s before and after the initial simulation were minimal. Only after that, specific α was introduced for these initial conditions accordingly. The fluid properties - ρ, dynamic viscosity and σ, were 998.2 kg/m^3, 0.001 Pa.s and 0.0728 N/m, respectively (Wang & Yu, 2012). The domain is rectangular with 5mm in width, 100mm in length and 7mm in height. The two-side walls in parallel were 'symmetry' BC and the other walls at the inlet, outlet and top were 'static pressure' BC of 1atm. The droplet contact surface was set as either 'slip or no-slip' BCs depending on the hydrophobicity.

3.2.5 Simulation Cases

The present setup uses a plain surface of 50mm in length and tilted at an angle of 35°. A 30μL water droplet was set to slide down under the influence of gravity. The details of the validation cases, namely S1-C1 to S1-C6, are listed in Table 3.1. Mesh independency study uses the case of S1-C1. The present research investigated different surface conditions, *i.e.*, hydrophilic (θ_s of 79.2º), hydrophobic (θ_s of 98.7º) and superhydrophobic conditions (θ_s of 151.4º). The implication resulted from setting-up the wall boundary conditions (BCs) as 'slip' and 'no-slip' for each surface condition were also studied. For the slip-wall condition, there is no change in the fluid velocity profile. On the no-slip wall boundary, the fluid velocity is zero. The CFD simulation models the no-slip wall by the wall shear stress via direct differentiation. In the later section, the results show that the hydrophilic surface (θ_s of 79.2°) with a no-slip wall BC (the case of S1-C1) and the hydrophobic surface (θ_s of 98.7°) with a slip-wall BC (the case of S1-C4) achieved accurate predictions.

Table 3.1: Details of simulation cases.

Case Name	*wall Condition*	*Surface Condition*	θ_s	θ_s *used in Sakai et al. (2006)*
S1-C1	No- slip	Hydrophilic	79.2°	79.5 °
S1-C2	Slip			
S1-C3	No-slip	Hydrophobic	98.7°	100°
S1-C4	Slip			
S1-C5	No-slip	Super-hydrophobic	151.4°	150°
S1-C6	Slip			

3.3 Results and Discussion

3.3.1 Mesh Dependency Studies

As shown in Figure 3.2, the comparisons were made at a distance vs. *t* travelled by the droplet. The centroid of the droplet was evaluated and used as the reference point. The results from 38980 and 76134 cells per droplet volume (or 10 and 12 cells/mm) are in good agreement with the data of Sakai et al. (2006) within 5% of errors. The mesh number of 38980 cells/ droplet volume (or 10 cells/mm) was selected, and it was applied for most of the cases due to the advantage of lesser computational time. The computational domain with the size of 5mm in width, 50mm in length and 7mm in height, consists of approximately 1.75 million mesh cells. The aspect ratio of each mesh cell is

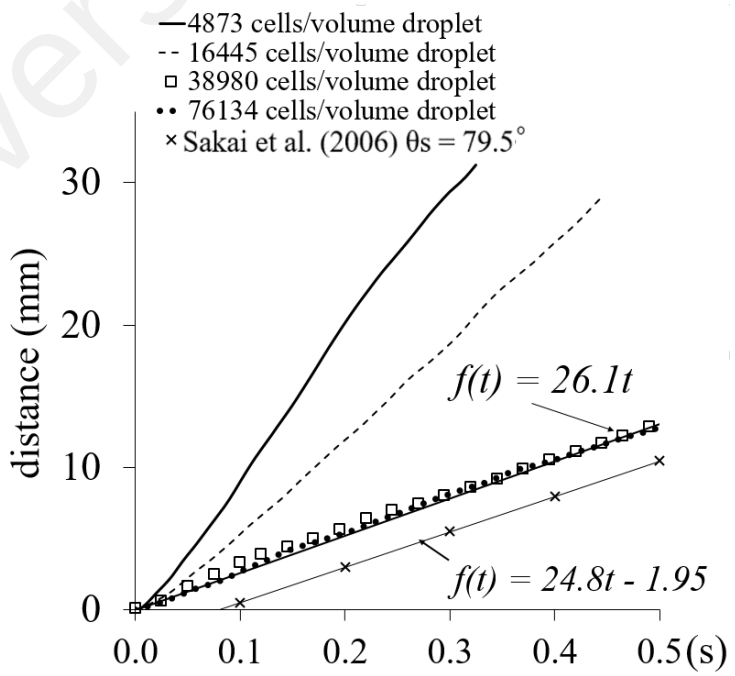

Figure 3.2: Simulations with different cells count are compared with Sakai's experimental result (M Sakai et al., 2006).

one or unity. Mesh sensitivity investigations were carried out by benchmarking S1-C1 validation case (See Table 3.1) and the results from Sakai et al. (2006). Four different number of mesh cells were tested, *i.e.,* about 4873, 16445, 38980 and 76134 cells in 30 μL droplet volume which corresponding to 5 cells/mm, 7.5 cells/mm, 10 cells/mm and 12.5 cells/mm respectively for the computational domain.

3.3.2 Hydrophilic Surface Condition

Figure 3.3 showed the CFD results of the distance travelled by 30μL water droplet on the hydrophilic surface (θ_s of 79.2) tilted to α of 35º angle, with no-slip and slip BCs (S1-C1 and S1-C2 cases). The mass centre of the water droplet was used as the distance travelled by the water droplet in the simulation. For comparison, a similar finding from the experimental investigation of Sakai et al. (2006), which has a regression line of $f(t) = 0.0248t-0.00195$ with the coefficient of determination, R^2 of *0.999*, is included in the figure as well. The CFD result of no-slip BC (S1-C1 case) and its regression line of $f(t) = 26.10t$ (R^2 of 0.9935) is consistent with that of Sakai's. The droplet velocities, which is the slope of these lines, are 26.1 and 24.8 mm/s for the CFD and Sakai's model respectively, with a difference of only 5%. However, on the contrary, the 'slip wall' BC case (S1-C2 case) has a higher slope or droplet velocity, almost two times, in comparison to that of Sakai's, *i.e.,* 40.34 mm/s (Figure 3.3). It is understandable as the 'slip wall' BC conserved the local velocities at the base and therefore allowed the droplet slide fast.

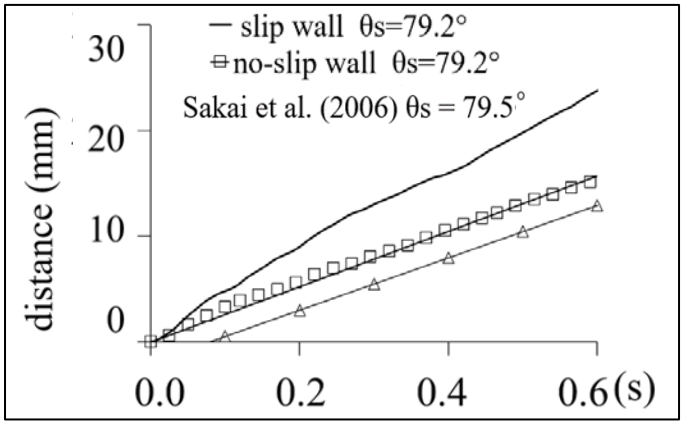

Figure 3.3: Simulation results of droplet travelling on the hydrophilic surface vs. the Sakai's experimental result.

3.3.3 Hydrophobic Surface Condition

The investigation was repeated for a hydrophobic surface (θ_s of 98.7°) with no-slip and slip BCs (S1-C3 and S1-C4 cases). Figure 3.4 shows the temporal distance travelled by 30μL droplet of the CFD cases at α of 35°. Together with a similar finding from the experimental investigation of Sakai et al. (2006), which used two references of advancing and receding points for measurements. Both the profiles of CFD cases with 'no-slip wall' BC (S1-C3) and 'slip wall' BC (S1-C4) in Figure 3.4 showed that the water droplets were accelerating for a short interval of 0.015 seconds before travelling at their constant velocities.

The profiles of simulation cases were close and matching to the experiment findings of Sakai et al. (2006) ranging from *t* of 0s to 0.02s. Also, both CFD results are quite reasonable for the interval from 0s to 0.1s. After that, the CFD case with 'slip wall' BC (S1-C4) settled at a higher constant velocity as compared to the CFD case with 'no-slip wall' BC (S1-C3). Overall, the CFD case with 'slip wall' BC (S1-C4) produced a closer result to Sakai's in comparison to the CFD case with 'no-slip wall' BC (S1-C3). As such, the CFD case with 'slip wall' BC (S1-C4) has a regression line of $f(t)=0.0768t-0.0018$ with $R^2=0.957$ which is closer to the experiment of Sakai et al. (2006) with given as $f(t)=0.1031t-0.0032$ with $R^2=0.999$. The derived constant velocities were 76.8mm/s and 103.1mm/s, respectively. Therefore, BC setting of 'slip wall' will be used to model the hydrophobic surface of θ_s of 98.7°.

3.3.4 Plain Wall vs. Surface Roughness

Through a detailed literature search, the velocity profiles of Figure 3.4 were about 7 to 10 times higher as compared to a similar work by Suzuki et al. (2004). In their work, the droplet velocities were approximately 15.8mm/s and 10.7mm/s. It were derived from our estimations $f(t)=0.0158t+0.0009$ with $R^2=0.9551$ and $f(t)=0.0107t+0.0015$ with

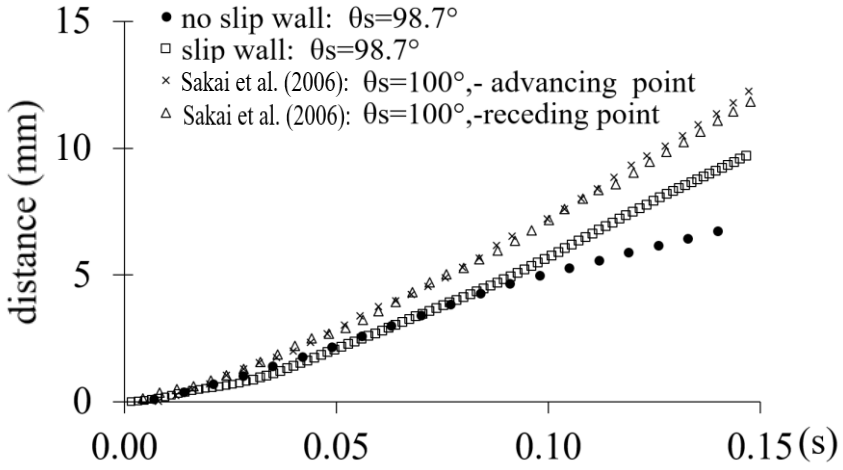

Figure 3.4: Comparisons of simulation results and Sakai's experimental results for the water droplet on the hydrophobic surface.

$R^2=0.9825$ respectively. Suzuki et al. (2004) discovered that the water droplet was experiencing a cyclic motion of elongation and contraction when sliding down the plane. The event could be explained by the high surface roughness used in Suzuki's experiment. In Suzuki et al. (2004), the 30μL water droplet at θ_s of 105° slide down on a hydrophobic surface, coated with Fluoroalkylsilane (FAS-17), with a surface roughness of 4.6nm for inclinations of 32.5° and 37.5°. Meanwhile, Sakai et al. (2006) used a low surface roughness of 0.19nm, Alkylsilane (ODS) material surface, and the water droplet at θ_s of 100° when sliding down at the inclination α of 35°. It showed that the CFD model is able to model the droplet motion on a surface with roughness of 0.19nm even of a lesser one.

3.3.5 Superhydrophobic Surface Condition

Similarly, droplet behaviour was investigated using a super-hydrophobic surface of θ_s of 151.4° on the surface with α as 35°. In Figure 3.5, the CFD cases with no-slip BC (S1-C5 case) and slip BC (S1-C6 case) are unable to predict the experimental results from Sakai et al. (2006). This inconsistency could have resulted from the CFD software itself. The interface between the droplet and its base is modelled as a plain wall with full contact length. The droplet, which rests on the superhydrophobic surface, has short contact length between the substrate and liquid droplet (Gogte et al., 2005).

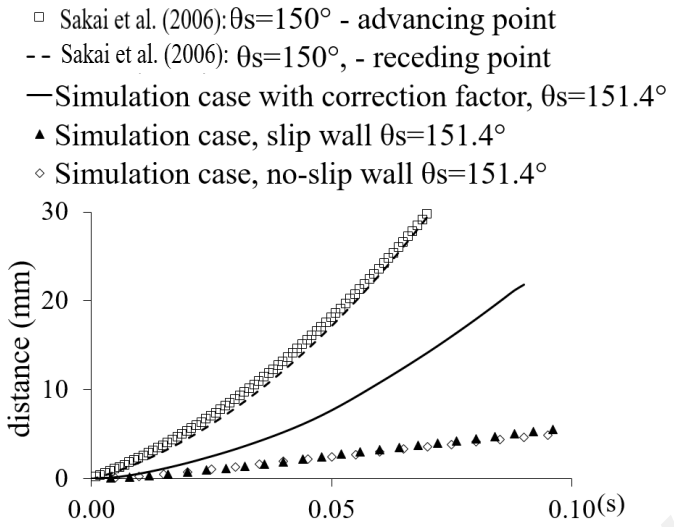

Figure3.5: Comparisons of simulation results and Sakai's experiment findings for water droplets on the superhydrophobic surface.

3.3.6 Droplet Shape Comparison

From Figure 3.6 to Figure 3.8, it showed comparison of simulation cases with Sakai's experimental results at the same distance travelled by the droplets for hydrophilic, hydrophobic and superhydrophobic surface conditions respectively. The pressure

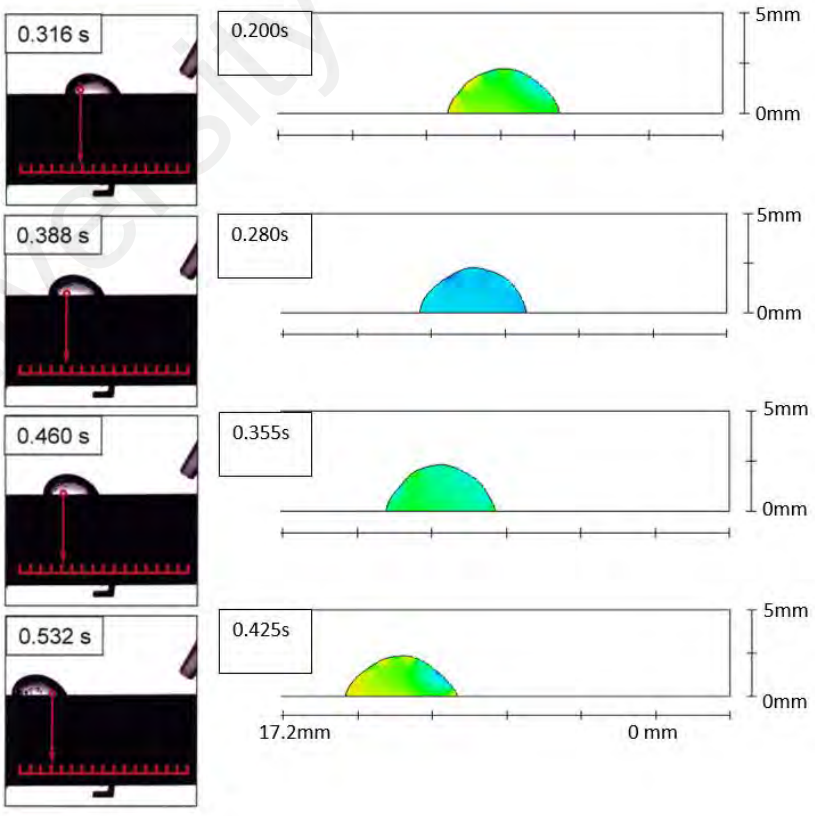

Figure 3.6: A series of images were experimental results by Sakai et al. on the left (θ_s of 79.5º). Present simulation results on the right (θ_s of 79.2º) in sliding down at α of 35º.

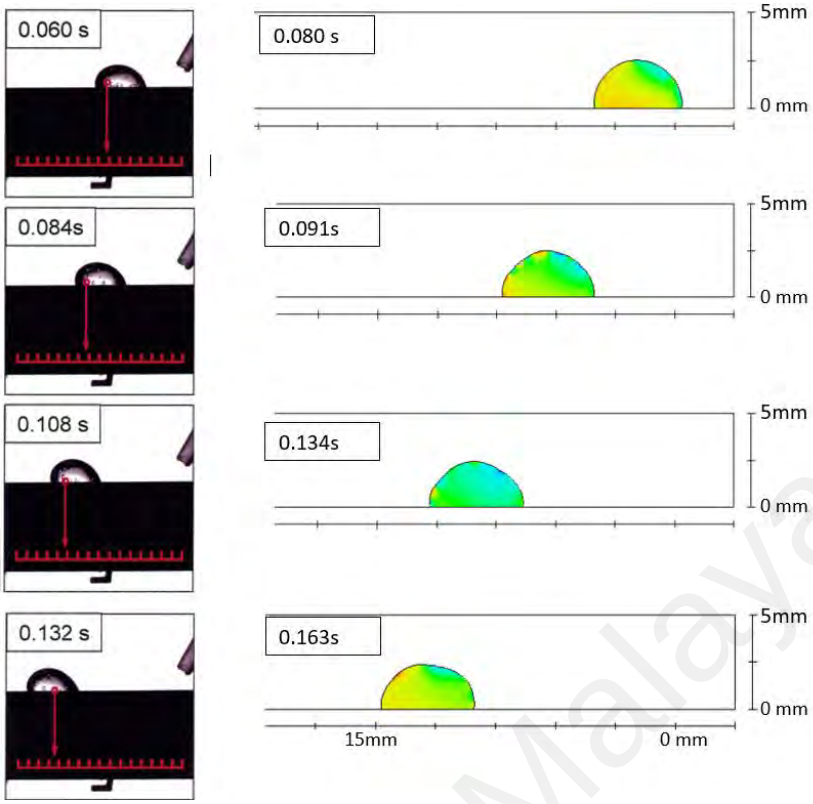

Figure 3.7: A series of images were experimental results by Sakai et al. on the left (θ_s of 100º). Present simulation results on the right (θ_s of 98.7º) in a sliding down angle at α of 35º.

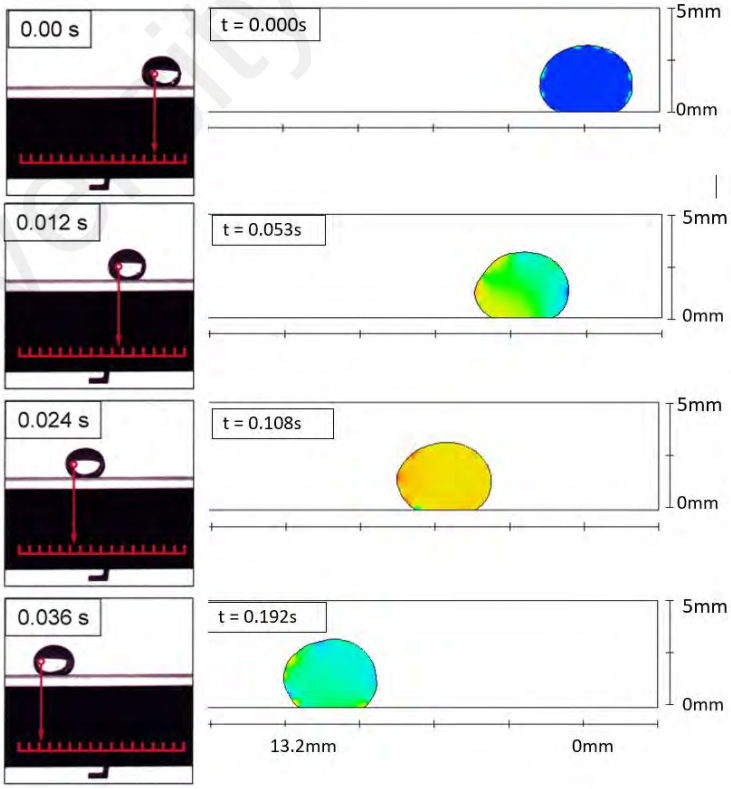

Figure 3.8: A series of images were experimental results by Sakai et al. on the left (θ_s of 150º). Present simulation results on the right (θ_s of 151.4º) in a sliding down angle at α of 35º.

contours in simulation images do not signify any point for discussion. In the hydrophilic and hydrophobic cases (S1-C1 and S1-C4 cases), the shape of the droplet in the CFD model appears to be close to an actual droplet, but they have small deformation on the top. However, such differences are less noticeable for the CFD droplet model with the surface cavities profile. The droplet shape from the CFD model of the superhydrophobic (S1-C6) case appears to be accurate with slight elongation.

3.4 Summary

The ability of software in the modelling of the hydrophilic surface of θ_s of 79.2^o and hydrophobic surface of θ_s of 98.7^o is accurate based on the comparisons with the literature findings. The latter requires a modification of the interface boundary wall into a 'slip' type. The modelling of the super-hydrophobic surface with θ_s of 151.4^o showed accurate droplet shape but the kinematic profile was inaccurate. The inconsistency was resulted due to the limitation of CFD software. In the CFD modelling, the droplet conformed fully with the plain wall at the base whereas the real droplet rests with short contact length on the superhydrophobic surface. The short contact length gives a very little resistance for the real droplet to slide freely on the surface.

CHAPTER 4: COMPUTATIONAL MODELLING OF DROPLET SLIDING DOWN ON CAVITIES SURFACES WITH HYDROPHILIC AND HYDROPHOBIC COATINGS

4.1 Introduction

This chapter present a CFD simulation study on cavity fillings resulting from a sliding droplet on a titled substrate with round-shaped cavities in a serial arrangement as shown in Figure 4.1. The present research investigated the effects of different hydrophobicity for different cavity and non-cavity surfaces, cavity depths, cavity spacing, tilting angles of the substrate and initial droplet volumes on the droplet mobility. The findings report the total number of filled cavities, its duration and the average volume of droplet per cavity.

A comparison is compiled in Table 4.1. Lin et al. (2018) investigated the generation of nanoliter droplets from a horizontal movement of one liquid source. Meanwhile, Chang et al. (2016) investigated the generation of an array of nanoliter droplets through sliding down motion on a substrate. Lin et al. (2018) investigated the generation of nanoliter droplets from a horizontal movement of the liquid source (from a volume of liquid or injector) on a surface with hydrophilic-hydrophobic coating in a specific pattern. On the other hand, Chang et al. (2016) investigated the generation of an array of nanoliter droplets through sliding down motion of a larger droplet on a tilted substrate (or gravity-induced) with hydrophilic-hydrophobic coatings.

In the present work, the generated droplet volume is approximately 230 times larger than the evaluated droplets of Chang's. The droplet sizes generated in both Chang's and Lin's are close within the nanoliter scale. However, the present work uses initial droplet volume 2 to 5 times smaller in comparison to Chang's. Both Lin and Chang used a straight substrate with the patterned hydrophobic/hydrophilic surface while the present research uses a substrate with cavities of different hydrophobicity. The main surface of

all these studies used hydrophobic coating, where the generated droplets retain on hydrophilic patterned surfaces. The common result is the average generated droplet volume ($\overline{v}_c$). Chang's data and the present research varied the spacing where the droplets are generated or deposited. In both the results, droplet velocity increased with the spacing since the moving droplet gained momentum during the sliding down motion on a longer path.

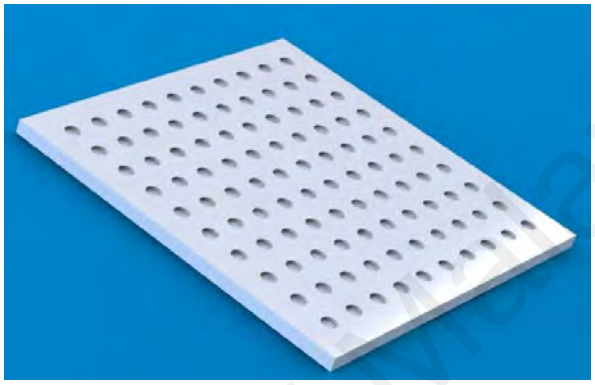

Figure 4.1: Substrate with cavities.

Table 4.1: Details of different studies.

Category	Parameters	Lin et al.'s	Chang et al.'s	Present research
Method	Energy source	Moving source	*g*-force	*g*-force
Droplet Volume	V_i (μL)	-	150	30-60
	$\overline{v}_c$ (μL)	0.002-0.017	0.011-0.016	2.52-7.09
Hydrophobic main surface	Geometry	Straight	Straight	Cavities
	$\theta_{s,nc}$	87°	170°	98.7°
	Spacing (mm)	-	0.20 to 20	5-10
	α	Horizontal	α from10° to 50°	α from 35°to 89.5°
Hydrophilic surface	$\theta_{s,c}$	-	30°	20° to 98.7°
	shape	round	Square	round
	area (mm^2)	Less than 0.38	0.25	3.90
Varied parameters	α	-	-	Yes
	V_i	-	-	Yes
	$\theta_{s,nc}$	-	-	Yes
	$\theta_{s,c}$	-	-	Yes
	S	-	Yes	Yes
	μ	Yes	-	-
	injector speed	Yes	-	-

4.2 Methodology

4.2.1 Model Setup

This chapter uses the same governing equations, numerical methods, droplet creation method, initial and boundary conditions as described in Section 3.2. As shown in Figure 4.2, the model geometry consists of 10 round cavities at an in-line position to each other. The round cavities has a diameter (D) of 2.227 mm and the cavity depth t_c of 0.5 mm. In default, the geometry uses these dimensions. The same simulation software, as mentioned in the previous chapter, was used in the work of this chapter. The centreline of the droplet is the symmetrical boundary. The open boundaries defined as static pressure.

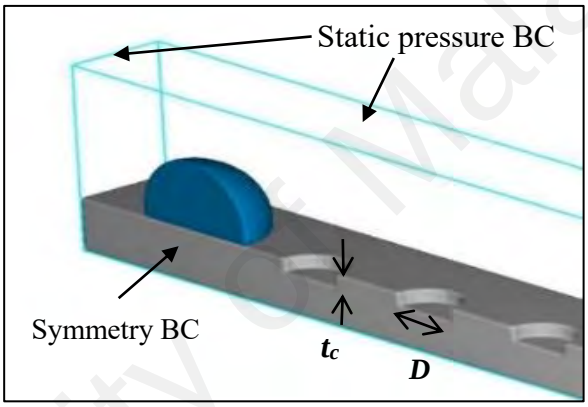

Figure 4.2: Model of water droplet and substrate in the computational domain. The symmetrical boundary is located at the centre half of the cavities. Other sides are defined with static pressure boundaries.

4.2.2 Simulation Cases

As shown in Table 4.2, the present research investigates the variables such as different hydrophobicity configurations (S2 cases), the θ_s of cavity surface (S3 cases), cavity depths (S4 cases), cavity spacing (S5 cases), α (S6 cases) and initial droplet volume (S7 cases). For S2 cases, the cavity and non-cavity surfaces were set-up as either hydrophilic (θ_s of 79.2°) or hydrophobic (θ_s of 98.7°) and vice versa, which resulted in four different combinations. The most effective configuration in generating droplets, *i.e.,* S2-C4 case, was selected for further studies after that.

For S3 cases, only the cavity surface contact angle ($\theta_{s,c}$) was varied, *i.e.,* 20º, 40º, 60 º and 79.2º. For S4 cases, the present research varies the cavity depth from 0.1, 0.5, 1.0 and 1.5 mm; and in comparison with the cavity diameter (D) of 2.227mm, it is about 4.4% to 67% smaller. In S5 cases, the present research varies the spacing between cavity (S) from 2.5, 5, 7.5 and 10 mm; and in comparison with the cavity diameter, it is about 1 to 4.5 times larger in length. For S6 cases, the present research varies the substrate tilt angle (α) from 35º to 89.5º. Finally, for S7 cases, the initial droplet volume (V_i) was varied from 15μL to 60μL.

In the present research, some particular parameters are used to evaluate the performance of the cavity based substrate design for droplet generation; they are (i) the average t taken for generating a droplet (t_g/N) where t_g is the total t taken from the

Table 4.2: Details of simulation cases and results.

Case Name	*Parameters*						*Simulation Results*			
	$\theta_{s,nc}$	$\theta_{s,c}$	t_c mm	S mm	α	V_i (μL)	N	t_g (s)	t_g/N (s)	$\overline{v}_c \pm \sigma_{SD}$ (μL)
S2-C1	79.2°	79.2°	0.5	5	35°	30	0			
S2-C2	98.7°	98.7°					0			
S2-C3	79.2°	98.7°					0			
S2-C4	98.7°	79.2°					1	0.16	0.16	2.52
S3-C1	98.7°	79.2°	0.5	5	35°	30	1	0.16	0.16	2.52
S3-C2		60.0°					4	0.34	0.09	3.32± 0.77
S3-C3		40.0°					4	0.34	0.09	3.92± 0.77
S3-C4		20.0°					4	0.36	0.09	3.90±0.53
S4-C1	98.7°	20.0°	0.1	5	35°	30	5	0.39	0.08	3.81±0.66
S4-C2			0.5				4	0.36	0.09	3.90±0.53
S4-C3			1.0				2	0.23	0.12	5.41±0.20
S4-C4			1.5				1	0.14	0.14	7.09
S5-C1	98.7°	79.2°	0.5	2.5	35°	30	6	0.52	0.09	2.71±0.17
S5-C2				5			1	0.16	0.16	2.52
S5-C3				7.5			1	0.24	0.24	2.65
S5-C4				10			1	0.24	0.24	2.65
S6-C1	98.7°	79.2°	0.5	5	35°	30	1	0.16	0.16	2.52
S6-C2					50°		3	0.27	0.09	3.16±0.21
S6-C3					70°		6	0.40	0.07	3.31±0.72
S6-C4					89.5°		7	0.24	0.03	2.77±0.32
S7-C1	98.7°	79.2°	0.5	5	35°	15	1	0.25	0.25	2.90
S7-C2						30	1	0.16	0.16	2.52
S7-C3						45	7	0.79	0.11	2.54±0.13
S7-C4						60	10	1.04	0.10	2.39±0.11

beginning (t of 0) to the moment at which the last generated droplet separated from the substrate, wherein N is the number of the generated droplets and (ii) the average volume per cavity ($\overline{v}_c$) with the exclusion of last retaining or moving droplet. These parameters are essential in designing a substrate; it provides estimation like the initial droplet size and the duration of filling for N number of cavities.

4.3 Results and Discussion

4.3.1 The Effect of Different Configurations in Hydrophobicity

In this section, the results from CFD models of S2 cases (Table 4.2), which consist of cavities on the surface, and the cases S2-C1 to S2-C4 of different conditions of hydrophobicity will be discussed. Refers to Figure 4.3, which shows the droplet mobility in temporal sequence for the S2-C2 model, the droplet has limited mobility in which it moved from its initial position (t of 0s) and filled in the first cavity (t from 0.06 to 0.09s). After that, the droplet was only able to advance near the 2nd cavity inline, but it was unable to fill the cavity (t from 0.12s to 0.15 s). Beyond t of 0.15s, the droplet does not move further. Note that, the results of cases S2-C1, S2-C2 and S2-C3 are similar and therefore only those from S2-C2 is given herein.

However, in S2-C4 model, which has the non-cavity surface with θ_s of 98.7° (hydrophobic) and the cavity surface with θ_s of 79.2° (hydrophilic), the droplet behaviour is different from that obtained in S2-C2. In Figure 4.4, the droplet moves faster and filled two cavities in inline comparatively. For example, the droplet of S2-C4 has moved into the 1st cavity within t of 0.06s and subsequently, the 2nd cavity at t from 0.09s to 0.15s. The droplet shape profile, particularly at t of 0.12s, showed an elongated shape which bridged between two cavities (Figure 4.4) while sliding over. This finding shows that a sudden change in droplet θ_s in the specific order of, lower surface energy (*i.e.,* hydrophobic surface) to the higher surface energy (*i.e.,* hydrophilic surface) enhances the droplet mobility.

Further evidence of such a phenomenon was observed in the S3-C4 case of Figure 4.5, where the droplet was slipping forward effortlessly at t equals to 0.04s and 0.08s. According to the law of conservation of energy, the droplet on the hydrophobic surface gained more kinetic energy or increased in speed when it entered and moved along the hydrophilic surfaces in the cavity. The potential energy stored in the droplet surface tension was released or converted into kinetic energy as the θ_s changes from a higher θ_s to a lower θ_s in the cavity (Xu et al., 2016). In the present research, it showed the potential in the development of an effective and fast means of droplet generation in cavities.

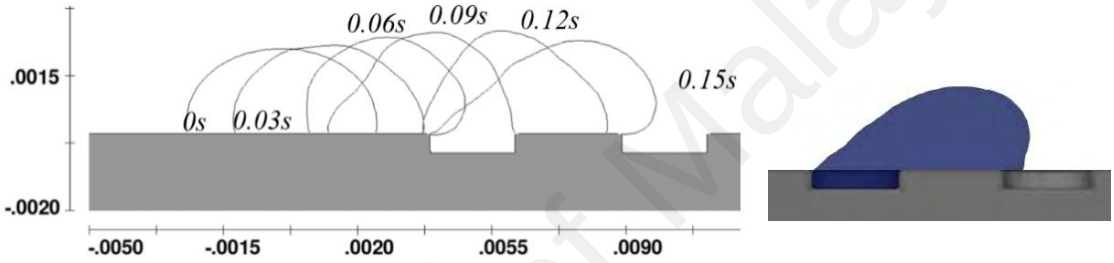

Figure 4.3: Droplet of S2-C2 case which filled the first cavity and stopped near the second cavity. The scale on the vertical axis and horizontal axis are given in unit meter (on the left). The figure shows the final condition at t_∞ (on the right).

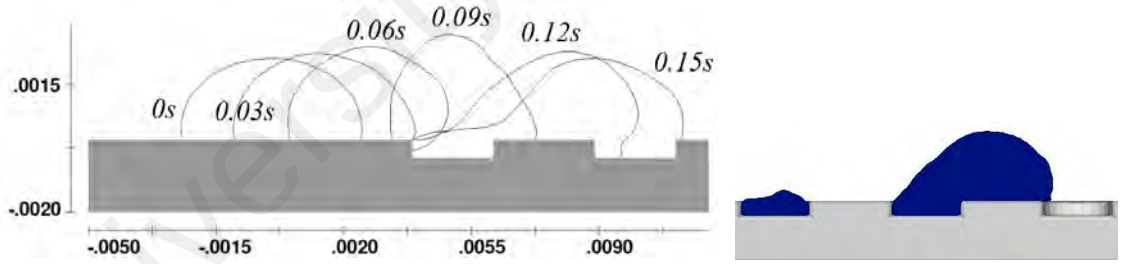

Figure 4.4: Time series of droplet free surface line for S2-C4 case. The scale on the vertical and horizontal axis are given in unit meter (on the left). The figure shows the final condition at t_∞ (on the right).

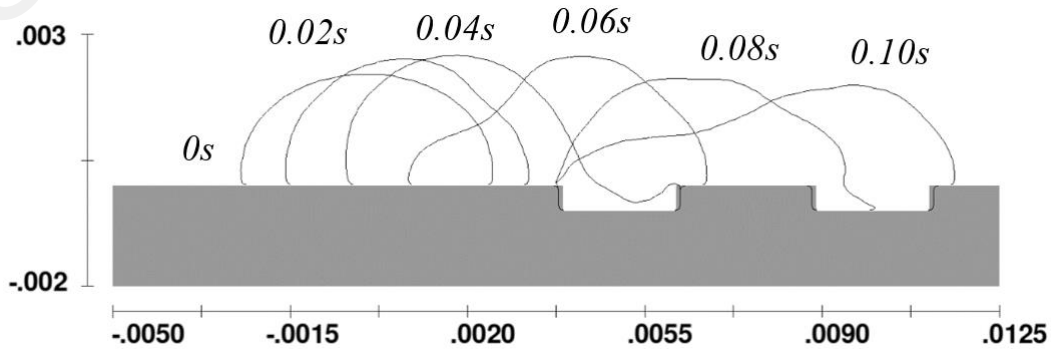

Figure 4.5: Time series of droplet free surface line for S3-C4 case slip forward free surface at t of 0.04s and 0.08s. The scale on the vertical and horizontal axis are given in unit meter.

4.3.2 The Effect of Different Hydrophobicity for Cavity Surfaces

The cavity hydrophobicity, measured by the static θ_s, is varied from $\theta_{s,c}$ from 20° to 79.2° in S3 cases (see Table 4.2). In these cases, the surface energy of cavities is increased or made more hydrophilic as compared to the previous study. Herein, the implication of such changes on droplet generation is investigated using several cavities filled (N), the total duration (t_g) for N number of generated droplets, the duration per cavity (t_g/N)and the average volume per cavity ($\overline{v}_c$). Note that all of these parameters exclude the volume of the last droplet at the downstream. For example, referring to Figure 4.6 (a), N of 1, $t_g$of 0.22s, t_g/N of 0.22s and $\overline{v}_c$ of 2.52 μL.

Table 4.2 summarises such results for S3 cases, and Figure 4.6 shows the graphical representation. The reduction of cavity $\theta_{s,c}$ from 79.2° to 60° has resulted in a sudden and significant increase in N, *i.e.,* from 1 to 4. Similarly, $\underline{v_c}$ has increased from 2.52 to 3.32 ± 0.77 μL (mean ± standard deviation). The difference in the droplet volume comparing from one cavity to the other is about 20% only, suggesting a reasonable consistency. However, a further reduction on cavity θ_s (≤ 60°) has resulted in no changes on N and minor increase on $\underline{v_c}$ which is roughly about 3.9 μL. The only obvious difference is the profile or shape of the last droplet at the downstream; those of $\theta_{s,c}$ of 20° (S3-C4) case is relatively more asymmetric (or with a tail) near the cavity region. In general, this result suggests that under the given set-up condition, a small reduction of cavity θ_s to a value below 60° is sufficient to achieve more numbers of cavity filling or droplet generation. Figure 4.7 shows the profiles of kinetic energy (KE) in the computational domain for different cases of S3. The KE graphs started at origin for all cases. Before t of 0.03s, small differences in the KE profiles were caused by the fluctuation on the droplet-free surface. The kinetic energy of the droplet increases six(6) times higher than before sliding into the first cavity. The KE of the S2-C2 case has the lowest KE among all cases.

Meanwhile, the KE in the S3-C1 case, which has a lower cavity surface $\theta_{s,c}$ of 79.2°, exhibited higher KE with two noticeable peaks as it filled two cavities. The first peak was seen at the time interval between 0.060s and 0.135s while the second peak appeared between 0.135s and 0.165s. The highest KE happened in the S3-C4 case, which the cavity surface $\theta_{s,c}$ of 20°, with five filled cavities. The peaks are located at 0.06s, 0.09s and, 0.12, 0.15s and 0.18s when observed closer.

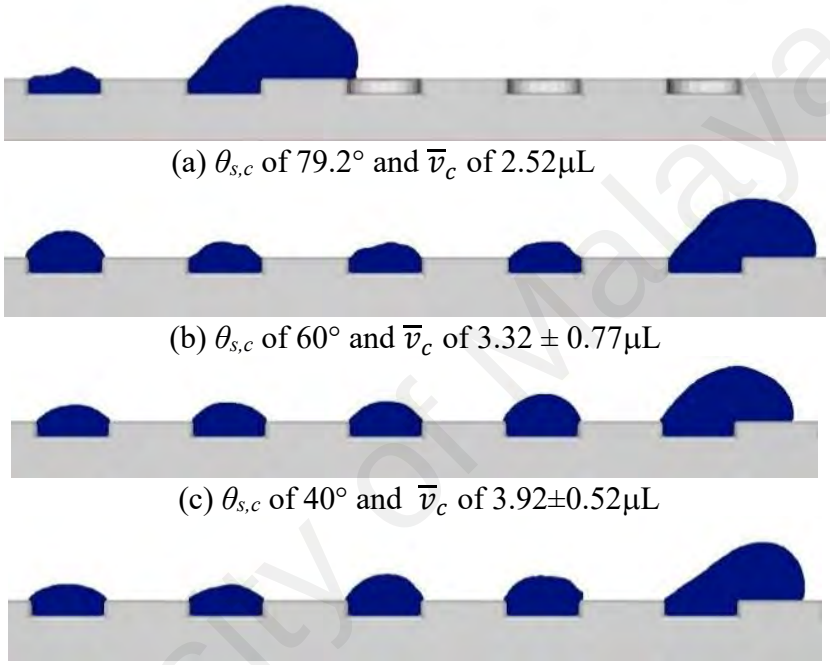

(a) $\theta_{s,c}$ of 79.2° and $\overline{v}_c$ of 2.52μL

(b) $\theta_{s,c}$ of 60° and $\overline{v}_c$ of 3.32 ± 0.77μL

(c) $\theta_{s,c}$ of 40° and $\overline{v}_c$ of 3.92±0.52μL

(d) $\theta_{s,c}$ of 20° and $\overline{v}_c$of 3.90±0.53μL

Figure 4.6: Images of S3 are presented in (a) to (d), respectively. Images are taken at t_∞.

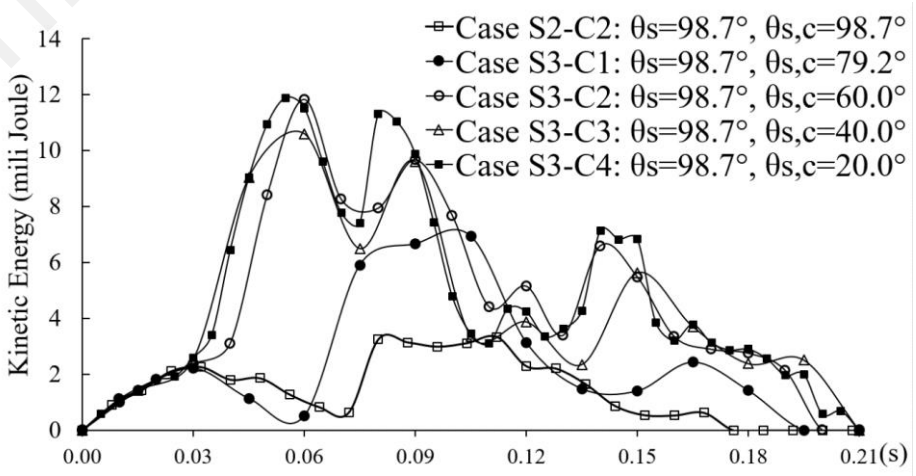

Figure 4.7: Kinetic energy profiles in the computational domain of S3 cases.

It is observed that the differences in KE profiles for S3-C2, S3-C3 and S3-C4 cases were small and seemed to have to reach an optimal condition. Overall, the KE of the cases increases with the decreasing $\theta_{s,c}$ in the cavity surface. The gradual decrease in the heights of the peaks is due to the moving droplet, which travelled with lesser mass after filling each cavity subsequently.

4.3.3 The Effect of Different Cavity Depth

As shown in Figure 4.8 (a) to (d), the effect of cavity depths (t_c), *i.e.*, 0.1, 0.5, 1.0 and 1.5mm on droplet mobility and cavity fillings are investigated and presented as S4 cases. The non-cavity and cavity surfaces have θ_s of 98.7° and θ_s of 20° respectively. The results of N, t_g, t_g/N and $\overline{v}_c$ of S4 cases are tabulated in Table 4.2 as well. In general, with the increase of the cavity depth, the number of the cavity filled, N reduces. For example, at t_c of 0.1mm (shallow cavity), N is 5, but when $t_c$of 1.5 mm (deep cavity), N is equal to only 1. It is understandable that a deep cavity can hold a larger fluid volume and impedes the droplet mobility. It reflected from the results of $\overline{v}_c$, which increases with

(a) t_c of 0.1mm and $\overline{v}_c$of 3.81±0.66μL

(b) t_c of 0.5mm and $\overline{v}_c$of 3.90±0.53μL

(c) t_c of 1.0mm and $\overline{v}_c$of 5.41±0.20μL

(d) t_c of 1.5mm and $\overline{v}_c$ of 7.09μL

Figure 4.8: Each case has a different cavity depth. The plane slope tilted at α of 35°. The non-cavity surface θ_s of 98.7° and the cavity surfaces $\theta_{s,c}$ of 20°. Images are taken at the final moment (t_∞).

the increase of t_c. For example $\overline{v}_c$=3.81±0.66 and 7.09 μL for t_c of 0.1 and 1.5 mm respectively. Referring to t_c of 1.5 mm (S4-C4) case (d) in Figure 4.8, there is an incomplete cavity filling (or over-flowed) condition for cavity no. 3 and therefore only one cavity (the first one) is considered as *N* equals to unity for the present research.

4.3.4 The Effect of Different Cavity Spacing

In S5 cases (Table 4.2), the spacing between cavities (*S*) was varied from 2.5, 5, 7.5 and 10 mm, which was about 1 to 4.5 times larger in length when compared with the cavity diameters. The non-cavity and cavity surfaces had $\theta_{s,nc}$ of 98.7° and $\theta_{s,c}$ of 79.2°, respectively. As shown in Figure 4.9, the case with S of 2.5mm, which is shorter than the cavity diameter, eight of the cavities have been filled, but the last two cavities are bridged together. Hence, only six generated droplets are counted (*N* of 6) with $\overline{v}_c$ of 2.71±0.71 μL. However, this is not for the case where S≥0.5 mm and in which only one cavity has been filled (*N* of 1) with $\overline{v}_c$ranging from 2.52 to 2.65 μL. The $\overline{v}_c$ values of the cases are quite close to each other; this suggests a cavity with a specific depth that can capture a consistent amount of droplet in the cavity.

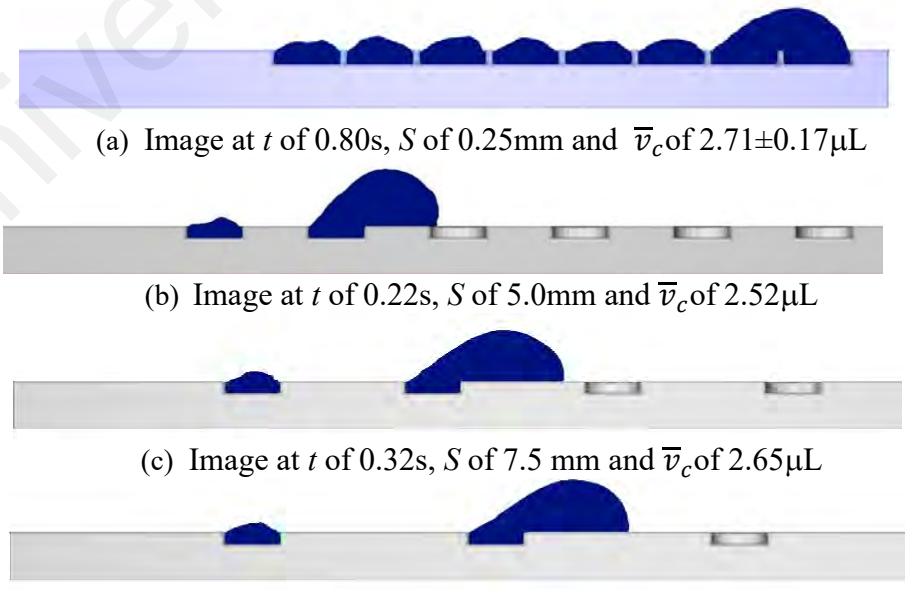

(a) Image at *t* of 0.80s, *S* of 0.25mm and $\overline{v}_c$of 2.71±0.17µL

(b) Image at *t* of 0.22s, *S* of 5.0mm and $\overline{v}_c$of 2.52µL

(c) Image at *t* of 0.32s, *S* of 7.5 mm and $\overline{v}_c$of 2.65µL

(d) Image at *t*=0.50s, *S*=10.0mm and $\overline{v}_c$of 2.65µL

Figure 4.9: Final moment (t_∞) when the water droplet stopped sliding down for different cavity spacing. The plane slope tilted at α of 35°. The non-cavity θ_s of 98.7° and the cavity θ_s of 79.2°.

4.3.5 The Effect of Different Tilted Angle

For S6 cases, the effect of α ranging from 35° to 89.5°, on droplet mobility and cavity fillings was investigated. Figure 4.10 presented a series of images where the droplet in the S6-C3 case was sliding across the substrate. See Table 4.2 for the results of *N*, t_g, t_g/N and $\overline{v}_c$. As expected, an increase in the tilt angle resulted in the increase of the number of filled cavities (*N*), e.g., *N* of 1, 3, 6 and 7 as for α of 35°, 50°, 70° and 89.5° respectively. Similarly, $\overline{v}_c$ increases with the increase of α. The increase of $\overline{v}_c$ is larger for α within the range from 35° to 50°. Non-linearity behaviour was observed in the changes of t_g/N and $\overline{v}_c$ with the increase of α. At a more significant inclination, the droplet slides down with higher momentum and caused a lesser duration in overcoming the surface tension during separation before the droplet moved to the next cavity. As seen in S6-C4, lesser liquid volume was generated (left) in the cavity due to fast separation.

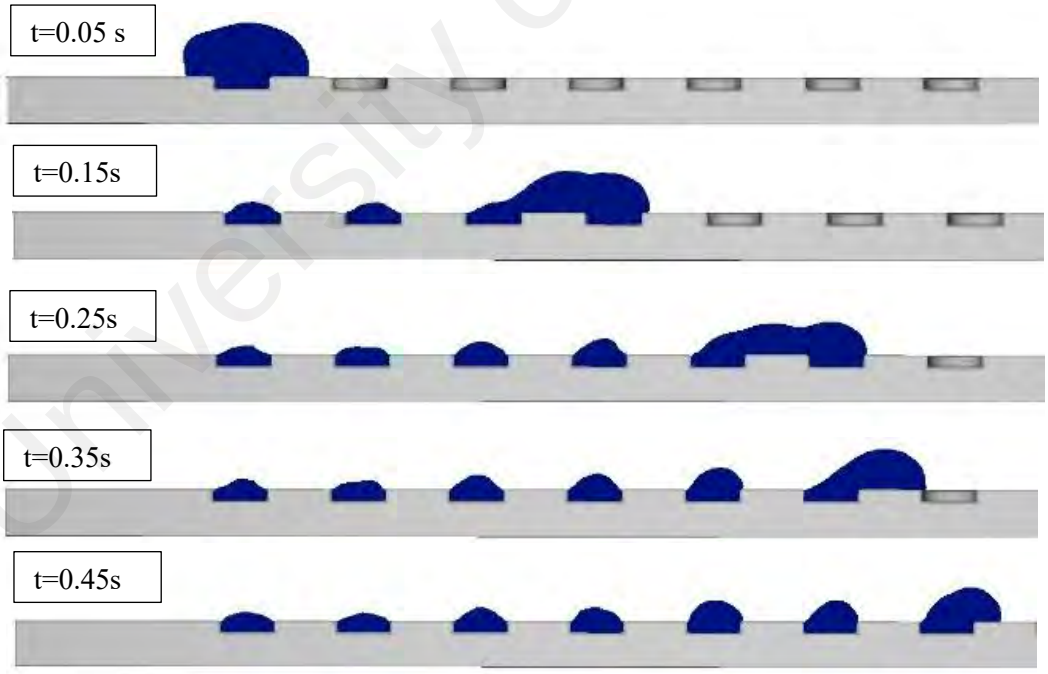

Figure 4.10: In the case of S6-C3, the droplet filled all seven cavities and stopped at t of 0.45s. The substrate geometry parameters are *S* of 5mm, t_c of 0.5mm and α of 70°.

4.3.6 The Effect of Different Initial Droplet Volume

The effect of the volume of the initial droplet (V_i) was investigated using S7 cases in which 15 – 60 μL were tested. See Table 4.2 for the results of N, t_g, t_g/N and $\overline{v}_c$ for cases S7. In general, more numbers of cavities were filled (N) with a larger droplet volume, *e.g.*, N of 1, 1, 7 and 10 as for V_i of 15, 30, 45 and 60 μL respectively. However, $\overline{v}_c$ reduces with the increase of V_i. A larger initial droplet has a higher momentum as it slides downward and therefore resulted in a smaller t_g/N. Larger droplet has a higher momentum as it slides downward and it resulted in a shorter duration for the moving droplet separate from the cavity. Therefore, it resulted in a smaller t_g/N.

4.4 Summary

A detailed study on droplet mobility and cavity fillings resulted from a tilted surface or substrate with cavities were carried out by CFD mean using FLOW-3D® software. For a tilted plate or substrate with cavities, comparatively, the coating of the non-cavity surface with θ_s of 98.7° (hydrophobic) and the cavity surface with θ_s of 79.2° (hydrophilic) will enhance (or speed up) the droplet mobility and cavity filling. The reduction of the cavity hydrophobicity from θ_s of 79.2° to θ_s of 20° does not have a linear effect in term of improving droplet mobility and cavity filling; Reducing θ_s from 79.2° to 60° resulted a large number and volume of cavity filling and, however, there is no further improvement beyond $\theta_s \leq 60°$. A deep cavity can hold-up a larger volume of fluid, which directly impedes the droplet mobility and cavity filling further downstream. The effect of the gap size between the two cavities is negligible provided that the gap is more than two times larger than the cavity diameter. An increase of the plate α gives an incremental effect on droplet mobility and cavity filling. An increase of the initial droplet volume increases the number of the cavity filled but decreases the cavity filled volume.

CHAPTER 5: COMPUTATIONAL MODELLING OF WATER RETENTION ON POROUS GEOMETRIES WITH HYDROPHILIC AND HYDROPHOBIC COATINGS

5.1 Introduction

A regular 3D geometry requires four independent information for a complete identification. One of those is the shape or structure type and the other three are the dimensional variables, *e.g.,* a cuboid has width, height and length while an ellipsoid has three different radiuses. In the case of metallic foam, the interior shapes itself can be viewed as variables. Besides the PPI and ϕ, the present research proposed two more variables for quantifying the interior shapes; *i.e.*, the structural homogeneity and the number of junctions. In the present research, water retention behaviour of two different porous structures, *i.e.*, an actual porous metal which obtained using the Micro-Computed Tomography scan, and an ideal geometry were investigated using CFD software. The present research models a decreasing water level in a reservoir consisting the porous structure in stationary. It mimics the setup used in dynamics dip-testing which measures the amount of retained water for different types of fins-tubes heat exchangers.

5.2 Background

Indirectly, a fins-tubes type of heat exchanger is a porous structure with high porosity and surface area. In the cooling and dehumidifying application, the condensates grow on the heat exchanger surfaces. The ability for condensates to allow drainage depends on the shapes of fins and tubes in the heat exchangers. The standard performance test for heat exchanger uses wind-tunnel and it is relatively expensive in terms of time and material costs (Liu & Jacobi, 2008). Alternatively, 'dynamics dip-testing' offers a fast, preliminary test and cost-effective way to check the order of water retention for fins-tubes types of heat exchangers (Zhong et al., 2005). In a dynamics of dip-testing, the fins-tube heat exchanger is fully-submerged in a reservoir of water. The weight measurement

device is used to record the weight of heat exchanger throughout the test while the water is being drained-off from the bottom of reservoir.

The retained water volume on a heat exchanger varies with different *U*, surface wettability, gravity direction, and interiors geometry features (Ganesan et al., 2016; Joardar et al., 2004; Liu & Jacobi, 2008; Zhong et al., 2005). In terms of the interaction forces, it involves viscous forces, gravity force, and fluid surface tension force. Generally, a heat exchanger in a slanted position retains water by 20% lesser (Joardar et al., 2004) compared to one in a vertical position. The heat exchanger of a round-tube type has more rapid drainage than a flat-tube one (Zhong et al., 2005) while the retained water volume on the heat exchanger of a round-tube type increases with the surface wettability, it is the opposite for a flat-tube type (Liu & Jacobi, 2008). Recently, a metallic foam was used in the dynamics dip-testing (Hu et al., 2017). Hu et al. (2017) found that the retained volume of water on metal foam surfaces, was higher in those specimens of a higher PPI and also with a longer submerged length. However, the retained volume of water was lower in those specimens of a higher porosity or hydrophobicity (Hu et al., 2017).

5.3 Methodology

5.3.1 Porous Metal and Ideal Geometry

Metallic foam is a non-uniform porous medium. It has a high ratio of stiffness to the weight that gives an attractive geometry property for the used in many applications (Banhart, 2001; Banhart, 2013; Lefebvre et al., 2008; Liebscher et al., 2013). Usually, the structural characteristic of metallic foam is measured by PPI and porosity (ϕ). Upon closer inspection, a metallic foam has a random or non-homogeneous structure due to the complexity during the formation stage (Babcsán et al., 2003; Raj, 2011; Repossi et al., 2015). In the past, Tetra-kai-decahedron was thought to be the general model structure for representing the metallic foam but it was found to be the otherwise (Raj, 2011).

The present research uses an open type of metallic foam, *i.e.*, a copper porous metal, which was purchased from a manufacturer in China. The preparation of samples involves cutting five number of specimens with a size of 40mm × 40mm × 5mm from the main piece. The inspection on the specimens involves measuring the dimensions and weight. For the latter, a weighing machine with the model name of GH-202 series by A&D Company (Japan) was used. It has readability of 0.01 mg. In the measurements, the average (μ_s) and the standard deviation (σ_s) were 3.15197g and ± 0.02665g, respectively. The relative standard of deviation (σ_s/μ_s), calculated as 0.02665g /3.15197g, is approximately lesser than 1%.

The CFD model uses one of the specimens with the least defects or variations (see Figure 5.1a). It has an average solid mass ($\bar{m}_s$) of 3.1601g. That specimen has an average porosity of 96% which was calculated using the equation, $\bar{\phi} = 1 - \bar{m}_s/\rho_s V_T = 1 - V_s/V_T$ where V_T is the volume of the outer geometry (40 mm x 40 mm x 5 mm) and the copper density (ρ_s) is 8940 kg/m^3. The PPI was counted to be 36 units. The 3D scanning of the actual specimens used a micro Computed Tomography (CT) imaging machine, namely Seiss Xradia 510 Versa, located at Department of Geology, University Malaya. It is capable of scanning with a spatial resolution of 0.7 µm with a minimum voxel of 70 nm. First, the file conversion steps involves the imaging software, AVIZO (Version 6.3) which translates the 3D geometry data of Tagsoft data (TXM) format into the Digital

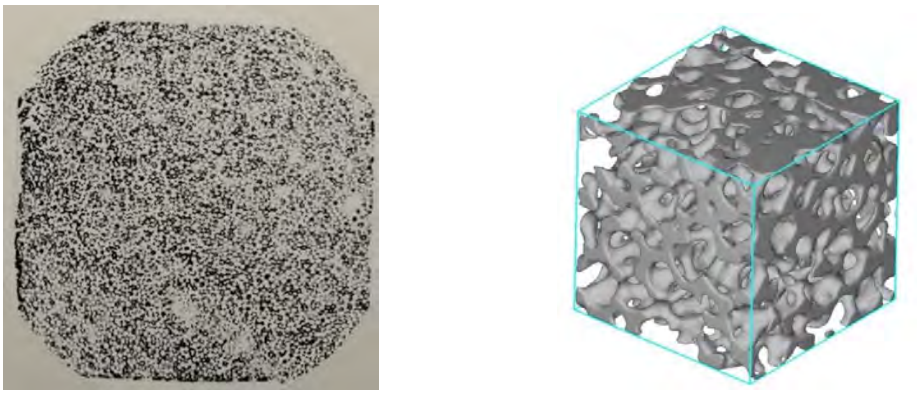

(a) (b)

Figure 5.1: (a) 40mm × 40mm × 5mm porous metal. (b) 3mm × 3mm × 3mm porous metal. Both images were obtained from CT Scan.

Imaging Communications in Medicine (DICOM) format. Another imaging software, InVesalius (Version 3.1), is used to convert DICOM into Stereolithography (STL) format.

The effect of the interior shapes in the present behavioural study would be more noticeable for a smaller specimen rather the larger one. Also, the dimensions of the smaller specimen is closer to a louver fin size used in radiator (2 to 3mm). For those reasons, the CFD model used the smaller specimen instead of the larger one. The porous metal geometry (3mm × 3mm × 3mm) has a surface area (A_s) and a solid volume (V_s) of 148 mm^2 and 9.99 mm^3 respectively. As a consequence of reducing the sample size, the porosity and PPI changes. The new porosity is 63% which calculated as $1 - (9.99/27)$. The average PPI for that sample is 47 units.

The purpose of creating the ideal geometry is to compare the water retention behaviour in both the geometries. The ideal geometry consists of two kind of unit cells, *i.e.*, the full unit cell (see Figure 5.2a) and the partial unit cell (see Figure 5.2b). In Figure 5.2c, the full unit cells are located at the core and surrounded by the partial unit cells, also known as the outer units. The ideal geometry has outer dimensions (V_T) of 3mm × 3mm × 3mm, 63% in porosity and 47 PPI. The A_s and V_s of the ideal geometry are 140 mm^2 and 9.97 mm^3 respectively. The geometry specifications, *i.e.*, PPI, θ, A_s, V_s, are close to the porous metal geometry as the above. For achieving the same V_s as the porous metal geometry, the ratio unit length ($\bar{l}$) to pore diameter ($\bar{d}$) of Equation (5.1) was adjusted iteratively. The present model uses 2.61units for the ratio of $\bar{l}$ to $\bar{d}$.

The terms used in volume formula (see Figure 5.2) is the radius of the unit sphere (r_i), the diameter of the pores (d_i) and the length of a unit cell (l_i). The volume of a unit cell is equal to the total of a cube volume minus the volume of a sphere without its minor caps. The total solid volume is formed as $V_s = \sum_1^{N^3} v_i = N^3 \bar{v}$. In the formulations, the average terms like $\bar{r}$, $\bar{d}$, and $\bar{l}$ are used to replace the terms of the unit cell accordingly.

The length of the cube (L) is given as, $L = \sum_1^N l_i = N\bar{l}$ wherein by the $\bar{l}$ is the unit length and the N is the number of pores. The total solid volume of the ideal geometry is

$$V_s = \left(\frac{L}{\bar{l}}\right)^3 \left[\frac{\pi}{3}\left(\bar{l}^2 + \bar{d}^2\right)^{1.5} - \frac{3}{4}\pi\bar{l}\left(\bar{l}^2 + \bar{d}^2\right) + \left(\frac{\pi}{4} + 1\right)\bar{l}^3\right] \quad (5.1)$$

where $\bar{v}$ is the volume of the unit cell. See Appendix A for proofs.

In finding the total surface area, it is the sum area of the inside units ($A_{i,in}$), the outer units ($A_{i,out}$) and the cut or sectioned faces ($A_{i,cs}$). The parameter of $A_{i,in}$ is the area of a sphere without six of its minor caps. The parameter of $A_{i,out}$ is the sum of $0.5A_{i,in}$ and an extra area which starts from the centreline to the cut line (see Figure 5.2b). The extra area is formed as $\int_{\alpha_2}^{\frac{\pi}{2}} \int_{\theta_1}^{\frac{\pi}{4}} 8 \cdot r_i d\theta \cdot sin\alpha \cdot r_i d\alpha$. The angle α is the angle rests on the plane as per view. The angle θ is the angle rests on a plane which parallels to the cutting

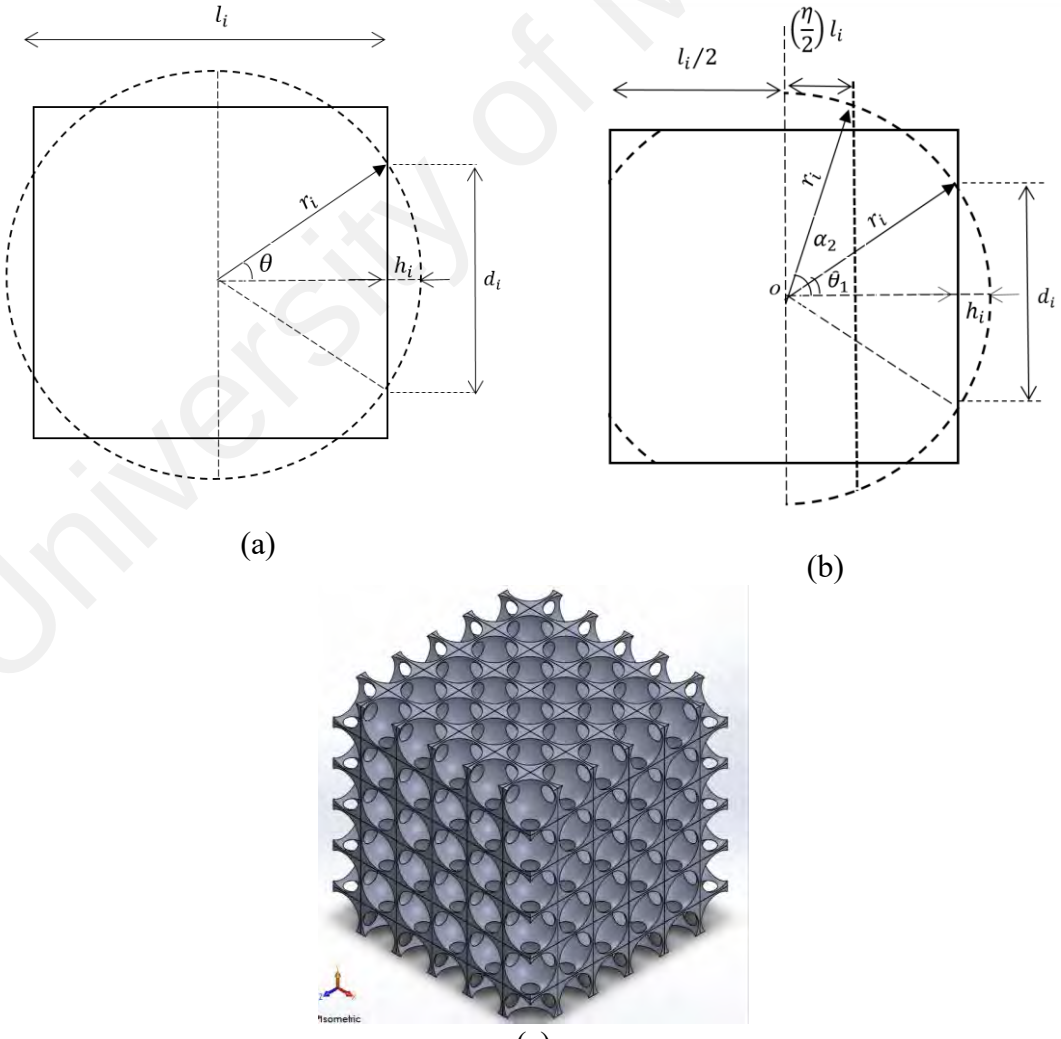

(a) (b)

(c)

Figure 5.2: (a) A full unit cell. (b) A unit cell with cut-line. (c) The ideal geometry.

plane. Both angles are stated in the same diagram for the ease of presentation. The parameter of $A_{i,cs}$ is the remaining area of the subtracted square at which it was sectionalized. The total surface area of the ideal geometry is the sum area of the inside units ($A_{i,in}$), the outer units ($A_{i,out}$) and the cut or sectioned faces ($A_{i,cs}$) and given by

$$A_s = k_1 A_{i,cs} + k_2 A_{i,out} + k_3 A_{i,in} \tag{5.2}$$

where the unit counts are $k_1 = 4$, $k_2 = 6(N-\eta)^2$ and $k_3 = (N-1-\eta)^3$ and follows

$$A_{i,in} = -2\pi\bar{l}^2 - 2\pi\bar{d}^2 + 6\pi\bar{l}\bar{r} \tag{5.3}$$

$$A_{i,out} = \frac{1}{2}A_{i,in} + 4\eta\bar{l}\bar{r}\left(\frac{\pi}{4} - \sin^{-1}\left(\frac{\bar{d}}{2\bar{r}}\right)\right) \tag{5.4}$$

$$A_{i,cs} = \bar{l}^2 + \left(4\tan^{-1}\left(\frac{2b}{\bar{l}}\right) - \pi\bar{r}^2\right)\left(\bar{r}^2 - \left(\frac{\eta\bar{l}}{2}\right)^2\right) - 2b\bar{l} \tag{5.5}$$

The average radius, $\bar{r} = \sqrt{(\bar{l}/2)^2 + (\bar{d}/2)^2}$ and the unknown $b = \sqrt{(\bar{d}/2)^2 - (\eta\bar{l}/2)^2}$ for the condition that $\bar{d} > \eta\bar{l}$ or else $b = 0$ if otherwise. See Appendix B for proofs.

5.3.2 Simulation Cases

The purpose of dimensional analysis is to identify the common parameters used for the simulation cases. For the dimensional analysis, the geometric variables like $\bar{d}, \bar{l},$ and N (see Section 5.3.1.2) are replacing the parameters like ϕ and PPI. The analysis begins with the variables in a function are given as $f(\mu, \rho, \sigma, \theta_s, U, g, \gamma, \bar{d}, \bar{l}, N) = 0$ where μ is dynamics viscosity, g is gravity acceleration, and γ is an angle of orientation. The dimensionless groups are given by

$$f\left(\frac{U}{\sqrt{\bar{d}g}}, \frac{\rho U\bar{d}}{\mu}, \frac{\mu.U}{\sigma}, \frac{\bar{l}}{\bar{d}}, N, \theta_s\right) = 0 \tag{5.6}$$

Since the variables γ, $\bar{d}$ and N are not varied in the study, the final form of the dimensional analysis becomes

$$f(Ca, \theta_s) = 0 \tag{5.7}$$

where *Ca* is Capillary number (see Appendix C for proofs). In each of the simulation cases, the geometry has a specific θ_s and a specific *U*. The specific θ_s of the cases are

30°, 60°, 75°, 90° and 120°. In every simulation case of θ_s, the study varied the *U* for 0.5, 2, 4, 6 and 8 mms^{-1}. For a note, Hu et al. (2017) used *U* of $4mms^{-1}$. The corresponding *Ca* number, in the order of 10^{-6}, are 6.86, 27.45, 54.90, 82.35 and 109.80 respectively.

5.3.3 Governing Equations and Numerical Scheme

The present research uses the Volume-of-Fluid (VOF) method of the commercial CFD software, namely FLOW-3D®. It defines the simulation model as a three-dimensional (3D) with the isothermal condition. It uses incompressible flow settings and Newtonian single-phase fluid. The mass continuity equation is

$$\frac{1}{V_F}\frac{\partial}{\partial x}(\rho u A_x) + \frac{1}{V_F}\frac{\partial}{\partial y}(\rho v A_y) + \frac{1}{V_F}\frac{\partial}{\partial z}(\rho w A_z) = -\frac{R}{V_F} \tag{5.8}$$

where V_F is fractional volume open to flow and (A_x, A_y, A_z) are the fractional open to the flow. The variables (u, v, w) are the fluid velocity components. The *R* is the mass source term. The negative *R* represents the rate of fluid mass moving out of the computational domain. It uses the fractional face areas and the fractional volumes of the cells that are open to the flow for defining the wall boundary features in the mesh. The software solves the equations of Navier-stokes (see Equation (2.2)) where the conditions were isothermal, incompressible, single fluid with gravitation force. The free surface in Eulerian grids is solved by Equation (2.3) using the mathematical conditions of Equation (2.4). At the free surface interface, the atmospheric pressure treatment is given by Equation (2.5). The advection of the free surface in the grids was explained in Section 2.2.5. The residual value of 10^{-4} for the momentum and continuity equations is set as the convergence criteria.

5.3.4 Initial and Boundary Conditions

The geometry in fixed position that was defined with no-slip wall boundary conditions for the cases with hydrophilic conditions *i.e.*, θ_s of $30°, 60°, 75°$ and $90°$. It also used free-slip wall boundary conditions for hydrophobic surface *i.e.*, θ_s of $120°$.

The preferences follow a set of established criteria in Chapter 3. The flow drain-off with a specific outflow velocity at the lowermost boundary of the computational domain. Two of the geometry sides are the symmetrical boundary conditions, which are also the boundaries of the computational domains. As such, the geometry occupies the corner of the computational domain. The other boundaries are open pressure boundaries. The size of the computational domain is 120mm width, 120mm length, and 120mm in height with a mesh aspect ratio of unity. The computational domain consists of several levels of mesh refinements. The pressure and velocity calculations at inter-mesh levels use the Neumann and Dirichlet boundary conditions as the controls. On top of geometry, it has additional water height of 0.3mm. The drainage direction was parallel to the z-axis direction. g is 9.81m/s^2. The ρ and the σ were 998.21kg/m^3 and 0.0728 N/m, respectively.

5.3.5 Mesh Independency Test

Mesh independency tests check the sensitivity of mesh on the simulation results. The cases of M1, M2, and M3 (see Table 5.1) have unit mesh size of 0.06mm, 0.12mm, and 0.24mm, respectively. The mesh independency test uses porous metal geometry with θ_s of 90° and the U of 4mm/s. The solution time for solving the M2 case was approximately two weeks using a computer with Intel Xeon EU31225 (3.1GHz) processor. The mesh independency test evaluates the volume of water remaining on the porous metal. The mesh size of the M2 case is reasonable for the use in the present research due to its solution time and the volume of water remaining on the porous metal did not differ much from the M1 case.

Table 5.1: Cases of mesh independency test

Geometry Type	*Cases*	*mesh size (mm)*	ϕ	*time steps (s)*	*Volume retention (mm^3)*
Porous metal	M1	0.06	61.05%	1.36×10^{-6}	0.0765
	M2	0.12	63.00%	4.29×10^{-6}	0.0799
	M3	0.24	70.14%	1.14×10^{-5}	0.0952

5.3.6 Structural Homogeneity

5.3.6.1 Definitions

The common solid element in metallic foam, namely "strut", connects between two junctions. The junction position is treated as a unique entity for simplicity. Other entities like the junction position, the strut length, and the angle between struts are linked or chained. Thus, the interpretation of homogeneity is interchangeable among those entities. Also, another type of variation in the porous metal geometry that can be measured is the number of connecting struts at a junction. For combining the variations, the overall structural homogeneity ($\overline{D}_s$) is expressed by

$$\overline{D}_s = \left(\prod_{p=1}^{p} D_p \right)^{\frac{1}{p}} \tag{5.9}$$

where D_p, is a independent factor. It is denoted with an arbitrary unknown 'p'. See equation (5.11). The capital-pi symbol represents the product operator for every independent factor. The p^{th} root is to average the products. In the present research, the specific independent factors are D_x, D_y, and D_z. of which it is the junction position in *x, y*, and *z* coordinates accordingly while the independent factor of the number of connecting struts per junction is denoted by D_q. Thus, the overall structural homogeneity is

$$\overline{D}_s = \sqrt[4]{D_x D_y D_z D_q} \tag{5.10}$$

For the independent factor, it uses the general form that is

$$D_p = (1 - C) + \frac{C + \sigma_p}{C + |\mu_p|} \tag{5.11}$$

where $\mu_p$is the average and σ_p is the standard deviation of that particular factor. While *C* is an arbitrary factor that changes the general form into two types of equations using the option *C* equals to unity or zero. Both of these forms are the modification of the relative standard deviation. Casually, it is the ratio of the standard deviation to the mean, σ_s/μ_s (Everitt, 1998). It is a standardised measure of variation of a frequency distribution.

The modification is necessary for resolving the issue in evaluating the relative standard deviation when $\mu_p \approx 0$, which results in a vast number for D_p which consists of zero in the number system (or the real number, $\mathbb{R}$), *e.g.*, the independent factors D_x, D_y, and D_z, must use Equation (5.11) with C equals one. The average junction positions (μ_x, μ_y, μ_z) or the average centre is the summation of all of the positive and negative coordinates of the same axis or variable. It often results in a value that is close to zero. On the other hand, the independent factor D_q uses Equation (5.11) with C equals zero. It changes Equation (5.11) into the original form of relative standard deviation, which is suitable for the non-zero group of number (or the counting number, $\mathbb{N}_1$).

5.3.6.2 Locating the junction positions in porous metal

For applying the definitions above, the method requires one to 'track' the junction position within one interval and to another interval. It uses a 3D-modelling software, namely SOLIDWORKS (version 2019), for that purpose. As shown in Figure 5.3a, the circles trace or 'tracks' the strut diameters and the lines connect the circles on the same solid boundary on a specific plane or cross-section. The present research creates 10 units or 2(N-η) of space intervals in parallel for 'tracking' the junction locations. As shown in Figure 5.3b, the thicker 3D lines 'track' the centre of a circle to another one in the neighbouring space intervals. The condition for the 'tracking' is that the pair must consist of a strut in its path. In that method, a junction is defined as a point with at least three units of connecting lines (struts). In Figure 5.3c, it shows the final representation of all the lines in the porous metal geometry.

Then, the final representation in 3D wireframe lines was exported as the Initial Graphics Exchange Specification (IGES) before converting it into text format. The x, y and z coordinates from the text data using Microsoft Excel. In learning to identify the data, the learning begun by using simple entities such as a point, a line, circle, and others. In

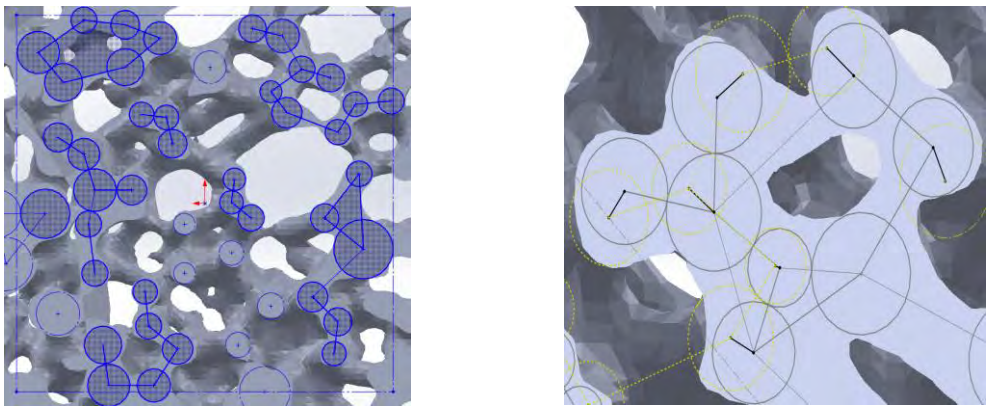

(a) (b)

(c)

Figure 5.3: (a) 'Tracking' the junction position. (b) 'Tracking' two parallel cross-sections with the thicker lines. (c) All of the connected lines

Appendix D, the table shows the data arrangement where a particular junction position (x_m, y_m, z_m) is next to the quantity q_m for a common point which denoted as, E_m. The averages (μ_x, μ_y, μ_z) are the sum of the positive and the negative coordinates within the columns. The same calculation followed by the 'average number of struts connecting to a junction' (μ_q), the standard deviations $(\sigma_x, \sigma_y, \sigma_z, \sigma_q)$ and the independent factors (D_x, D_y, D_z, D_q).

5.4 Results and Discussion

5.4.1 The measured structural homogeneity

Table 5.2 shows the average values and the overall structural homogeneity factor in both of the geometries. The overall structural homogeneity ($\overline{D}_s$) of the ideal geometry and the porous metal geometry are 1.01 and 1.61 units, respectively. Theoretically, an infinite length of an ideal geometry has no variation. Its overall structural homogeneity

Table 5.2: Details of overall structural homogeneity calculation

	Porous Metal Geometry	*Ideal Geometry*
$\mu_x \pm \sigma_x$	-0.0374±0.853	0
$\mu_y \pm \sigma_y$	-0.0770±0.896	0
$\mu_z \pm \sigma_z$	-0.0679±0.804	0
$\mu_q \pm \sigma_q$	3.841±0.998	5.397±0.271
D_x	1.786	1
D_y	1.761	1
D_z	1.690	1
D_q	1.260	1.050
$\overline{D}_s$	1.61	1.01

factor always unity ($\overline{D}_s$ of 1). However, some variations exist in the present geometry due to the segmentation. At the edge, it consists of partial unit cells. The junction at the full unit cell has six units of connecting struts while the junction at the sectioned face has five units of connecting struts. Thus, the parameter $\overline{D}_s$ is not equal to unity for the ideal geometry. In the porous metal geometry, the independent factors (D_x, D_y, D_z) are much higher than the parameter of D_q. It means that the variation in the structure are more affected by (D_x, D_y, D_z) rather than D_q.

Figure 5.4a shows the distribution of local $\overline{D}_s$ by the space intervals. The calculation for the local $\overline{D}_s$ for a particular axis direction uses Equation (5.10) with a replacement value. At a particular direction, the replacement value for the independent factor in that direction is one (see the legend in Figure 5.4a). *E.g.*, the local $\overline{D}_s$ of the *z*-axis direction use D_z equals unity wherein the Equation (5.10) becomes $\left(D_x \cdot D_y \cdot 1 \cdot D_q\right)^{1/4}$. The replacement or correction value is necessary. In some cases, the D_p falls below unity. As observed, Equation (5.11) does not restrict the parameter D_p to have a value below one when $\sigma_p \approx 0$ and $\mu_p > \sigma_p$. Since the measurement gathers the data by intervals, the σ_p for space intervals of the same sampling axis-direction would have the least variation in position ($\sigma_p \approx 0$). Thus, the correction is justifiable because the sampling is done by interval basis. In Figure 5.4a, the coordinates of -1.5 mm and +1.5mm are the end faces. For the porous metal, the local $\overline{D}_s$ at the end faces are lower than the

other intervals. The local $\overline{D}_s$ was ranging from 1.20 to 1.45 approximately. Meanwhile, the local $\overline{D}_s$ for the *x* and *z* directions at the center of porous metal geometry are relatively lesser than the neighbouring ones. On the other hand, the ideal geometry is represented by one solid line since the variations are the same for all of the axis-directions.

Figure 5.4b shows the frequency distribution for the number of connecting struts per junction in the porous metal geometry. The classes for 'q' in the population are ranging from three to eight units. The frequency of 'q' equals three units of connecting struts, is denoted as n (q=3). It amounted 46.5% of the total population. It followed by 32.5% 13.2%, 6.1%, 1.1%, and 0.5% for 'q=4', 'q=5' and up to 'q=8' respectively. A probability function was developed using those percentages. As a note, the probability function can be a useful reference for recreating an identical porous metal geometry. The estimated probability function based on counting basis is given by

$$P(q) = \left(\frac{e}{\pi}\right)^3 \sum_{n=0}^{n=2} (-q)^n f_1 f_2 f_3(n) \tag{5.12}$$

with R^2 = 0.9785 wherein the function $f_1(n) = 2^n$, $f_2(n) = 3 - 2^n$ and $f_3(n) = n + 1$ maps into one and another accordingly. In the estimation, the probability of a junction to have eight numbers of connecting struts per junction, P (q=8) is equal to zero. For P (q=3),

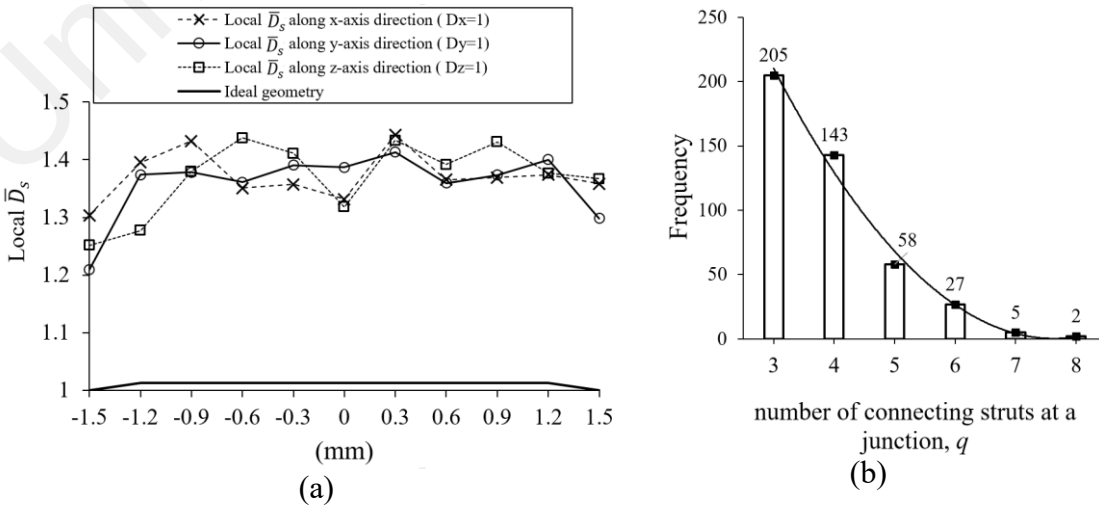

Figure 5.4: (a) The local $\overline{D}_s$ for different axis directions. (b) Frequency distribution vs the total number of connecting struts per junction.

it is equal to 0.5061 or 50.61%. The Equation (5.12), is obtained by performing factorisation using the common factor, *i.e.,* coefficient $(e/\pi)^3$ on a polynomial equation which estimates the same population. The factorisation calculation was done using Microsoft Excel. The coefficient $(e/\pi)^3$ was chosen from a list of e and π products with different indexes. The remaining coefficients were rounded up as whole numbers. The condition for the selection was that the remaining coefficients in the polynomial equation must be a lead for a complete factorisation for summation or formulation. Then, a new R^2 was recalculated for the new estimation (See Appendix E for proofs).

5.4.2 Number of Junctions by Space Intervals

Figure 5.5 shows the number of junctions by the space interval for both of the geometries. For the ideal geometry, there are 45 units of junctions per interval for the in-between ones while 25 units of junctions per interval for the end faces. On the other hand, the average number of junctions per interval recorded for porous metal geometry were 40±10.5, 40±9.4 and 40±12.2 units for the *x*, *y* and *z*-axis directions respectively. The number of junctions in the space intervals between coordinate-*y* ranging from +0.45mm to +0.75mm is 27 units. It is far lesser than the other space intervals. It indicates that the

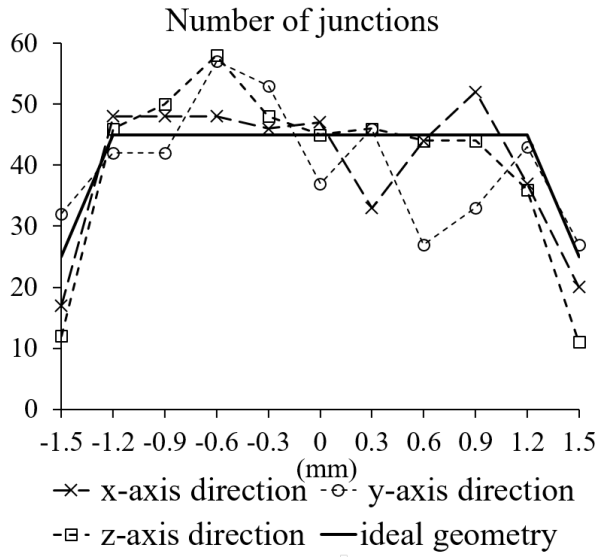

Figure 5.5: The number of junctions for different axis directions.

pores size is larger than its neighbouring space intervals. Also, the local $\overline{D}_s$ of that location is lower than its neighbouring space intervals (see Figure 5.5). It indicates that the large pores are distributed more evenly than its neighbouring one. In the same way, small pores with more uniform distribution can be observed at the space intervals from the coordinate-*y* ranging from - 0.45mm to - 0.75mm. It consists of 58 units of junctions and a lower local $\overline{D}_s$ as compare to its neighbouring ones.

5.4.3 Result by Entire Geometry

5.4.3.1 Observable Behaviours

Figure 5.6 shows the time series results for both of the geometries. *U* is 0.5mm/s, and θ_s is 60°. At *t* of 4s, the geometries were set in a fixed position and seen as if emerging from the water surface as the water level decreases. At *t* of 8 sec, the water surface can

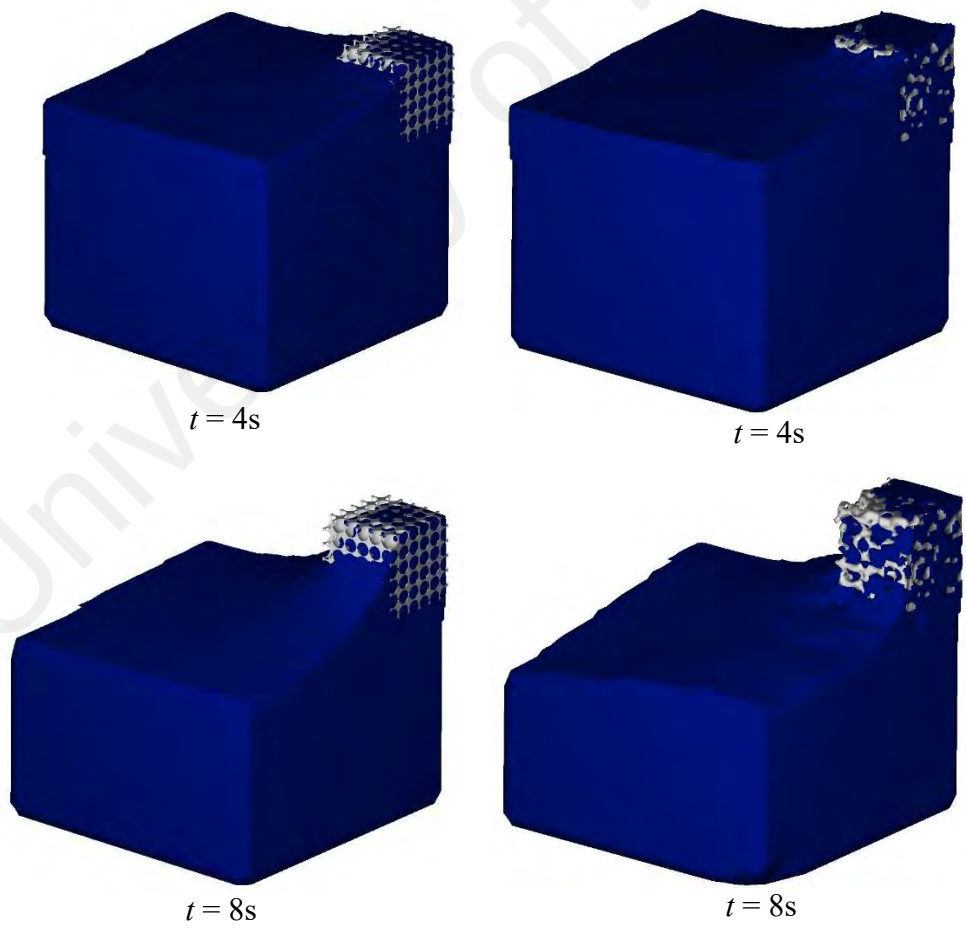

Figure 5.6: Comparison of water retention in the ideal geometry (left side) and porous metal geometry (right side).

be seen pulling on the solid surfaces. The water lines formed gradients on the side of the geometries. The contact line of the water free-surface on the ideal geometry was more uniformed as compared to the porous metal geometry.

Figure 5.7a and Figure 5.7b showed the final conditions of water retention (t_∞). The shape of water retained inside the ideal geometry is rather more spherical as compared to the one in porous metal geometry. In Figure 5.7b, the pores on the right side of the porous metal geometry retained less water compared to its left side. For evaluation purpose, the saturation of water in the porous medium is given by

$$V_r^* = \frac{V_r}{V_T - V_s} \tag{5.13}$$

where V_r is the retained volume and the expression $(V_T - V_s)$ is the volume of void in a geometry. The average saturation of water (V_r^*) for the ideal geometry and the porous metal geometry were 1.05 and 0.76 respectively. The ideal geometry retained slightly more fluid *i.e.*, around 5% than the total void volume (space) inside due to the extra water on the top and sides surfaces.The distribution of V_r^* in the geometries were investigated using the space intervals.

Figure 5.7c shows that the saturation in the ideal geometry is more than the porous metal geometry. The direction of the space intervals in Figure 5.7c is the same one as shown in Figure 5.7a and Figure 5.7b, *i.e.*, from the left to the right. The occurrence of spikes in the graph is due to the uniformity of the solid junctions which are aligned together. In those intervals, it consists more surface area where it is easier for water to 'stick' or hold on the surfaces. On the other hand, the retained water volume was declining from coordinate-*y* equal to -1.5mm to +1.5mm in the porous metal geometry (See Figure 5.7c). The reason for the steady declination is due to the structure non-uniformity across the intervals (See Figure 5.7d).

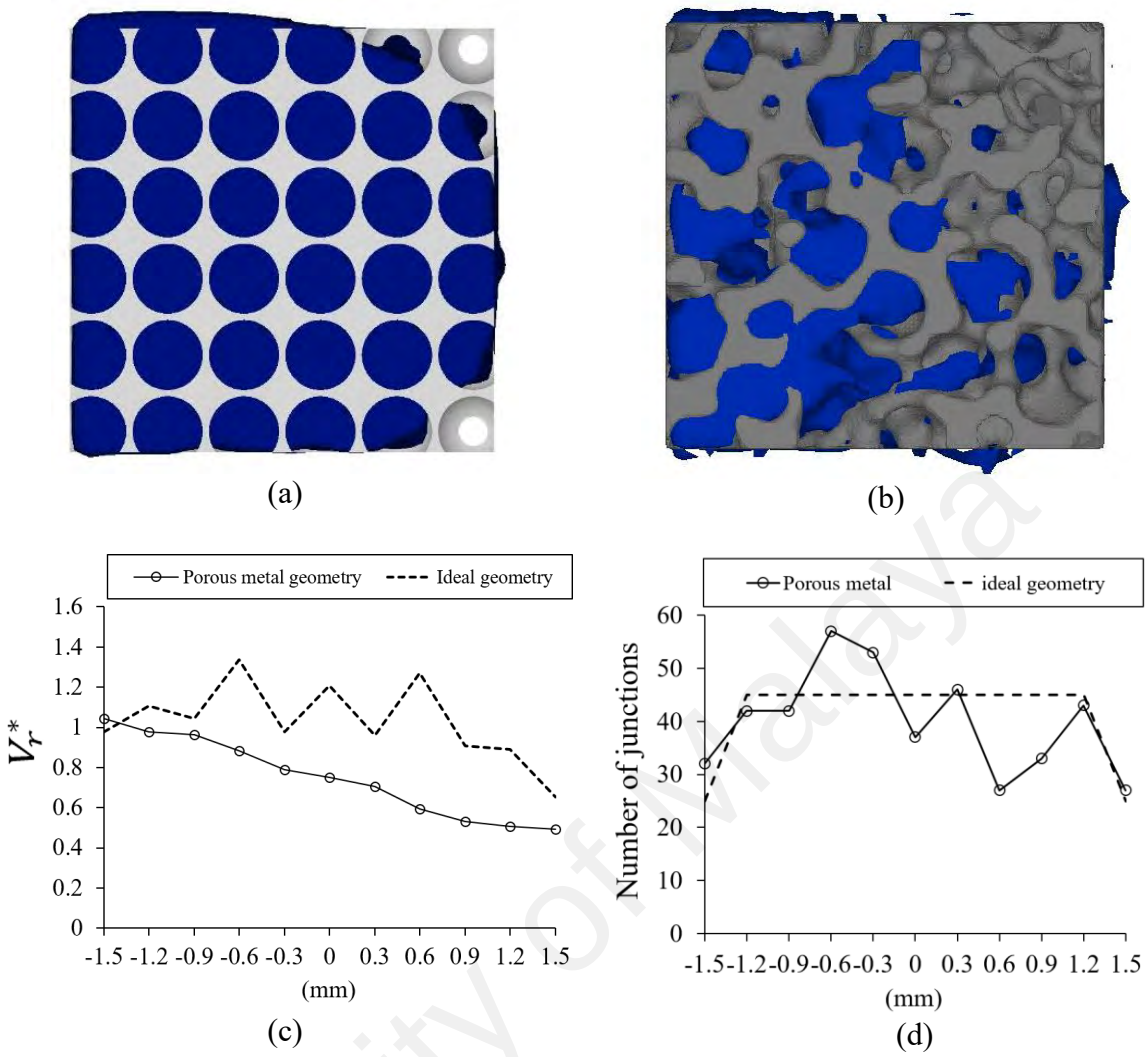

Figure 5.7: Results at t_∞ of 16.8s for (a) the ideal geometry and (b) the porous metal geometry. The shape of water in ideal geometry is rather more spherical than the one in porous metal geometry. The *y*-axis direction is parallel to horizontal direction while the *z*-axis direction is parallel vertical direction. The intervals data in *y*-axis are presented by the figures of (c) water saturation vs. space intervals and (d) number of junctions vs. space intervals.

5.4.3.2 The Effect of Different θ_s and U

Figure 5.8 shows that both of the geometries with a lower θ_s (lower hydrophobicity) retains more water than the one of a higher θ_s. For cases with the ideal geometry recorded V_r^* of 1.05, 0.70, 0.53, and 0.05 units for different θ_s, *i.e.*, 60°, 75°, 90°, and 120° respectively. The water saturation changes very slightly with different U in ideal geometry and it is almost independent of that parameter. The uniformity of the struts in the ideal geometry has enable it to retain a higher volume of water with minimal influence from U. At U of 0.5mm/s, the porous metal geometry retains V_r^* of 0.76, 0.37,

0.04 and 0.04 units for cases with θ_s of 60°, 75, 90 and 120° respectively. Furthermore, the cases *i.e.*, θ_s of 60° and 75° are showing that the water saturation (V_r^*) decreases with the increasing *U*. As for cases with $\theta_s$of 120°, it varies randomly.

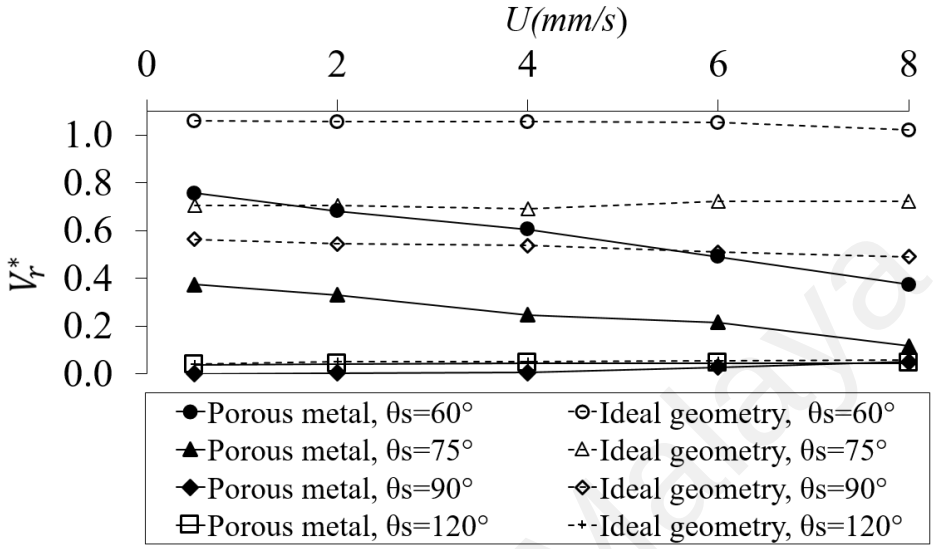

Figure 5.8: The water saturation vs drainage velocities. Comparisons of both the geometries with different hydrophobicity.

5.4.4 Results in Space Intervals

5.4.4.1 Comparison of V_r^* at the Same θ_s

Figure 5.9 shows the V_r^* distribution in both geometries with different hydrophobicity for the *x, y* and *z* axis directions. The θ_s of those cases are 60°, 75°, 90°, and 120°. The symmetry boundaries are located at -1.5mm for *x* and *y* axis directions. In Figure 5.9a, the ideal geometry has a higher water saturation at the spikes generally. The V_r^* distribution at the symmetry boundary is higher than the opposite ends which are open to the reservoir at coordinate- *x* and *y* of 1.5mm. In the *x* axis direction of the porous metal geometry (Figure 5.9b), local V_r^* on the right side (from 0mm to +1.5mm) is higher than its left side (from -1.5mm to 0mm). The water retains more on the right side is because of (i) the number of junctions per interval on the right side is slightly higher than its neighbouring space intervals, that it means that the pores size are small; and (ii) it has a lower local $\overline{D}_s$ as compare to the left side, that means the pores are more uniform than the other. The V_r^* distribution in the *y*-axis direction was the opposite of the *x*-axis direction.

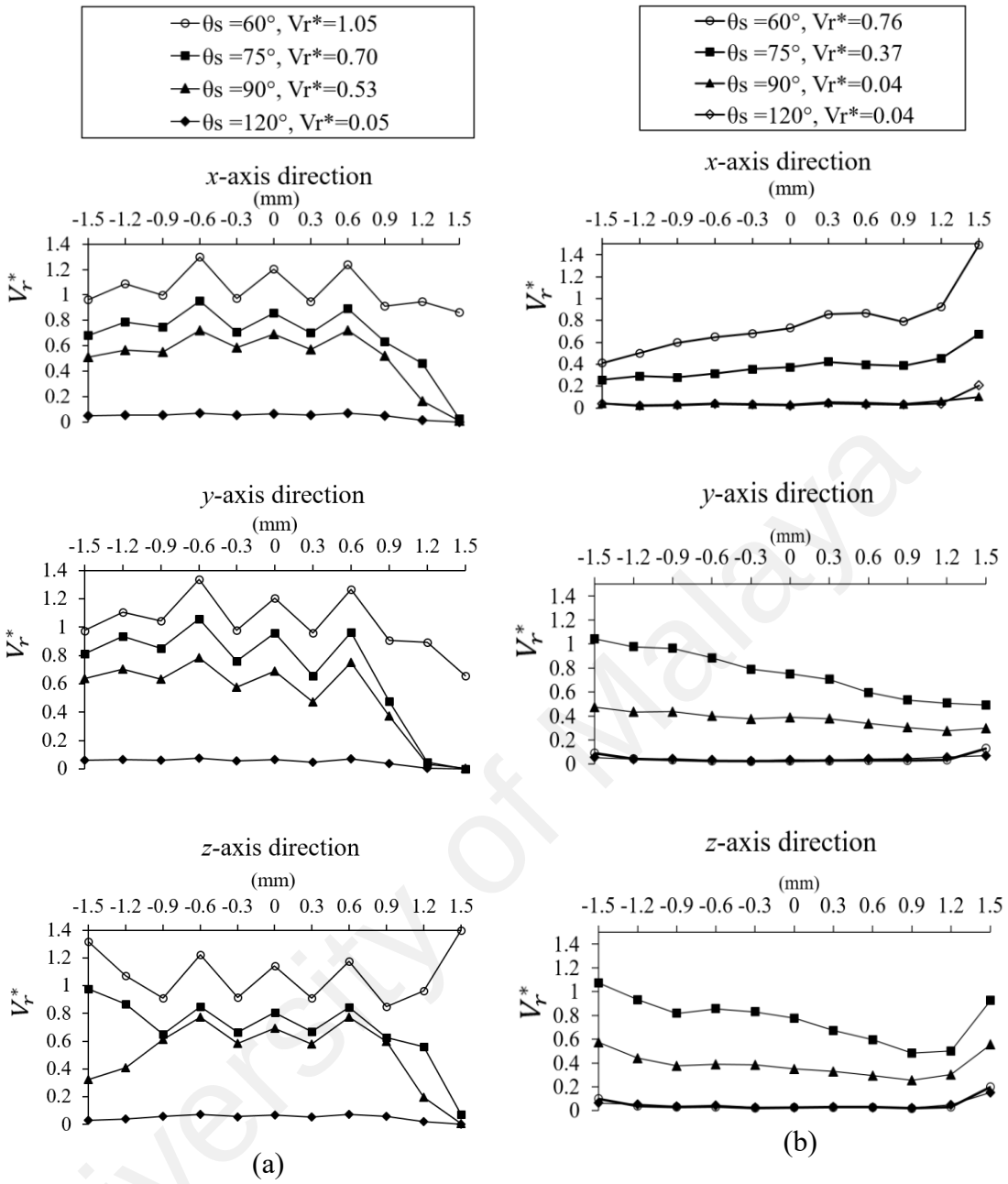

Figure 5.9: The saturation of water by the space intervals in the *x, y* and *z*-axis directions. The comparisons of the same θ_s for (a) the ideal geometry and (b) the porous metal geometry. The *U* of the porous metal geometry maintained at 0.5mm/s.

The local V_r^* of both geometries at the space interval at coordinate-*z* of -1.5mm are higher than the top space intervals generally. It is due to the gravity direction and the higher number of junctions in the lower region. In addition, the number of junctions for the space intervals in the lower region, ranging from -1.5mm to 0mm in *z*-axis, is higher than the space intervals in the upper region, ranging from 0 to 1.5mm in *z*-axis (See Figure 5.5). At the space intervals ranging between coordinate-*z* of +0.9mm to +1.2mm in Figure

5.9b, the "bend" shape in V_r^* distribution indicates a sudden change in the pore sizes. The local $\overline{D}_s$ of that location is much higher than its neighbouring space intervals (Figure 5.4a).

However, the number of junctions of those space intervals was normal as compared to its neighbouring space intervals (Figure 5.6). It means that the location consisted of the large pores which were concentrated in one quadrant of the geometry. With that estimation, the large pores are located at the coordinate-*x* of +0.3mm, *y* of +0.6mm and z of +0.9mm. By visual, it can be seen in the unfilled region at the top of Figure 5.7b. It shows that the graph of the in-plane $D_x D_y$ is similar to the local $\overline{D}_s$. Also, the in-plane $D_x D_y$ is higher than D_q. For confirmation, the present research investigates the dominance of the local $\overline{D}_s$ for that *z*-axis direction.

In Figure 5.10, the independent factors were compared, *i.e.*, the in-plane homogeneity $D_x D_y$ and the parameter of D_q. It means that the structural homogeneity in junction positions is more dominance than the variation in the number of junctions. The calculation uses a replacement value for Equation (5.16). The in-plane $D_x\, D_y$ is calculated as $\left(D_x \cdot D_y \cdot 1 \cdot 1\right)^{1/4}$ where D_z and D_q are replaced by one. For the parameter of D_q, it is calculated as $\left(1 \cdot 1 \cdot 1 \cdot D_q\right)^{1/4}$ where D_x , D_y and· D_z are replaced by one.

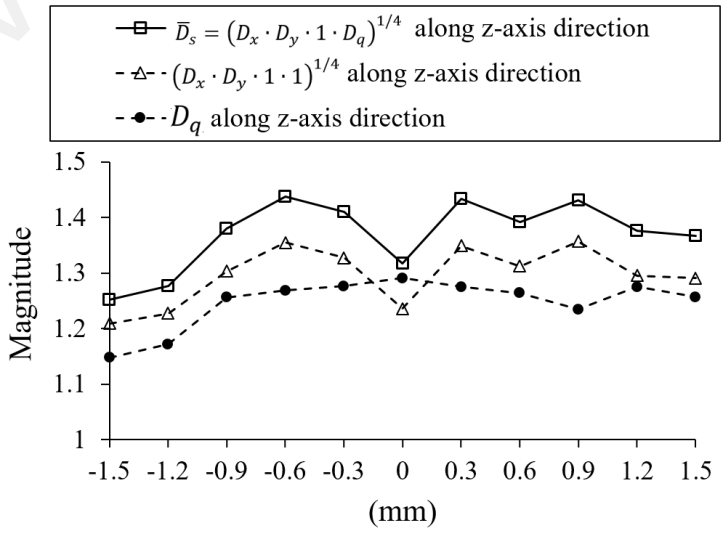

Figure 5.10: Local $\overline{D}_s$ and its independent factors in the *z*-axis direction.

5.4.4.2 Comparison of V_r^* at the same U

As shown in Figure 5.11, the V_r^* distribution in porous metal geometry with different hydrophobicity under the influence of different U. The related cases use θ_s of 60° and θ_s of 75°. The order of the U of cases with θ_s of 60° was overlapping or sharing the same common saturation at several locations. Such phenomenon happened at coordinates-x ranging from -1.5mm to -1.2mm; coordinate-y of 0.9mm; and

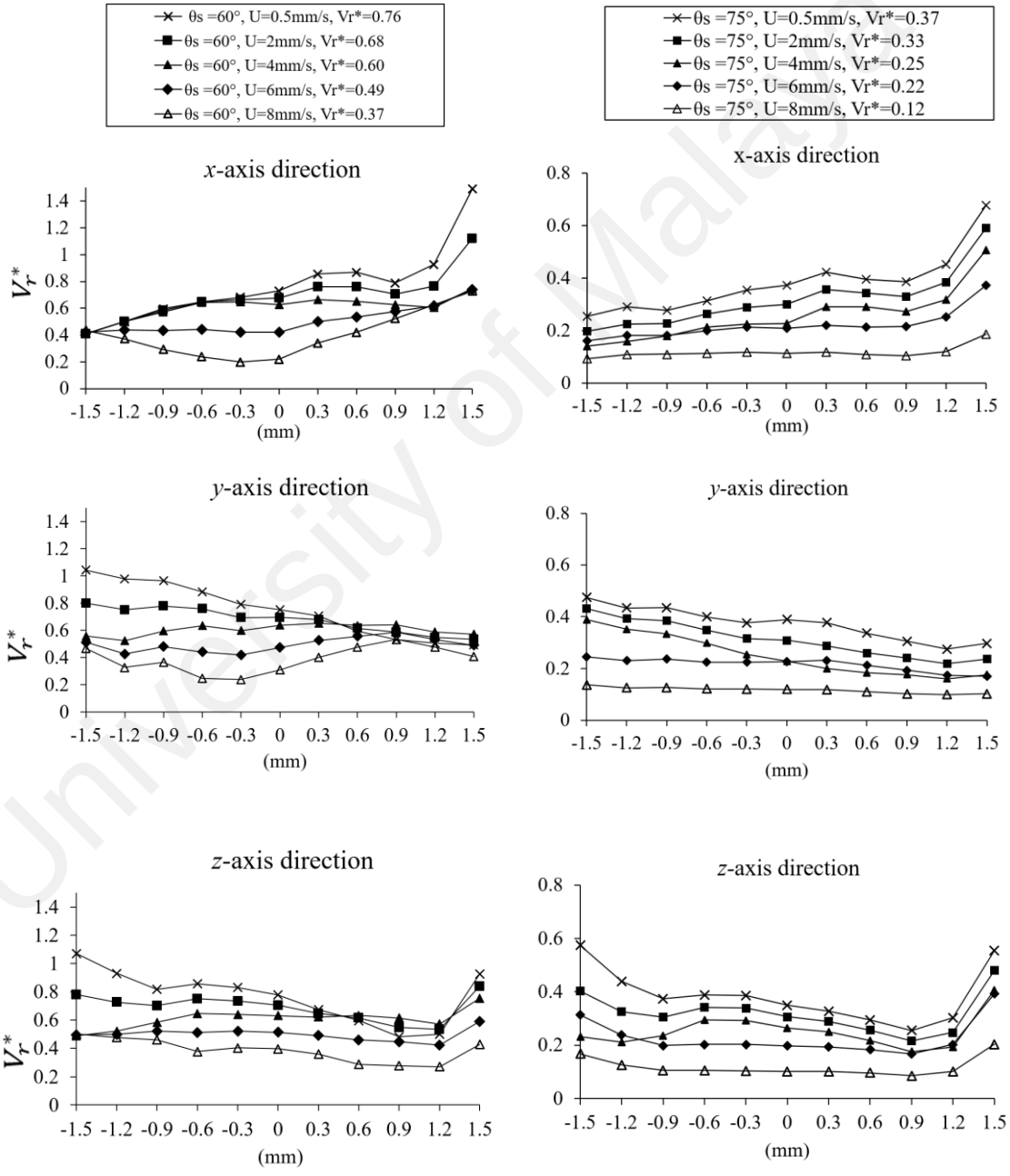

Figure 5.11: The saturation of water by the space intervals in the *x, y* and *z*-axis for the porous metal geometry with (a) θ_s of 60° and (b) θ_s of 75° at different U.

coordinates-z at -1.5mm, 0.6mm and 1.2mm. Most of those coordinates consist of large pores. The V_r^* distribution cases with θ_s of 75° seems to be more independent or less dependent on the geometric variations. Simply, it means that a higher hydrophobicity enables the water to move around the structures with lesser resistance. Table 5.3 shows that the behaviours of water retention in different porous-like structures. It includes the literature findings regarding the behaviour of water retention in heat exchangers. In the present research, both of the porous structures, *i.e.*, the porous metal geometry and the ideal geometry, retain a lesser volume of water at higher hydrophobicity. The same behaviour was observed by Hu et al. (2017) in dynamic dip-testing for metal foam. Liu and Jacobi (2008) reported the same kind of observation when testing a heat exchanger of the plain-fins with round-tubes type with a hydrophobic coating. In that findings, it was reported that the behaviour of water on straight surfaces in the columns that did not break quickly. Thus, it retains less water on the hydrophobic fin surfaces. On the other hand, the water saturation was found to vary very little on the coated hydrophilic fin surfaces for the plain-fins and the louvre fins types of heat exchangers. As for the effect of different water *U*, the water saturation in the ideal geometry was not affected much.

Table 5.3: Water retention in different types of porous media

Reference	Porous structure	Effect of different hydrophobicity	Effect of different U
Present research	Ideal geometry	Retains a lesser amount of water at a higher hydrophobicity.	The volume of water changes very little for all *U*.
	Porous metal		Retains a higher amount of water for lower *U*.
Hu et al. (2017)	Metal foam		N/A
Liu and Jacobi (2008)	Plain-fins round-tubes heat exchanger	Retains a lesser volume of water for hydrophobic conditions.	Retains a lesser volume of water for lower U.
	Plain-fins round-tubes and Louvre fins heat exchangers	The volume of water changes very little for different hydrophilic conditions.	N/A

The uniformity of the struts structure enables it to break the water surface easily. For the porous metal geometry, it retains a higher volume of water for lower U, but it was the opposite for plain-fins round-tubes heat exchanger.

5.5 Summary

The identified parameters of the porous metal are PPI, porosity, structural homogeneity and number of junctions. The structural homogeneity and the number of junctions can be quantified using the method as described in this chapter. It involves measuring the junction positions and the variation in the number of connecting struts to a junction. Also, it uses a modified formula of relative standard deviation for analysing the data. Two types of graphs were used, *i.e.*, the local structural homogeneity and the number of junctions for determining the location of the large pores which could further reduce the capacity in retaining water. The results showed both the geometries retained more volume of water at higher hydrophilicity. The water saturation in the ideal geometry is independent of the U. On the other hand, the water saturation in the porous metal decreases with higher U. The very different water retention behaviour under different U for both geometries has signified the influence of the additional parameters *i.e.,* structural homogeneity and number of junctions.

CHAPTER 6: CONCLUSIONS

6.1 Conclusions

The popular topics in water mobility modelling are related to cases like the droplet sliding down and the phenomenon of droplet jumping upon coalescence on the superhydrophobic surface. It is anticipated that the future research of droplet dynamics behaviour will focus on mixed types of surfaces, different g-forces and other external factors like flow and heat transfer especially in confined geometry like microchannel in the application of PEMFC. In that application, the publication related to the optimum microchannel design for dispensing is lacking.

The present research performed the CFD modelling of droplet sliding down on surface for several types of conditions, *i.e.*, hydrophilic, hydrophobic and super-hydrophobic. The results were accurate for the case of hydrophilic with boundary condition of no-slip wall and the case of hydrophobic with the slip-wall condition when compared with the experimental results from the literature. On the other hand, the modelling of the super-hydrophobic surface was inaccurate even though the droplet shape was close to the experimental results from the literature. The inconsistency was resulted due to the limitation in the CFD modelling. The droplet conformed fully with the plain floor whereas the real droplet rests with short contact length on the superhydrophobic surface and able to slide freely on the surface.

The present research discovered a new phenomenon was discovered where the droplet accelerates on a hydrophilic cavity surface when sliding down from a hydrophobic surface. The finding is useful for creating an effective way of filling liquids into cavities for passive microfluidics related devices. A detailed study on droplet mobility and cavity fillings resulted from a titled surface or substrate with cavities were carried out by CFD means. The present research investigated the effect of having different configurations of hydrophobicity for cavity and non-cavity surfaces, cavity depths, several cavity spacing,

tilted angles of a substrate and initial droplet volumes. The reduction of the cavity hydrophobicity, or making it more hydrophilic, does not have a linear effect in terms of improving droplet mobility and cavity filling. An increase of the plate tilted angle gives an incremental effect on the droplet mobility and the cavity filling. An increase of the initial droplet volume increases the number of filled cavity but decreases the filled volume. A deep cavity can hold-up a larger volume of fluid, which directly impedes the droplet mobility and cavity filling further downstream. The effect of the gap size between the two cavities is negligible provided that the gap is more than two times larger than the cavity diameter.

In the other work, a method was developed to quantify the structural variations or interior shapes of a open-type metallic foam structure*, i.e.,* the porous metal. In that method, the structural homogeneity and the number of junctions are found to be the third and fourth parameters of porous metal besides PPI and porosity. With that information, the present research able to detect the location of large pores in porous metal. The simulation showed that large pores would reduce the ability for water retention. The simulation results showed that the ideal and the porous metal geometries retain more volume of water at higher hydrophilicity. On the other hand, the results showed that the water saturation in the ideal geometry was independent of drainage velocity but it was otherwise for the porous metal geometry.

6.2 Applications and Future Work

The contents in the literature anticipated that the future research in water mobility behaviour will focus on the use of mixed hydrophobicity surfaces in the application which uses microchannel, *e.g.*, microfluidics devices and fuel cells technology for transportation application. In addition, the external physical influences like vibrations, external body force or heat transfer will be included as well. The present findings in the newly proposed

microfluidics device for droplet generation can be related to passive surface control for heat transfer. On the other hand, the present research had showed that the structural 'randomness' in metallic foam like the porous metal can be quantified and relatable to the water retention behaviour. It provides meaningful insight in designing fins which will work effectively in the application of cooling and dehumidification. As aligned with the need for developing manufacturing technology through the use of automation and robotics, the same know-how can be developed into computer algorithm for checking the metallic foam shapes in large quantity at the early stage of manufacturing and reduced the number of tests indirectly.

References

Ahmed, G., Sellier, M., Jermy, M., & Taylor, M. (2014). Modeling the effects of contact angle hysteresis on the sliding of droplets down inclined surfaces. *European Journal of Mechanics, B/Fluids*, *48*(1), 218–230. https://doi.org/10.1016/j.euromechflu.2014.06.003

Ahmed, G., Sellier, M., Lee, Y. C., Jermy, M., & Taylor, M. (2013). Modeling the spreading and sliding of power-law droplets. *Colloids and Surfaces A: Physicochemical and Engineering Aspects*, *432*(17), 2–7. https://doi.org/10.1016/j.colsurfa.2013.05.015

Baah, D., Tigner, J., Bean, K., Walker, N., Britton, B., & Floyd-Smith, T. (2012). Microfluidic synthesis and post-processing of non-spherical polymeric microparticles. *Microfluidics and Nanofluidics*, *12*(1–4), 657–662. https://doi.org/10.1007/s10404-011-0874-6

Babcsán, N., Banhart, J., & Leitlmeier, D. (2003). Metal foams manufacture and physics of foaming. In *International Conference Advanced Metallic Material*. Smolenice, Slovakia. Retrieved from https://www.researchgate.net/publication/40828766_Metal_foams_manufacture_and_physics_of_foaming

Banhart, J. (2001). Manufacture, characterisation and application of cellular metals and metal foams. *Progress in Materials Science*, *46*(6), 559–632. https://doi.org/10.1016/S0079-6425(00)00002-5

Banhart, J. (2013). Light-metal foams-history of innovation and technological challenges. *Advanced Engineering*, *15*(3), 82–111. https://doi.org/10.1002/adem.201200217

Barkhudarov, M. R. (2003). *Semi-Lagrangian VOF advection method for FLOW-3D*. *Flow Science, Inc.* (Vol. FSI-03-TN6).

Barthlott, W., & Neinhuis, C. (1997). Purity of the sacred lotus, or escape from contamination in biological surfaces. *Planta*, *202*(1), 1–8. https://doi.org/10.1007/s004250050096

Bazylak, A., Sinton, D., & Djilali, N. (2008). Dynamic water transport and droplet emergence in PEMFC gas diffusion layers. *Journal of Power Sources*, *176*(1), 240–246. https://doi.org/10.1016/j.jpowsour.2007.10.066

Bico, J., Marzolin, C., & Qu, D. (1999). Pearl drops. *Europhysics Letters (EPL)*, *47*(2), 220–226. https://doi.org/https://doi.org/10.1209/epl/i1999-00453-y

Boreyko, J. B., & Chen, C. H. (2009). Self-propelled dropwise condensate on superhydrophobic surfaces. *Physical Review Letters*, *103*(18), 184501. https://doi.org/10.1103/PhysRevLett.103.184501

Boreyko, J. B., & Collier, C. P. (2013). Delayed frost growth on jumping-drop superhydrophobic surfaces. *ACS Nano*, *7*(2), 1618–1627. https://doi.org/10.1021/nn3055048

Bormashenko, E., & Faculty, P. (2015). Progress in understanding wetting transitions on rough surfaces. *Advances in Colloid and Interface Science*, *222*(8), 92–103. https://doi.org/10.1016/j.cis.2014.02.009

Byun, S., & Kwak, D. (2019). Removal of flooding in a PEM fuel cell at cathode by flexural Wave. *Journal of Electrochemical Science and Technology*, *10*(2), 104–114. https://doi.org/10.5229/JECST.2019.10.2.104

Cao, L., Jones, A. K., Sikka, V. K., Wu, J., & Gao, D. (2009). Anti-icing superhydrophobic coatings. *Langmuir*, *25*(21), 12444–12448. https://doi.org/10.1021/la902882b

Carey, V. P. (2008). *Liquid-vapor phase change phenomena*. (S. Scholl, Ed.) (2nd ed.). New York: Taylor & Francis Group.

Carreras, M. P., & Wang, S. (2017). A multifunctional microfluidic platform for

generation, trapping and release of droplets in a double laminar flow. *Journal of Biotechnology*, *251*(23), 106–111. https://doi.org/10.1016/j.jbiotec.2017.04.030
Cassie, A. B. D., & Baxter, S. (1944). Wettability of porous surfaces. *Transactions of the Faraday Society*, *40*(0), 546. https://doi.org/10.1039/tf9444000546
Chang, B., Zhou, Q., Ras, R. H. A., Shah, A., Wu, Z., & Hjort, K. (2016). Sliding droplets on hydrophilic/superhydrophobic patterned surfaces for liquid deposition. *Applied Physics Letters*, *108*(15), 154102. https://doi.org/10.1063/1.4947008
Cho, S. C., Wang, Y., & Chen, K. S. (2012). Droplet dynamics in a polymer electrolyte fuel cell gas flow channel: forces, deformation and detachment. II: comparisons of analytical solution with numerical and experimental results. *Journal of Power Sources*, *210*(4), 191–197. https://doi.org/10.1016/j.jpowsour.2012.03.033
Choi, W. K., Lebrasseur, E., A. Haq, M. I., Tsuchiya, H., Torii, T., Yamazaki, H., … Higuchi, T. (2007). Nano-liter size droplet dispenser using electrostatic manipulation technique. *Sensors and Actuators A: Physical*, *136*(1), 484–490. https://doi.org/10.1016/j.sna.2006.12.028
Chu, F., Wu, X., & Ma, Q. (2017). Condensed droplet growth on surfaces with various wettability. *Applied Thermal Engineering*, *115*(6), 1101–1108. https://doi.org/10.1016/j.applthermaleng.2017.01.060
Cui, J., Li, W., & Lam, W. H. (2011). Numerical investigation on drag reduction with superhydrophobic surfaces by lattice-Boltzmann method. *Computers and Mathematics with Applications*, *61*(12), 3678–3689. https://doi.org/10.1016/j.camwa.2010.07.037
Drelich, J., Wilbur, J. L., Miller, J. D., & Whitesides, G. M. (1996). Contact angles for liquid drops at a model heterogeneous. *Langmuir*, *12*(7), 1913–1922. https://doi.org/https://doi.org/10.1021/la9509763
Dreyfus, R., Tabeling, P., & Willaime, H. (2003). Ordered and disordered patterns in two-phase flows in microchannels. *Physical Review Letters*, *90*(14), 144505. https://doi.org/10.1103/PhysRevLett.90.144505
Dupont, J. B., & Legendre, D. (2010). Numerical simulation of static and sliding drop with contact angle hysteresis. *Journal of Computational Physics*, *229*(7), 2453–2478. https://doi.org/10.1016/j.jcp.2009.07.034
Ellinas, K., Pliaka, V., Kanakaris, G., Tserepi, A., Alexopoulos, L. G., & Gogolides, E. (2017). Micro-bead immunoassays for the detection of IL6 and PDGF-2 proteins on a microfluidic platform, incorporating superhydrophobic passive valves. *Microelectronic Engineering*, *175*(9), 73–80. https://doi.org/10.1016/j.mee.2017.02.015
Ellinas, K., Tserepi, A., & Gogolides, E. (2014). Superhydrophobic, passive microvalves with controllable opening threshold: exploiting plasma nanotextured microfluidics for a programmable flow switchboard. *Microfluidics and Nanofluidics*, *17*(3), 489–498. https://doi.org/10.1007/s10404-014-1335-9
ElSherbini, A. I., & Jacobi, A. M. (2004a). Liquid drops on vertical and inclined surfaces: I. An experimental study of drop geometry. *Journal of Colloid and Interface Science*, *273*(2), 556–565. https://doi.org/10.1016/j.jcis.2003.12.067
ElSherbini, A. I., & Jacobi, A. M. (2004b). Liquid drops on vertical and inclined surfaces: II. A method for approximating drop shapes. *Journal of Colloid and Interface Science*, *273*(2), 566–575. https://doi.org/10.1016/j.jcis.2003.12.043
ElSherbini, A. I., & Jacobi, A. M. (2006). Retention forces and contact angles for critical liquid drops on non-horizontal surfaces. *Journal of Colloid and Interface Science*, *299*(2), 841–849. https://doi.org/10.1016/j.jcis.2006.02.018
Everitt, B. S. (1998). *The Cambridge Dictionary of Statistics.* Cambridge UK: Cambridge University Press.
Fang, W., Mayama, H., & Tsujii, K. (2008). Formation mechanism of super water-

repellent fractal surfaces of alkylketene dimer. *Colloids and Surfaces A: Physicochemical and Engineering Aspects*, *316*(1–3), 258–265. https://doi.org/10.1016/j.colsurfa.2007.09.010

Farokhirad, S., Morris, J. F., & Lee, T. (2015). Coalescence-induced jumping of droplet: Inertia and viscosity effects. *Physics of Fluids*, *27*(10). https://doi.org/10.1063/1.4932085

Feng, B. L., Li, S. H., Li, Y. S., Li, H. J., Zhang, L. J., Zhai, J., … Zhu, D. B. (2002). Super-hydrophobic surfaces: from natural to artificial. *Advanced Materials*, *14*(24), 1857–1860. https://doi.org/DOI 10.1002/adma.200290020

Gañán C., A. M., & Barrero, A. (1999). A novel pneumatic technique to generate steady capillary microjets. *Journal of Aerosol Science*, *30*(1), 117–125. https://doi.org/10.1016/S0021-8502(98)00029-9

Ganesan, P. B., Islam, M. T., Pokrajac, D., Hamad, F. A., & Sandaran, S. C. (2017). Coalescence and rising behavior of co-axial and lateral bubbles in viscous fluid: a CFD study. *Asia-Pacific Journal of Chemical Engineering*, *12*(4), 605–619. https://doi.org/10.1002/apj.2102

Ganesan, P. B., Vanakia, S. M., Thoo, K. K., & Chin, W. M. (2016). Air-side heat transfer characteristics of hydrophobic and super-hydrophobic fin surfaces in heat exchangers: A review. *International Communications in Heat and Mass Transfer*, *74*(6), 27–35. https://doi.org/10.1016/j.icheatmasstransfer.2016.02.017

Garrod, R. P., Harris, L. G., Schofield, W. C. E., Mcgettrick, J., Ward, L. J., Teare, D. O. H., & Badyal, J. P. S. (2007). Mimicking a Stenocara beetle ' s back for microcondensation using plasmachemical patterned superhydrophobic - superhydrophilic surfaces. *Langmuir*, *23*(2), 689–693. https://doi.org/10.1021/la0610856

Gogte, S., Vorobieff, P., Truesdell, R., Mammoli, A., van Swol, F., Shah, P., & Brinker, C. J. (2005). Effective slip on textured superhydrophobic surfaces. *Physics of Fluids*, *17*(5), 1–4. https://doi.org/10.1063/1.1896405

Gopalan, P., & Kandlikar, S. G. (2013). Effect of channel material on water droplet dynamics in a PEMFC gas channel. *Journal of the Electrochemical Society*, *160*(6), F487–F495. https://doi.org/10.1149/2.030306jes

Gopalan, P., & Kandlikar, S. G. (2014). Modeling dynamic interaction between an emerging water droplet and the sidewall of a trapezoidal channel. *Colloids and Surfaces A: Physicochemical and Engineering Aspects*, *441*(2), 262–274. https://doi.org/10.1016/j.colsurfa.2013.09.013

Hao, L., & Cheng, P. (2010). An analytical model for micro-droplet steady movement on the hydrophobic wall of a micro-channel. *International Journal of Heat and Mass Transfer*, *53*(5–6), 1243–1246. https://doi.org/10.1016/j.ijheatmasstransfer.2009.11.010

Harlow, F. H. (1966). Numerical study of large-amplitude free-surface motions. *Physics of Fluids*, *9*(5), 842. https://doi.org/10.1063/1.1761784

Hartnig, C., Manke, I., Kuhn, R., Kleinau, S., Goebbels, J., & Banhart, J. (2009). High-resolution in-plane investigation of the water evolution and transport in PEM fuel cells. *Journal of Power Sources*, *188*(2), 468–474. https://doi.org/10.1016/j.jpowsour.2008.12.023

He, B., Lee, J., & Patankar, N. A. (2004). Contact angle hysteresis on rough hydrophobic surfaces. *Colloids and Surfaces A: Physicochem. Eng. Aspects*, *248*(1–3), 101–104. https://doi.org/10.1016/j.colsurfa.2004.09.006

He, B., Patankar, N. A., & Lee, J. (2003). Multiple equilibrium droplet shapes and design criterion for rough hydrophobic surfaces. *Langmuir*, *19*, 4999–5003. https://doi.org/10.1021/la0268348

He, T., Wang, Y., Zhang, Y., lv, Q., Xu, T., & Liu, T. (2009). Super-hydrophobic

surface treatment as corrosion protection for aluminum in seawater. *Corrosion Science*, *51*(8), 1757–1761. https://doi.org/10.1016/j.corsci.2009.04.027
He, X., & Luo, L. (1997). Theory of the lattice Boltzmann method: from the Boltzmann equation to the lattice Boltzmann equation. *Physical Review E*, *56*(6), 6811–6817.
Herranz B., B., Ginestar, E., Zhang, H. b., Hirvonen, J., & Santos, H. A. (2017). Microfluidics platform for glass capillaries and its application in droplet and nanoparticle fabrication. *International Journal of Pharmaceutics*, *516*(1–2), 100–105. https://doi.org/10.1016/j.ijpharm.2016.11.024
Hirt, C. W., & Nichols, B. D. (1981). Volume of Fluid (VOF) method for the dynamics of free boundaries. *Journal of Computational Physics*, *39*(1), 201–225. https://doi.org/10.1016/0021-9991(81)90145-5
Hou, Y., Deng, H., Du, Q., & Jiao, K. (2018). Multi-component multiphase lattice Boltzmann modeling of droplet coalescence in flow channel of fuel cell. *Journal of Power Sources*, *393*(21), 83–91. https://doi.org/10.1016/j.jpowsour.2018.05.008
Hu, H., Lai, Z., Ding, G., Zhuang, D., & Weng, X. (2017). Experimental investigation on water drainage characteristics of open-cell metal foams with different wettabilities. *International Journal of Refrigeration*, *79*(7), 101–113. https://doi.org/10.1016/j.ijrefrig.2017.04.002
Hu, H. W., Tang, G. H., & Niu, D. (2016). Experimental investigation of convective condensation heat transfer on tube bundles with different surface wettability at large amount of noncondensable gas. *Applied Thermal Engineering*, *100*(9), 699–707. https://doi.org/10.1016/j.applthermaleng.2016.02.086
Huang, J., Fan, R., Connor, S., & Yang, P. (2007). One-step patterning of aligned nanowire arrays by programmed dip coating. *Angewandte Chemie International Edition*, *46*(14), 2414–2417. https://doi.org/10.1002/anie.200604789
Islam, M. T., Ganesan, P., Sahu, J. N., & Hamad, F. A. (2015). Numerical study of co-axial bubble coalescence characteristics. *Asia-Pacific Journal of Chemical Engineering*, *10*(5), 670–680. https://doi.org/10.1002/apj.1898
Jhee, S., Lee, K. S., & Kim, W. S. (2002). Effect of surface treatments on the frosting/defrosting behavior of a fin-tube heat exchanger. *International Journal of Refrigeration*, *25*(8), 1047–1053. https://doi.org/10.1016/S0140-7007(02)00008-7
Jin, Z., Zhang, H., & Yang, Z. (2016). The impact and freezing processes of a water droplet on a cold surface with different inclined angles. *International Journal of Heat and Mass Transfer*, *103*(12), 886–893. https://doi.org/10.1016/j.ijheatmasstransfer.2016.08.012
Joardar, A., Jacobi, A. M., & Gu, Z. P. (2004). Assessing the condensate-drainage behavior of dehumidifying heat exchangers. In *International refrigeration and air conditioning conference* (p. 639). Purdue e-Pubs, Purdue University. Retrieved from http://docs.lib.purdue.edu/iracc/639
Kamali, R., Khojasteh, D., & Mousavi, S. M. (2016). Newtonian and non-Newtonian droplet impact onto a heated hydrophobic solid surface. In *24th Annual International Conference on Mechanical Engineering* (p. 24486). Retrieved from https://www.researchgate.net/publication/301731946
Khatir, Z., Kubiak, K. J., Jimack, P. K., & Mathia, T. G. (2016). Dropwise condensation heat transfer process optimisation on superhydrophobic surfaces using a multi-disciplinary approach. *Applied Thermal Engineering*, *106*(15), 1337–1344. https://doi.org/10.1016/j.applthermaleng.2016.06.128
Khojasteh, D., Kazerooni, M., Salarian, S., & Kamali, R. (2016). Droplet impact on superhydrophobic surfaces : A review of recent developments. *Journal of Industrial and Engineering Chemistry*, *42*(10), 1–14. https://doi.org/10.1016/j.jiec.2016.07.027
Kim, D. E., Ahn, H. S., & Kwon, T. S. (2017). Experimental investigation of filmwise

and dropwise condensation inside transparent circular tubes. *Applied Thermal Engineering*, *110*(1), 412–423. https://doi.org/10.1016/j.applthermaleng.2016.08.175

Kim, G., Lee, H., & Webb, R. L. (2002). Plasma hydrophilic surface treatment for dehumidifying heat exchangers. *Experimental Thermal and Fluid Science*, *27*(1), 1–10. https://doi.org/10.1016/S0894-1777(02)00219-4

Kim, M., Kim, H., Lee, K., & Kim, D. R. (2017). Frosting characteristics on hydrophobic and superhydrophobic surfaces : A review. *Energy Conversion and Management*, *138*(8), 1–11. https://doi.org/10.1016/j.enconman.2017.01.067

Koh, Y. Y., Lee, Y. C., Gaskell, P. H., Jimack, P. K., & Thompson, H. M. (2009). Droplet migration: Quantitative comparisons with experiment. *European Physical Journal: Special Topics*, *166*(1), 117–120. https://doi.org/10.1140/epjst/e2009-00890-2

Krasovitski, B., & Marmur, A. (2005). Drops down the hill : Theoretical study of limiting contact angles and the hysteresis range on a tilted plate. *Langmuir*, *21*(9), 3881–3885. https://doi.org/10.1021/la0474565

Kulju, S., Riegger, L., Koltay, P., Mattila, K., & Hyväluoma, J. (2018). Fluid flow simulations meet high-speed video : Computer vision comparison of droplet dynamics. *Journal of Colloid And Interface Science*, *522*(20), 48–56. https://doi.org/10.1016/j.jcis.2018.03.053

Kumar, A., & Reddy, R. G. (2003). Modeling of polymer electrolyte membrane fuel cell with metal foam in the flow-field of the bipolar/end plates. *Journal of Power Sources*, *114*(1), 54–62. https://doi.org/10.1016/S0378-7753(02)00540-2

Lavi, B., & Marmur, A. (2004). The exponential power law: Partial wetting kinetics and dynamic contact angles. *Colloids and Surfaces A: Physicochemical and Engineering Aspects*, *250*(1–3), 409–414. https://doi.org/10.1016/j.colsurfa.2004.04.079

Lee, C., Lyu, S., Park, J. W., & Hwang, W. (2016). Lattice Boltzmann simulation of the movement of droplets on stripe-patterned surfaces having different wettability. *Advances in Engineering Software*, *91*(1), 44–50. https://doi.org/10.1016/j.advengsoft.2015.10.001

Lefebvre, L. P., Banhart, J., & Dunand, D. C. (2008). Porous metals and metallic foams: Current status and recent developments. *Advaced Engineering Materials*, *10*(9), 775–787. https://doi.org/10.1002/adem.200800241

Li, Q., Luo, K. H., & Li, X. J. (2013). Lattice Boltzmann modeling of multiphase flows at large density ratio with an improved pseudopotential model. *Physical Review E*, *87*(5), 053301. https://doi.org/10.1103/PhysRevE.87.053301

Li, X., Zhang, L., Ma, X., & Zhang, H. (2016). Dynamic characteristics of droplet impacting on prepared hydrophobic superhydrophobic silicon surfaces. *Surface & Coatings Technology*, *307*(23, Part A), 243–253. https://doi.org/10.1016/j.surfcoat.2016.08.089

Liebscher, A., Proppe, C., Redenbach, C., & Schwarzer, D. (2013). Stochastic multiscale modeling of metal foams. In *IUTAM Symposium on Multiscale Problems in Stochastic Mechanics* (Vol. 6, pp. 87–96). Karlsruhe, Germany: Elsevier B.V. https://doi.org/10.1016/j.piutam.2013.01.010

Lin, Y., Wu, Z., Gao, Y., Wu, J., & Wen, W. (2018). High-throughput controllable generation of droplet arrays with low consumption. *Applied Surface Science*, *442*(16), 189–194. https://doi.org/10.1016/j.apsusc.2018.02.055

Liu, F., Ghigliotti, G., Feng, J. J., & Chen, C. H. (2014). Self-propelled jumping upon drop coalescence on Leidenfrost surfaces. *Journal of Fluid Mechanics*, *752*(15), 22–38. https://doi.org/10.1017/jfm.2014.319

Liu, L., & Jacobi, A. M. (2006). The effects of hydrophilicity on water drainage and

condensate retention on air-conditioning evaporators. In *International Refrigeration and Air Conditioning Conference* (pp. 1–8). Indiana, U.S.: School of Mechanical Engineering, Purdue University. Retrieved from http://docs.lib.purdue.edu/iracc/847

Liu, L., & Jacobi, A. M. (2008). Issues affecting the reliability of dynamic dip testing as a method to assess the condensate drainage behavior from the air-side surface of dehumidifying heat exchangers. *Experimental Thermal and Fluid Science*, *32*(8), 1512–1522. https://doi.org/10.1016/j.expthermflusci.2008.04.006

Liu, X., & Cheng, P. (2015). 3D multiphase lattice Boltzmann simulations for morphological effects on self-propelled jumping of droplets on textured superhydrophobic surfaces. *International Communications in Heat and Mass Transfer*, *64*(5), 7–13. https://doi.org/10.1016/j.icheatmasstransfer.2015.03.002

Liu, X., Cheng, P., & Quan, X. (2014). Lattice Boltzmann simulations for self-propelled jumping of droplets after coalescence on a superhydrophobic surface. *International Journal of Heat and Mass Transfer*, *73*(6), 195–200. https://doi.org/10.1016/j.ijheatmasstransfer.2014.01.060

Liu, Z. M., Yang, Y., Du, Y., & Pang, Y. (2017). Advances in droplet-based microfluidic technology and its applications. *Chinese Journal of Analytical Chemistry*, *45*(2), 282–296. https://doi.org/10.1016/S1872-2040(16)60982-9

Loyselle, P., & Prokopius, K. (2011). *Teledyne Energy Systems , Inc ., Proton Exchange Member (PEM) Fuel Cell Engineering Model Powerplant*. Ohio. Retrieved from https://ntrs.nasa.gov/archive/nasa/casi.ntrs.nasa.gov/20110014968.pdf

Lv, C., Hao, P., Yao, Z., Song, Y., Zhang, X., & He, F. (2013). Condensation and jumping relay of droplets on lotus leaf. *Applied Physics Letters*, *103*(2), 021601. https://doi.org/10.1063/1.4812976

Marcinichen, J. B., Olivier, J. A., Oliveira, V. de, & Thome, J. R. (2012). A review of on-chip micro-evaporation: Experimental evaluation of liquid pumping and vapor compression driven cooling systems and control. *Applied Energy*, *92*(4), 147–161. https://doi.org/10.1016/j.apenergy.2011.10.030

Matsui, H., Noda, Y., & Hasegawa, T. (2012). Hybrid energy-minimization simulation of equilibrium droplet shapes on hydrophilic hydrophobic patterned surfaces. *Langmuir*, *28*(44), 15450–15453. https://doi.org/10.1021/la303717n

McDonald, J. C., & Whitesides, G. M. (2002). Poly(dimethylsiloxane) as a material for fabricating microfluidic devices. *Accounts of Chemical Research*, *35*(7), 491–499. https://doi.org/10.1021/ar010110q

McHale, G., Rowan, S. M., Newton, M. I., & Banerjee, M. K. (1998). Evaporation and the wetting of a low-energy solid surface. *The Journal of Physical Chemistry B*, *102*(11), 1964–1967. https://doi.org/10.1021/jp972552i

Mchale, G., Shirtcliffe, N. J., & Newton, M. I. (2004). Contact-angle hysteresis on super-hydrophobic surfaces. *Langmuir*, *20*(23), 10146–10149. https://doi.org/10.1021/la0486584

Miljkovic, N., Preston, D. J., Enright, R., & Wang, E. N. (2013). Electric-field-enhanced condensation on superhydrophobic nanostructured surfaces. *ACS Nano*, *7*(12), 11043–11054. https://doi.org/10.1021/nn404707j

Min, J., & Webb, R. L. (2000). Condensate carryover phenomena in dehumidifying, finned-tube heat exchangers. *Experimental Thermal and Fluid Science*, *22*(3–4), 175–182. https://doi.org/10.1016/S0894-1777(00)00024-8

Moallem, E., Padhmanabhan, S., Cremaschi, L., & Fisher, D. E. (2012). Experimental investigation of the surface temperature and water retention effects on the frosting performance of a compact microchannel heat exchanger for heat pump systems. *International Journal of Refrigeration*, *35*(1), 171–186. https://doi.org/10.1016/j.ijrefrig.2011.08.010

Moffat, J. R., Sefiane, K., & Shanahan, M. E. R. (2009). Nanofluid droplet evaporation kinetics and wetting dynamics on flat substrates. *Journal of Nano Research*, *7*(11), 75–80. https://doi.org/10.4028/www.scientific.net/JNanoR.7.75

Mortazavi, M., Santamaria, A. D., Chauhan, V., & Benner, J. Z. (2019). Enhanced water removal from PEM fuel cells using acoustic pressure waves. *Journal of The Electrochemical Society*, *166*(7), F3143–F3153. https://doi.org/10.1149/2.0211907jes

Nabavi, S. A., Gu, S., Vladisavljević, G. T., & Ekanem, E. E. (2015). Dynamics of double emulsion break-up in three phase glass capillary microfluidic devices. *Journal of Colloid and Interface Science*, *450*(14), 279–287. https://doi.org/10.1016/j.jcis.2015.03.032

Nam, Y., Kim, H., & Shin, S. (2013). Energy and hydrodynamic analyses of coalescence-induced jumping droplets. *Applied Physics Letters*, *103*(16). https://doi.org/10.1063/1.4825273

Okada, T., Xie, G., & Meeg, M. (1998). Simulation for water management in membranes for polymer electrolyte fuel cells. *Electrochimica Acta*, *43*(14–15), 2141–2155. https://doi.org/10.1016/S0013-4686(97)10099-8

Oliveira, L. de, Lopes, D., Ramos, S., & Mombach, J. (2011). Two-dimensional modeling of the superhydrophobic behavior of a liquid droplet sliding down a ramp of pillars. *Soft Matter*, *7*, 3763–3765. https://doi.org/10.1039/c0sm01178a

Oliveira, M. B., Salgado, C. L., Song, W., & Mano, J. F. (2013). Combinatorial on-chip study of miniaturized 3D porous scaffolds using a patterned superhydrophobic platform. *Small*, *9*(5), 768–778. https://doi.org/10.1002/smll.201201436

Onda, T., Shibuichi, S., Satoh, N., & Tsujii, K. (1996). Super-water-repellent fractal surfaces. *Langmuir*, *12*(9), 2125–2127. https://doi.org/10.1021/la950418o

Önnerfjord, P., Nilsson, J., Wallman, L., Laurell, T., & Marko-Varga, G. (1998). Picoliter Sample Preparation in MALDI-TOF MS using a micromachined silicon flow-through dispenser. *Analytical Chemistry*, *70*(22), 4755–4760. https://doi.org/10.1021/ac980207z

Palan, V., Shepard, S. W. J., & Williams, A. K. (2006). Removal of excess product water in a PEM fuel cell stack by vibrational and acoustical methods. *Journal of Power Sources*, *161*(2), 1116–1125. https://doi.org/https://doi.org/10.1016/j.jpowsour.2006.06.021

Patankar, N. A. (2003). On the modeling of hydrophobic contact angles on rough surfaces. *Langmuir*, *19*(4), 1249–1253. https://doi.org/https://doi.org/10.1021/la026612+

Patil, N., & Bhardwaj, R. (2014). Evaporation of a Sessile Microdroplet on a Heated Hydrophobic Substrate. *International Journal of Micro-Nano Scale Transport*, *5*(2), 51–58. https://doi.org/10.1260/1759-3093.5.2.51

Patil, N. D., Gada, V. H., Sharma, A., & Bhardwaj, R. (2016). On dual-grid level-set method for contact line modeling during impact of a droplet on hydrophobic and superhydrophobic surfaces. *International Journal of Multiphase Flow*, *81*(4), 54–66. https://doi.org/10.1016/j.ijmultiphaseflow.2016.01.005

Peng, B., Wang, S., Lan, Z., Xu, W., Wen, R., & Ma, X. (2013). Analysis of droplet jumping phenomenon with lattice Boltzmann simulation of droplet coalescence. *Applied Physics Letters*, *102*(15). https://doi.org/10.1063/1.4799650

Perumal, D. A., & Dass, A. K. (2015). A review on the development of lattice Boltzmann computation of macro fluid flows and heat transfer. *Alexandria Engineering Journal*, *54*(4), 955–971. https://doi.org/10.1016/j.aej.2015.07.015

Platzman, I., Janiesch, J. W., & Spatz, J. P. (2013). Synthesis of nanostructured and biofunctionalized water-in-oil droplets as tools for homing T cells. *Journal of the American Chemical Society*, *135*(9), 3339–3342. https://doi.org/10.1021/ja311588c

Podgorski, T., Flesselles, J. M., & Limat, L. (2001). Corners, cusps, and pearls in running drops. *Physical Review Letters*, *87*(3), 361021–361024. https://doi.org/10.1103/PhysRevLett.87.036102

Popova, A. A., Schillo, S. M., Demir, K., Ueda, E., Nesterov M., A., & Levkin, P. A. (2015). Droplet-array (DA) sandwich chip: A versatile platform for high-throughput cell screening based on superhydrophobic-superhydrophilic micropatterning. *Advanced Materials*, *27*(35), 5217–5222. https://doi.org/10.1002/adma.201502115

Qin, C., Rensink, D., & Hassanizadeh, S. (2012). Direct simulation of liquid water dynamics in the gas channel of a polymer electrolyte fuel cell. *Journal of The Electrochemical Society*, *159*(4), 434–443. https://doi.org/10.1149/2.004205jes

Raj, S. V. (2011). *Microstructural characterization of metal foams : An examination of the applicability of the theoretical models for modeling foams*. Cleveland, Ohio. Retrieved from http://gltrs.grc.nasa.gov

Ramos, S. M. M., Benyagoub, A., Canut, B., & Jamois, C. (2010). Superoleophobic behavior induced by nanofeatures on oleophilic surfaces. *Langmuir*, *26*(7), 5141–5146. https://doi.org/10.1021/la9036138

Ravi, A. S., Murthy, J. Y., & Garimella, S. V. (2012). Prediction of droplet dynamics on an incline. *International Journal of Heat and Mass Transfer*, *55*(5–6), 1466–1474. https://doi.org/10.1016/j.ijheatmasstransfer.2011.10.028

Ren, H., Fair, R. B., & Pollack, M. G. (2004). Automated on-chip droplet dispensing with volume control by electro-wetting actuation and capacitance metering. *Sensors and Actuators B: Chemical*, *98*(2–3), 319–327. https://doi.org/10.1016/j.snb.2003.09.030

Repossi, E., Verani, M., & Rosso, R. (2015). *On the mathematical modeling of a metal foam expansion process*. Politecnico Di Milano.

Saffari, H., Sohrabi, B., Noori, M. R., & Bahrami, H. R. T. (2018). Optimal condition for fabricating superhydrophobic Aluminum surfaces with controlled anodizing processes. *Applied Surface Science*, *435*(9), 1322–1328. https://doi.org/10.1016/j.apsusc.2017.11.188

Sakai, M, Song, J. H., Yoshida, N., Suzuki, S., Kameshima, Y., & Nakajima, A. (2006). Direct observation of internal fluidity in a water droplet during sliding on hydrophobic surfaces. *Langmuir*, *22*(11), 4906–4909. https://doi.org/10.1021/la060323u

Sakai, Munetoshi. (2006). Relationship between sliding acceleration of water droplets and dynamic contact angles on hydrophobic surfaces. *Surface Science*, *600*(16), L204–L208. https://doi.org/10.1016/j.susc.2006.06.039

Schleizer, A. D., & Bonnecaze, R. T. (1999). Displacement of a two-dimensional immiscible droplet adhering to a wall in shear and pressure-driven flows. *Journal of Fluid Mechanics*, *383*(6), 29–54. https://doi.org/10.1017/S0022112098003462

Schwartz, L. W. (1998). Hysteretic effects in droplet motions on heterogeneous substrates : direct numerical simulation. *Langmuir*, *14*(12), 3440–3453. https://doi.org/https://doi.org/10.1021/la971407t

Schwartz, L. W., Roux, D., & Cooper White, J. J. (2005). On the shapes of droplets that are sliding on a vertical wall. *Physica D*, *209*(1–4), 236–244. https://doi.org/10.1016/j.physd.2005.07.001

Shan, X., & Chen, H. (1994). Simulation of nonideal gases and liquid-gas phase transitions by the lattice Boltzmann equation. *Physical Review E*, *49*(4), 2941–2948. https://doi.org/10.1103/PhysRevE.49.2941

Shang, X., Luo, Z., Ya, E., Kabov, O. A., & Bai, B. (2018). GNBC-based front-tracking method for the three-dimensional simulation of droplet motion on a solid surface. *Computers and Fluids*, *172*, 181–195.

https://doi.org/10.1016/j.compfluid.2018.06.021
Shi, Y., & Tang, G. H. (2018). Investigation of coalesced droplet vertical jumping and horizontal moving on textured surface using the lattice Boltzmann method. *Computers and Mathematics with Applications*, *75*(4), 1213–1225. https://doi.org/10.1016/j.camwa.2017.10.024
Shi, Y., Tang, G. H., & Xia, H. H. (2015). Investigation of coalescence-induced droplet jumping on superhydrophobic surfaces and liquid condensate adhesion on slit and plain fins. *International Journal of Heat and Mass Transfer*, *88*(4), 445–455. https://doi.org/10.1016/j.ijheatmasstransfer.2015.04.085
Shibuichi, S., Yamamoto, T., Onda, T., & Tsujii, K. (1998). Super water- and oil-repellent surfaces resulting from fractal structure. *Journal of Colloid and Interface Science*, *208*(1), 287–294. https://doi.org/10.1006/jcis.1998.5813
Spelt, P. D. M. (2005). A level-set approach for simulations of flows with multiple moving contact lines with hysteresis. *Journal of Computational Physics*, *207*(2), 389–404. https://doi.org/10.1016/j.jcp.2005.01.016
Suzuki, S., Nakajima, A., Kameshima, Y., & Okada, K. (2004). Elongation and contraction of water droplet during sliding on the silicon surface treated by fluoroalkylsilane. *Surface Science Letters*, *557*(1–3), L163–L168. https://doi.org/10.1016/j.susc.2004.02.029
Suzuki, S., Nakajima, A., & Tanaka, K. (2008). Sliding behavior of water droplets on line-patterned hydrophobic surfaces. *Applied Surface Science*, *254*(6), 1797–1805. https://doi.org/10.1016/j.apsusc.2007.07.171
Tavakoli, F., & Kavehpour, H. P. (2015). Cold-induced spreading of water drops on hydrophobic surfaces. *Langmuir*, *31*(7), 2120–2126. https://doi.org/10.1021/la503620a
Thanh vinh, N., Takahashi, H., Matsumoto, K., & Shimoyama, I. (2015). Two-axis MEMS-based force sensor for measuring the interaction forces during the sliding of a droplet on a micropillar array. *Sensors & Actuators: A. Physical*, *231*(11), 35–43. https://doi.org/10.1016/j.sna.2014.09.015
Theodorakakos, A., Ous, T., Gavaises, M., Nouri, J. M., Nikolopoulos, N., & Yanagihara, H. (2006). Dynamics of water droplets detached from porous surfaces of relevance to PEM fuel cells. *Journal of Colloid and Interface Science*, *300*(2), 673–687. https://doi.org/10.1016/j.jcis.2006.04.021
Thorsen, T., Roberts, R. W., Arnold, F. H., & Quake, S. R. (2001). Dynamic pattern formation in a vesicle-generating microfluidic device. *Physical Review Letters*, *86*(18), 4163–4166. https://doi.org/10.1103/PhysRevLett.86.4163
Ueda, E., & Levkin, P. A. (2013). Emerging applications of superhydrophilic-superhydrophobic micropatterns. *Advanced Materials*, *25*(9), 1234–1247. https://doi.org/10.1002/adma.201204120
Venkateshan, D. G., & Tafreshi, H. V. (2018). Modelling droplet sliding angle on hydrophobic wire screens. *Colloids and Surfaces A: Physicochemical and Engineering Aspects*, *538*(3), 310–319. https://doi.org/10.1016/j.colsurfa.2017.11.003
Vladisavljević, G. T., Ekanem, E. E., Zhang, Z., Khalid, N., Kobayashi, I., & Nakajima, M. (2018). Long-term stability of droplet production by microchannel (step) emulsification in microfluidic silicon chips with large number of terraced microchannels. *Chemical Engineering Journal*, *333*(3), 380–391. https://doi.org/10.1016/j.cej.2017.09.141
Wang, C. C., & Chang, C. T. (1998). Heat and mass transfer for plate fin-and-tube heat exchangers, with and without hydrophilic coating. *International Journal of Heat and Mass Transfer*, *41*(20), 3109–3120. https://doi.org/10.1016/S0017-9310(98)00060-X

Wang, H., Tang, L., Wu, X., Dai, W., & Qiu, Y. (2007). Fabrication and anti-frosting performance of super hydrophobic coating based on modified nano-sized calcium carbonate and ordinary polyacrylate. *Applied Surface Science*, *253*(22), 8818–8824. https://doi.org/10.1016/j.apsusc.2007.04.006

Wang, R., Hashimoto, K., Fujishima, A., Chikuni, M., Kojima, E., Kitamura, A., … Watanabe, T. (1997). Light-induced amphiphilic surfaces. *Nature*, *388*(1), 431–432. https://doi.org/10.1038/41233

Wang, S., Yu, X., Liang, C., & Zhang, Y. (2018). Enhanced condensation heat transfer in air-conditioner heat exchanger using superhydrophobic foils. *Applied Thermal Engineering*, *137*(10), 758–766. https://doi.org/10.1016/j.applthermaleng.2018.04.020

Wang, X., & Yu, Y. (2012). Analysis of the shape of heavy droplets on flat and spherical surface. *Science China Physics, Mechanics and Astronomy*, *55*(6), 1118–1124. https://doi.org/10.1007/s11433-012-4750-5

Wang, Z. H., Wang, C. Y., & Chen, K. S. (2001). Two-phase flow and transport in the air cathode of proton exchange membrane fuel cells. *Journal of Power Sources*, *94*(1), 40–50. https://doi.org/10.1016/S0378-7753(00)00662-5

Washe, A. P., Lozano S., P., Bejarano N., D., Teixeira D., B., & Katakis, I. (2013). Electrochemically actuated passive stop-go microvalves for flow controlin microfluidic systems. *Microelectronic Engineering*, *111*(11), 416–420. https://doi.org/10.1016/j.mee.2013.04.022

Wenzel, R. N. (1949). Surface roughness and contact angle. *Journal of Physical & Colloid Chemistry*, *53*(9), 1466–1467. https://doi.org/10.1021/j150474a015

Wu, X. M., & Webb, R. L. (2001). Investigation of the possibility of frost release from a cold surface. *Experimental Thermal and Fluid Science*, *24*(3–4), 151–156. https://doi.org/10.1016/S0894-1777(01)00045-0

Wu, Y. (2006). Water droplets interaction with super-hydrophobic surfaces. *Surface Science*, *600*(18), 3710–3714. https://doi.org/10.1016/j.susc.2006.01.073

Wu, Y., Bekke, M., Inoue, Y., Sugimura, H., Kitaguchi, H., Liu, C., & Takai, O. (2004). Mechanical durability of ultra-water-repellent thin film by microwave plasma-enhanced CVD. *Thin Solid Films*, *457*(1), 122–127. https://doi.org/10.1016/j.tsf.2003.12.007

Wu, Y., Inoue, Y., Sugimura, H., Takai, O., Kato, H., Murai, S., & Oda, H. (2002). Characteristics of ultra water-repellent thin films prepared by combined process of microwave plasma-enhanced CVD and oxygen-plasma treatment. *Thin Solid Films*, *407*(1–2), 45–49. https://doi.org/10.1016/S0040-6090(02)00010-X

Xu, X., Di, Y., & Doi, M. (2016). Variational method for liquids moving on a substrate. *Physics of Fluids*, *28*(8), 087101. https://doi.org/10.1063/1.4959227

Yan, H., Shiga, H., Ito, E., Nakagaki, T., Takagi, S., Ueda, T., & Tsujii, K. (2006). Super water-repellent surfaces with fractal structures and their potential application to biological studies. *Colloids and Surfaces A: Physicochemical and Engineering Aspects*, *284–285*(1), 490–494. https://doi.org/10.1016/j.colsurfa.2005.10.083

Yang, X. G., Zhang, F. Y., Lubawy, A. L., & Wang, C. Y. (2004). Visualization of liquid water transport in a PEFC. *Electrochemical and Solid State Letters*, *7*(11), 408–411. https://doi.org/10.1149/1.1803051

Yeong, W., Ling, L., Wah, T., Neild, A., & Zheng, Q. (2011). Journal of Colloid and Interface Science Sliding variability of droplets on a hydrophobic incline due to surface entrained air bubbles. *Journal of Colloid And Interface Science*, *354*(2), 832–842. https://doi.org/10.1016/j.jcis.2010.11.027

Yong, K. W., Ganesan, P. B., Kazi, S. N., Ramesh, S., Badruddin, I. A., & Mubarak, N. M. (2018). Sliding behavior of droplet on a hydrophobic surface with hydrophilic cavities : A simulation study. *Physics of Fluids*, *30*(12), 122006.

https://doi.org/10.1063/1.5063857
Yoshida, N., Abe, Y., Shigeta, H., Nakajima, A., & Ohsaki, H. (2006). Sliding behavior of water droplets on flat polymer surface. *J. Am. Chem. Soc.*, *128*(13), 743–747. https://doi.org/10.1021/ja050617m
Yoshimitsu, Z., Nakajima, A., & Watanabe, T. (2002). Effects of surface structure on the hydrophobicity and sliding behavior of water droplets. *Langmuir*, *18*(15), 5818–5822. https://doi.org/10.1021/la020088p
You, L., & Liu, H. (2002). A two-phase flow and transport model for the cathode of PEM fuel cells. *International Journal of Heat and Mass Transfer*, *45*(11), 2277–2287. https://doi.org/10.1016/S0017-9310(01)00322-2
Yu, J., Froning, D., Reimer, U., & Lehnert, W. (2018). Apparent contact angles of liquid water droplet breaking through a gas diffusion layer of polymer electrolyte membrane fuel cell. *International Journal of Hydrogen Energy*, *43*(12), 6318–6330. https://doi.org/10.1016/j.ijhydene.2018.01.168
Yuan, P. (2005). *Thermal lattice Boltzmann two-phase flow model for fluid dynamics*. *Diss. University of Pittsburgh*. University of Pittsburgh. Retrieved from http://d-scholarship.pitt.edu/9825
Yue, P. T., Zhou, C. F., Feng, J. J., Ollivier G., C. F., & Hu, H. H. (2006). Phase-field simulations of interfacial dynamics in viscoelastic fluids using finite elements with adaptive meshing. *Journal of Computational Physics*, *219*(1), 47–67. https://doi.org/10.1016/j.jcp.2006.03.016
Zeng, W., Li, S., & Fu, H. (2018). Modeling of the pressure fluctuations induced by the process of droplet formation in a T-junction microdroplet generator. *Sensors and Actuators A: Physical*, *272*(4), 11–17. https://doi.org/10.1016/j.sna.2018.01.013
Zhang, D., Papadikis, K., & Gu, S. (2014). Three-dimensional multi-relaxation time lattice-Boltzmann model for the drop impact on a dry surface at large density ratio. *Int. J. Multiph. Flow.*, *64*(7), 11–18. https://doi.org/10.1016/j.ijmultiphaseflow.2014.04.005
Zhang, L. Z., & Yuan, W. Z. (2018). A lattice Boltzmann simulation of coalescence-induced droplet jumping on superhydrophobic surfaces with randomly distributed structures. *Applied Surface Science*, *436*(10), 172–182. https://doi.org/10.1016/j.apsusc.2017.11.200
Zhang, Q., He, M., Chen, J., Wang, J., Song, Y., & Jiang, L. (2013). Anti-icing surfaces based on enhanced self-propelled jumping of condensed water microdroplets. *Chemical Communications*, *49*(40), 4516. https://doi.org/10.1039/c3cc40592c
Zhong, Y., Joardar, A., Gu, Z. P., Park, Y. G., & Jacobi, A. M. (2005). Dynamic dip testing as a method to assess the condensate drainage behavior from the air-side surface of compact heat exchangers. *Experimental Thermal and Fluid Science*, *29*(9), 957–970. https://doi.org/10.1016/j.expthermflusci.2005.01.006
Zhu, X., Liao, Q., Sui, P. C., & Djilali, N. (2010). Numerical investigation of water droplet dynamics in a low-temperature fuel cell microchannel: Effect of channel geometry. *Journal of Power Sources*, *195*(3), 801–812. https://doi.org/10.1016/j.jpowsour.2009.08.021
Zhu, X., Sui, P. C., & Djilali, N. (2008). Three-dimensional numerical simulations of water droplet dynamics in a PEMFC gas channel. *Journal of Power Sources*, *181*(1), 101–115. https://doi.org/10.1016/j.jpowsour.2008.03.005
Zhu, X. T., Zhang, Z. Z., Xu, X. h., Men, X. h., Yang, J., Zhou, X. y., & Xue, Q. J. (2012). Facile fabrication of a superamphiphobic surface on the copper substrate. *Journal of Colloid and Interface Science*, *367*(1), 443–449. https://doi.org/10.1016/j.jcis.2011.10.008

List of Publications

1st Journal : Physics of Fluids
Volume : 30
Year : 2018
Page : 122006
Authors : K.W. Yong, P.B. Ganesan, M.S.N. Kazi, S. Ramesh, I.A. Badruddin, N.M. Mubarak.
Title : Sliding behaviour of droplet on a hydrophobic surface with hydrophilic cavities : A simulation study
doi : 10.1063/1.5063857

2nd Journal : Journal of Electrochemical Science and Technology
Volume : 10 (4)
Year : December 2019
Authors : K.W. Yong, P.B. Ganesan, M.S.N. Kazi, S. Ramesh, S.C. Sandaran
Title : Computational Modeling of Droplet Dynamics Behaviour in Polymer Electrolyte Membrane Fuel Cells: A Review
doi : 10.33961/jecst.2019.00262.

3rd Journal : International Journal of Refrigeration
Authors : K.W. Yong, P.B. Ganesan, E. Hamidi, S.N. Kazi, S. Ramesh
Title : The Effects of Structural Homogeneity, Hydrophobicity and Drainage Velocity on the Water Retention Behaviour in Different Porous Structures: A Computational Study
Manuscript : JIJR-D-20-00421(under review on 28th June 2020)